NON-RIGID IMAGE REGISTRATION FOR DEEP BRAIN STIMULATION SURGERY

A Dissertation
Presented to
The Academic Faculty

By

Muhammad Faisal Khan

In Partial Fulfillment
of the Requirements for the Degree
Doctor of Philosophy
in
Electrical and Computer Engineering

School of Electrical and Computer Engineering
Georgia Institute of Technology
December 2008

NON-RIGID IMAGE REGISTRATION FOR DEEP BRAIN STIMULATION SURGERY

Approved by:

Dr. Oskar Škrinjar, Advisor
Department of Biomedical Engineering
Georgia Institute of Technology

Dr. Patricio Vela
School of ECE
Georgia Institute of Technology

Dr. Allen Tannenbaum
School of ECE
Georgia Institute of Technology

Dr. John Oshinski
Department of Biomedical Engineering
Georgia Institute of Technology

Dr. Anthony Yezzi
School of ECE
Georgia Institute of Technology

Date Approved: October 28th, 2008

To my parents,

***Muhammad Ahmad Khan and Safia Ahmad**,*

for their love, support and prayers, which enabled me to achieve this goal in life.

ACKNOWLEDGMENTS

First and foremost, i would like to thank my advisor Dr. Oskar Škrinjar for his genuine support and guidance. Dr. Skrinjar has been a continual source of ideas and has been instrumental in explaining the basic concepts of research. He has been very patient with my progress and answered all my questions in detail. He always encouraged me and has carefully went through my publication drafts and presentations. I would also like to thank Dr. Allen Tannenbaum, Dr. Tony Yezzi, Dr. Patricio Vela and Dr. John Oshinski for their support as committee members.

I would like to thank my parents for their unconditional love and support for me. They always believed in me and patiently waited for my return to Pakistan after completing my PhD. Whatever good i have done till now is just because of my parents prayers. I would also thank my brother and sisters for their faith and confidence in me. They always trusted me and supported me in my decisions.

I would like to thank my wife, Saman Faisal, without whose encouragement, i would not have been able to achieve this. Her continual love and inspiration has always given me the strength to go through the hard times. She has been particularly patient during the never ending PhD research and has tolerated the workload, assignments, deadlines, exams and an empty bank account with a smile on her face. I would also like to thank my daughter Eeman Faisal who is six years old and has seen me going to school as far as she remembers. She does not understand much about PhD but she tells me that it is good for me to go to school as she does. She always asks me the grade i go to for which i have no answer. She has been my source of mental relaxation during stressful hours as playing five minutes with her takes all the research stress off me.

Last but not least, I would like to humbly thank my God "Allah" for giving me the courage and strength to complete my PhD. Almighty Allah has blessed me with so many things that i can not count and thank them.

TABLE OF CONTENTS

LIST OF TABLES

LIST OF FIGURES

SUMMARY

Movement disorders, which include Parkinson's disease (PD), dystonia, essential tremor (ET) and Huntingtons disease, are neurological conditions caused by a dysfunction in the basal ganglia. To date, the exact cause of movement disorders is not known and there are no cures for them, only means to reduce symptoms. Possible treatment options are drug-based (e.g. dopamine replacement), stereotactic neurosurgery, and physical therapy. Deep brain stimulation (DBS) surgery, a type of the microelectrode-guided surgery, is an effective treatment for the movement disorders patients that can no longer be treated by medications. The success of the DBS surgery is critically dependent upon the implantation accuracy of the DBS electrode array into the selected target (e.g. ventral intermediate nucleus (Vim), subthalamic nucleus (STN) or globus pallidus internus (GPi)). These target locations are usually not visible in the commonly used imaging modalities like magnetic resonance imaging (MRI) or computed tomography (CT). The goal of my PhD research is to develop the new methods for rigid and non-rigid image registration of 3D MRI scans of the movement disorders patients that underwent DBS surgery. These new rigid and non-rigid image registration methods help study and analyze the brain shift during the DBS surgery using the pre-operative (pre-op) and the post-operative (post-op) 3D MR images. The 3D registration methods are also used to develop an algorithm for atlas-based segmentation of the deep brain structures in the pre-op image for the DBS surgery planning and navigation.

The first contribution of my work is that we developed a diploë based rigid registration method for the intra-operative brain shift analysis during the DBS surgery. Rigid registration of serial MRI head scans is used in a number of clinical and research applications. The commonly employed approach for this task is intensity based registration of the whole scans. However, intensity, geometric and topological differences between the two scans can decrease the accuracy of the rigid registration. These differences can be caused by a multitude of factors including deformation of soft tissues inside and outside the skull, lesion development, changes in intracranial pressure, hematoma, pneumocephalus, swelling, and surgical interventions. To avoid the influence of image differences on the rigid registration,

we propose to register the two scans using the diploë. We use this diploë based rigid registration to register the pre-op and the post-op MR images of DBS subjects to study the intra-operative brain deformation or brain shift. The proposed methods for the brain shift analysis ensure rigid registration of the pre-op and the post-op image based on diploë only, which can be treated as a rigid structure as opposed to brain tissues.

We developed an interactive tool for the segmentation of diploë in the 3D MR images. Diploë is a soft and spongy tissue between the hard inner and outer skull plates. The rigid registration based on diploë gives reliable results as opposed to the whole head that has deformed brain tissue. This diploë based rigid registration is used to register the pre-op and the post-op images. The pre-op and the post-op images are than registered non-rigidly to recover the brain shift during the DBS surgery. The results show that the brain shift during the DBS surgery is comparable to the size of the DBS targets and should not be neglected. This brain shift may further lengthen and complicate the DBS surgery contrary to the common belief that brain shift during the DBS surgery is not considerable.

The second contribution of my PhD work is the development of an integrated electrophysiological and anatomical atlas for the DBS surgery. Most of the DBS targets are not clearly visible in the common imaging modalities like MRI and CT due to their small size (approximately 4-12 mm in diameter) and lack of tissue type variation from the surrounding structures. To help infer their location, indirect targeting approaches like atlas based segmentation are used. Atlas based techniques either segment the DBS target structure by registering a subject image with an already segmented atlas image or identify a target location in the subject image by registering it with an electrophysiological atlas. We present an integrated MRI atlas that has eleven deep brain structures manually segmented in it by an expert, and electrophysiological data of four implant locations (left STN, right STN, left GPi and right GPi) using MR images of twenty patients that underwent DBS surgery. This atlas MR image is than non-rigidly registered with the pre-operative subject MR image that gives its initial DBS target location (centroids of STN and GPi clusters) along with the segmented deep brain structures, which are used for guidance during the microelectrode mapping of the stereotactic procedure. The atlas based segmentation approach predicts the target automatically on the pre-op scan as opposed to the manual selection currently used.

A 3D anatomical MRI atlas was prepared that had eleven deep brain structures manually segmented in it by an expert. The quality of the atlas image allowed for the segmentation of the deep brain structures, which is not possible from the clinical MR head scans. We also developed a non-rigid registration method that registers this atlas with the subject images. The final non-rigid registration between the atlas and the subject image is used to transform the segmentation map of the atlas to the subject image. These segmented structures are used as either targets or for guidance in the DBS surgery. We also integrated the electrophysiological data on to the anatomical 3D MRI atlas. The data was obtained using the patients that had already undergone DBS surgeries. This electrophysiological data helps predict the initial location of the target, where the deep brain stimulator is to be placed. This automatic selection of the target is robust and closer to the actual target as opposed to the manually selected targets.

CHAPTER 1
INTRODUCTION

1.1 DBS Surgery for Movement Disorders

The DBS surgery is an effective treatment for the movement disorders patients whose disabling symptoms can no longer be treated by medication only [1, 2, 3, 4, 5]. About 300,000 people in the North America suffer from dystonia, about a million from Parkinson's disease (PD), and 1.5 million from essential tremor (ET) [6, 7]. PD strikes one in every hundred people over age sixty and affects men more often than women [8]. Movement disorders can be broadly divided into two categories: those exhibiting slow movement, or a lack of movement called "hypokinetic" (like PD); and those with excessive movement called "hyperkinetic" (such as ET). DBS surgery is a stereotactic procedure that uses a permanently implanted electrode lead to deliver continuous high-frequency electrical stimulation to the target areas in the midbrain like Vim, GPi, or STN [9, 10]. The exact mechanism of action is not yet known, but it is believed that high frequency stimulation in these areas inhibits neuronal activity, helping to rebalance control messages throughout the movement control centers in the brain. The electrode is connected subcutaneously to a pacemaker-like device implanted below the collarbone.

The DBS surgery uses intraoperative feedback through microelectrode recording (MER) to iteratively approach the target. Even if there is a large error in the initial estimate of the target location, after a number of microelectrode tracks the target location can be determined with an acceptable accuracy. Nevertheless, the more tracks are done, the longer and riskier the surgery becomes. Planning of stereotactic trajectories is done on the pre-op scan (MRI and/or CT) using one or more techniques including indirect targeting and direct visualization [11]. Discrepancies between the initial selected target and the final DBS lead location are due to the application accuracy of the stereotactic procedure which is degraded by several factors including imaging distortion and registration error [12, 13] and mechanical inaccuracy of the stereotactic frame [14].

The success of the DBS surgery is mainly dependent upon the implantation accuracy of the deep brain stimulator [15]. The small size, surrounding neuronal structures, and fibre

tracts make Vim, STN and GPi a difficult stereotactic target [16, 17]. Since Vim, STN and GPi are not clearly visible in common imaging modalities, atlas-based techniques are used to help infer the target location.

1.2 Brain Shift in DBS Surgery

The DBS surgery planing is done using the pre-op MRI scan, and it is usually assumed that anatomical structures do not move between the time of the preop image acquisition and the time of the surgery. Recent studies suggest that brain tissues shift during DBS surgery [18, 19, 20]. This intraoperative brain deformation, also known as "brain shift", may be due to the loss of cerebro spinal fluid (CSF), gravitational force, change in the intracranial pressure, forces due to insertion of DBS lead, pneumocephalus, transventricular penetration, or their combination. The brain shift during the DBS surgery is a potential contributor to the inaccuracy of the microelectrode guided procedure. Although intraoperative neurophysiological techniques such as microelectrode mapping (MEM) and macroelectrode stimulation can compensate for brain shift [21], its occurrence can lengthen the procedure and cause complications and - in some instances - may lead to inaccurate placement of the DBS lead.

Brain shift has been recognized as a possible source of inaccuracy in DBS surgery and initial efforts to quantify this phenomenon have been reported. Winkler et al. [18] studied a single PD patient that underwent DBS surgery and measured a brain shift of 2 mm in the midbrain region. Khan et al. [19] analyzed the brain shift of 25 patients at and around the implantation site. Mean brain shift of 5 mm and 3.5 mm in cortical surface and thalamus respectively was observed by Wester et al. [22] for 12 stereotactic thalamotomies. Halpern et al. [20] analyzed the shortening of the length from the anterior commissure to the posterior commissure during DBS surgery and its correlation to the shift at the cortical surface in 50 patients. We also note the relevant work on brain shift analysis for procedures other than DBS surgeries. Hill et al. [23] estimated the median brain surface shift after the dura had been opened to range from 0.3 mm to 7.4 mm. Bucholz et al. [24] reported the average surface brain shift for cases in which hematoma or tumors were removed to be 9.5 mm and 7.9 mm, respectively. Similar values for the surface brain shift were reported by others [25, 26, 27, 28]. Another group of efforts is focused on compensation of the intraoperative

brain deformation by updating the images displayed to the surgeon based on a deformable brain model [29, 30, 21]. Furthermore, a few groups used intraoperative scanners to image the brain during the surgery, analyzed the brain deformation patterns, and estimated the brain shift magnitude [25, 26, 31, 32]. While most of the work on the brain deformation analysis has been done using MR images, some researchers used intraoperative ultrasound images for this purpose [24, 32].

We performed a comprehensive analysis of brain shift in DBS surgery over 25 subjects that underwent DBS surgery [19]. Brain shift of up to 4 mm was observed in deep brain structures. On average, the recorded shift was in the direction of gravity, with deeper structures experiencing smaller shift than more superficial structures. The main conclusion of the study is that the brain shift is comparable to the size of the targets in the DBS surgery and should not be ignored. Techniques that minimize the amount of brain shift may therefore lead to increased accuracy of DBS lead implantation. We also analyzed the brain shift during the DBS surgery over the entire brain for eight patients [33].

1.3 Atlas based segmentation of deep brain structures

Deep brain structures are the anatomical structures in and around midbrain and ventricular regions [34]. These structures are used as targets or for guidance in neurosurgical procedures, including DBS surgery [10, 16]. Most of the deep brain structures are not visible in the common imaging modalities like MRI or CT. This is because of their small size (e.g. STN is approximately 4x6 mm in the axial plane and the radius of GPi is approximately 4 mm, both of which are used as targets in DBS surgery) and lack of tissue type variation from the surrounding structures that can be captured by CT or MRI. Due to lack of their visibility in MRI or CT, atlas based approaches with indirect intraoperative mapping are usually used to infer their locations. These methods can have up to several millimeters of error, which can increase the duration of the surgery and affect the surgical outcome. The atlas-based techniques localize the target in the subject image without segmentation of the deep brain structures [35, 36].

Pre-op patient MRI head scans are used for the planning and navigation of the surgery.

The DBS surgery procedure may be summarized in the following steps: 1) Target identification and localization on the patient pre-op MRI scan; 2) Mapping of the initial target location on to the physical location in the patient's head; 3) Intraoperative refinement of the target location using microelectrode mapping; 4) Placing of the final DBS electrodes in the deep brain target structure. The atlas based localization approaches use different anatomical atlases [37, 38] to estimate the initial location of the target structure (step 1) and than improve them in step 3. But these methods can have up to several millimeters of error in step 1, which may prolong step 3 thus increasing the duration of the surgery and affecting the surgical outcome. The increase in the surgery duration also increases the chances of brain shift [19, 18] which further complicates the microelectrode mapping of step 3.

In order to automate the DBS surgery planning and navigation, we developed an integrated MR atlas [39], which has eleven deep brain structures segmented in it along with electrophysiological data in the shape of four clusters (left STN, right STN, left GPi and right GPi). The quality of the atlas image allowed for the manual segmentation of the deep brain structures by an expert, which is not possible from the clinical MR head scans. This integrated MR atlas image is non-rigidly registered to the pre-op subject MR image. The final non-rigid registration between the atlas and the subject image is used to transform the segmentation maps and the cluster centroids of the atlas to the subject image. This approach automatically provides the segmentation of eleven deep brain structures (named in section 4.1.3) and the initial estimate of the DBS target location (left STN, right STN, left GPi and right GPi) in the pre-op patient images, which automates step 1 as described above and helps in target correction through microelectrode mapping of step 3.

Computer aided placement of deep brain stimulator for DBS surgery has been studied previously. Atlas based segmentation of the DBS target location or the DBS target structure is the most commonly used approach for computer aided placement. The main idea is to use the atlas image or reference image that has either DBS targets or DBS structures identified in them. The next step is to non-rigidly register this atlas with the pre-op or intra-operative patient images to get the target point or segmentation of the target structure in the patient image. The use of non-rigid registration is required to capture the inter-image variations in

sizes and shapes of the anatomical structures.

There are four major approaches for the atlas based techniques for localization of the targets. The first approach uses anatomical atlases like Talairach-Tournoux atlas [37] and Schaltenbrand-Wahren atlas [38] and register them with the patient's pre-op MR image [40, 41]. The second approach uses manual segmentation of brain structures in a reference/atlas MR image by an expert and than non-rigidly register the atlas to the patient MR image to get the segmentation in the patient image [42, 43, 44, 45, 46]. The third approach uses a combination of the first two approaches. MRI atlas is prepared using anatomical atlases [35, 47]. The fourth approach prepares electrophysiological MR atlas using previously operated subjects. This atlas-based technique localizes the target in the subject image without segmentation of the deep brain structures [48, 36].

In addition to the above described atlas based approaches, direct targeting of the DBS target location has also been studied. Castro et. al. used this approach where both T1 and T2-weighted images were available [49]. T2 inversion recovery image showed clear boundaries of STN. Two best subjects were selected as atlas images, one for right STN and one for left STN. Intra-subject T1-T2 multimodal rigid registration was performed to bring STN target locations onto T1 images, which are than used as atlases. We also acknowledge the direct segmentation methods of the brain structures without using atlas-based approach [50, 51, 52, 53, 54, 55, 56, 57, 58].

CHAPTER 2

DIPLOË BASED RIGID REGISTRATION

Rigid registration of serial MRI head scans is used in a number of applications including image-guided therapy [59], surgical planning and navigation [60], intraoperative brain deformation analysis [61, 62, 63, 64, 19] and analysis of brain changes associated with tumor growth [65], multiple sclerosis [66], Alzheimer's disease [67] and schizophrenia [68]. A common denominator of these applications is that there are image differences in two or more MRI scans that need to be analyzed. In general, these image differences represent a combination of intensity, geometric and topological changes that can be caused by a multitude of factors including deformation of soft tissues inside and outside the skull, lesion development, changes in intracranial pressure, hematoma, pneumocephalus, swelling, and surgical interventions. Rigid registration is used as a step in the analysis of these differences. For an accurate analysis of image differences it is critical that the rigid registration is accurate. However, the image differences may affect the rigid registration and decrease its accuracy, which in turn decreases the accuracy with which they can be analyzed. An example of geometric image differences is shown in Fig. 1. To analyze the brain deformation one first needs to rigidly register the pre-operative (Fig. 1a) and post-operative (Fig. 1b) image. The substantial brain deformation due to the bilateral pneumocephalus visible in Fig. 1b can significantly lower the accuracy of the rigid registration if it is based on the whole scans. If the rigid registration is off for a couple of millimeters, so will be the brain shift vectors that are computed from the rigidly registered pre- and post-operative images. Such an error may not be negligible and in some instances can lead to incorrect conclusions.

The rigid image registration methods suggested in the literature can be categorized as non-image-based and imaged-based. The non-image-based methods use external adhesive fiducial markers [69], implantable fiducial markers [70], and frames [71]. The use of implantable markers results in a very accurate rigid registration since the markers are screwed into the skull, i.e. they are not affected by the image differences. However, the procedure is prohibitively invasive for regular clinical use. The non-image-based methods require a more complex acquisition than the image-based methods and they cannot be used to register

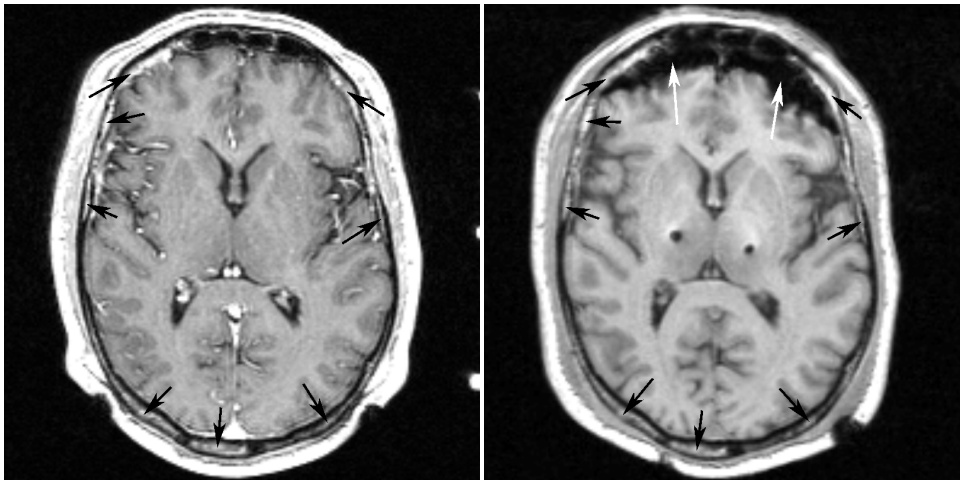

(a) (b)

Figure 1. Pre-operative (a) and post-operative (b) corresponding axial MR slices of a patient that underwent deep brain stimulation surgery are shown with the diploë marked with black arrows. As a result of the surgery, the brain experienced substantial deformation due to the development of a bilateral pneumocephalus (marked with white arrows) while the diploë remained unchanged.

scans taken over extended periods of time, e.g. to monitor the progress of a diseases. The image-based methods include feature-based [72, 73, 74, 75] and intensity-based [76] methods, which is the most common approach for the rigid registration of MRI scans. However, the suggested image-based methods use the image information from the whole scans and consequently the accuracy of rigid registration depends on the amount of image differences. The main drawback of the approaches suggested in the literature is that the rigid registration and the analysis of image differences are not decoupled, i.e. the presence of image differences introduces an error in rigid registration, which is then translated into an error of similar magnitude in the analysis of image differences.

To avoid the influence of image differences on the rigid registration, we propose to register the two scans using the diploë (Fig. 1) [77]. The diploë is a soft, spongy and porous tissue contained inbetween the hard outer and inner bone plates of the skull and for this reason it can be considered rigid for the registration purposes. The T1-weighted MR intensity of the bone plates, cerebro-spinal fluid and air is weak while it is strong for the diploë. This makes the boundaries of the diploë well defined as opposed to the poorly defined boundaries of the skull. Since the diploë does not change its shape and the rigid

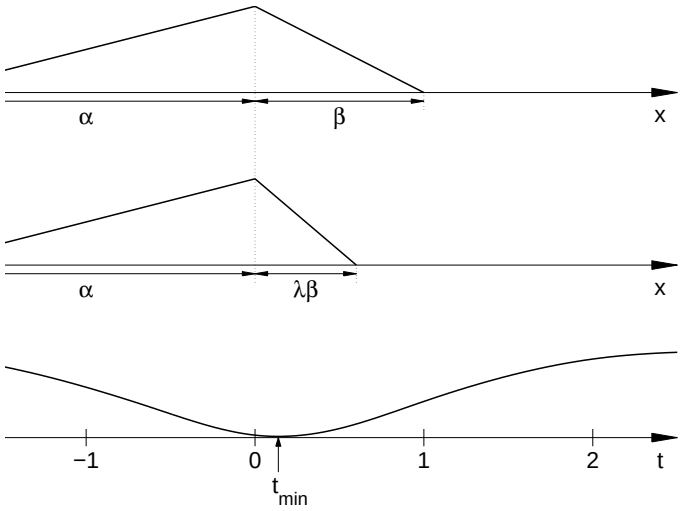

Figure 2. $I(x)$ **is image of a 1-D object composed of a rigid (left region with size** α**) and a deformable part (right region with size** β**).** $J(x)$ **is the image of the 1-D object after the deformation: the rigid part remained the same, while the deformable part was scaled by a factor** λ**.** $SSD(t)$ **is the sum of squared differences between** $J(x-t)$ **and** $I(x)$ **as a function of translation** t**. The graph is drawn for** $\alpha = 2$**,** $\beta = 1$ **and** $\lambda = .6$**, in which case the minimum is achieved at** $t_{min} = 0.138$**.**

registration based on the diploë does not depend on the image differences inside and outside the diploë, this approach can produce accurate rigid registration and it is decoupled from the analysis of image differences.

2.1 Rationale

To justify the proposed approach, we first mathematically show that the underlying deformation difference between two images can affect their rigid registration. The results are proven using the sum of squared differences as the similarity measure for the registration, but equivalent results can be obtained for other popular image similarity measures including information theoretic ones.

2.1.1 A One-Dimensional Deformable Object

To illustrate the problem, we define a 1-D object composed of a rigid part and a deformable part. The image of the object before and after deformation is given in Fig. 2. To rigidly register the pre- and post-deformation images[1], we seek the translation that minimizes the

[1]Rigid transformation in the 1-D case is just a translation.

sum of squared differences between $I(x)$ and translated $J(x)$,

$$SSD(t) = \int [J(x-t) - I(x)]^2 \, dx. \tag{2.1}$$

The translation that minimizes (2.1) is (see Appendix A)

$$t_{min} = \begin{cases} \frac{\alpha^2+\alpha\beta-\alpha\sqrt{(\alpha+\beta)(\alpha+\lambda\beta)}}{\alpha+\beta} & \lambda \leq 1, \\ \frac{-\alpha^2-\lambda\alpha\beta+\alpha\sqrt{(\alpha+\beta)(\alpha+\lambda\beta)}}{\alpha+\lambda\beta} & \lambda > 1. \end{cases} \tag{2.2}$$

It follows that the whole-scan rigid registration (i.e. the minimization of (2.1)) does not align the rigid structures of the 1-D object (which would be the case for $t_{min} = 0$) as long as there is some deformation present, i.e. as long as $\lambda \neq 1$ (note that $t_{min} = 0$ if and only if $\lambda = 1$). This conclusion holds regardless of the relative size of the rigid (α) and nonrigid (β) parts.

2.1.2 General Case

Now we show that the conclusion obtained in the previous section holds in the general case. Let an N-dimensional object be composed of rigid and deformable parts. Let $I(\mathbf{r})$ be the image of the object before deformation and let $J(\mathbf{r})$ be the image of the object after the deformable part underwent a non-rigid deformation. An affine transformation can be written as

$$\mathbf{L}(\mathbf{r}) = \mathbf{A}\mathbf{r} + \mathbf{b}, \tag{2.3}$$

where $\mathbf{A}$ is the transformation matrix and $\mathbf{b}$ the translation vector. If $\mathbf{A}$ is a rotation matrix then (2.3) represents a rigid body transformation. If $\mathbf{A}$ is an identity matrix and $\mathbf{b}$ a zero vector then (2.3) represents an identity transformation. The sum of squared differences between I and affinely transformed J is

$$SSD(\mathbf{A}, \mathbf{b}) = \int [J(\mathbf{A}\mathbf{r} + \mathbf{b}) - I(\mathbf{r})]^2 \, . \tag{2.4}$$

Theorem. The identity transformation is not a minimizer of (2.4).

A proof of the theorem is given in Appendix B. The meaning of the theorem is, contrary to the widely accepted belief, that the whole-scan rigid registration of two scans that differ by a deformed region does not "latch to rigid structures if the deformed region is not

substantial". In fact, no matter how big or small the rigid region is, as long as there is a deformed part, the whole-scan rigid registration will not align the rigid structures. Thus, in order for the rigid registration to align the rigid structures of two scans that have nonrigid differences, one first needs to identify the rigid structures and then base the registration on them.

2.2 Methods

The proposed approach is simple: segment the diploë and then rigidly register the two scans using only the diploë region. More precisely, we segment the diploë only in one scan and then rigidly move the other scan until the image similarity over the segmented diploë is maximized. To segment the diploë we use a semi-automated tool (Section 2.2.1) and for the registration we maximize the normalized mutual information [78] using a gradient descent method (Section 2.2.2).

2.2.1 Diploë Segmentation

We have developed a semi-automated tool for the diploë segmentation that reduces the segmentation time from several hours for manual segmentation to less than 30 minutes for T1 weighted MRI head scans of 200 slices with 256 x 256 pixels. The segmentation procedure consists of the following steps.

- STEP 1 (interactive): The user selects approximately uniformly spaced eight to ten seed points on the diploë in one sagittal (Fig. 3a, first row), one coronal (Fig. 3b, first row) and one axial slice (Fig. 3c, first row).

- STEP 2 (automated): The seed points are interpolated using the pseudo thin plate spline interpolation on the sphere [79] to form the mid-diploë surface. The sphere is uniformly sampled [80] and the samples are projected to the mid-diploë surface over the extent defined by the seed points (Fig. 3d, first row). The projected samples are referred to as the control points.

- STEP 3 (automated): For each control point, a search is performed along the normal of the mid-diploë surface for two intensity minima (corresponding to the skull bone

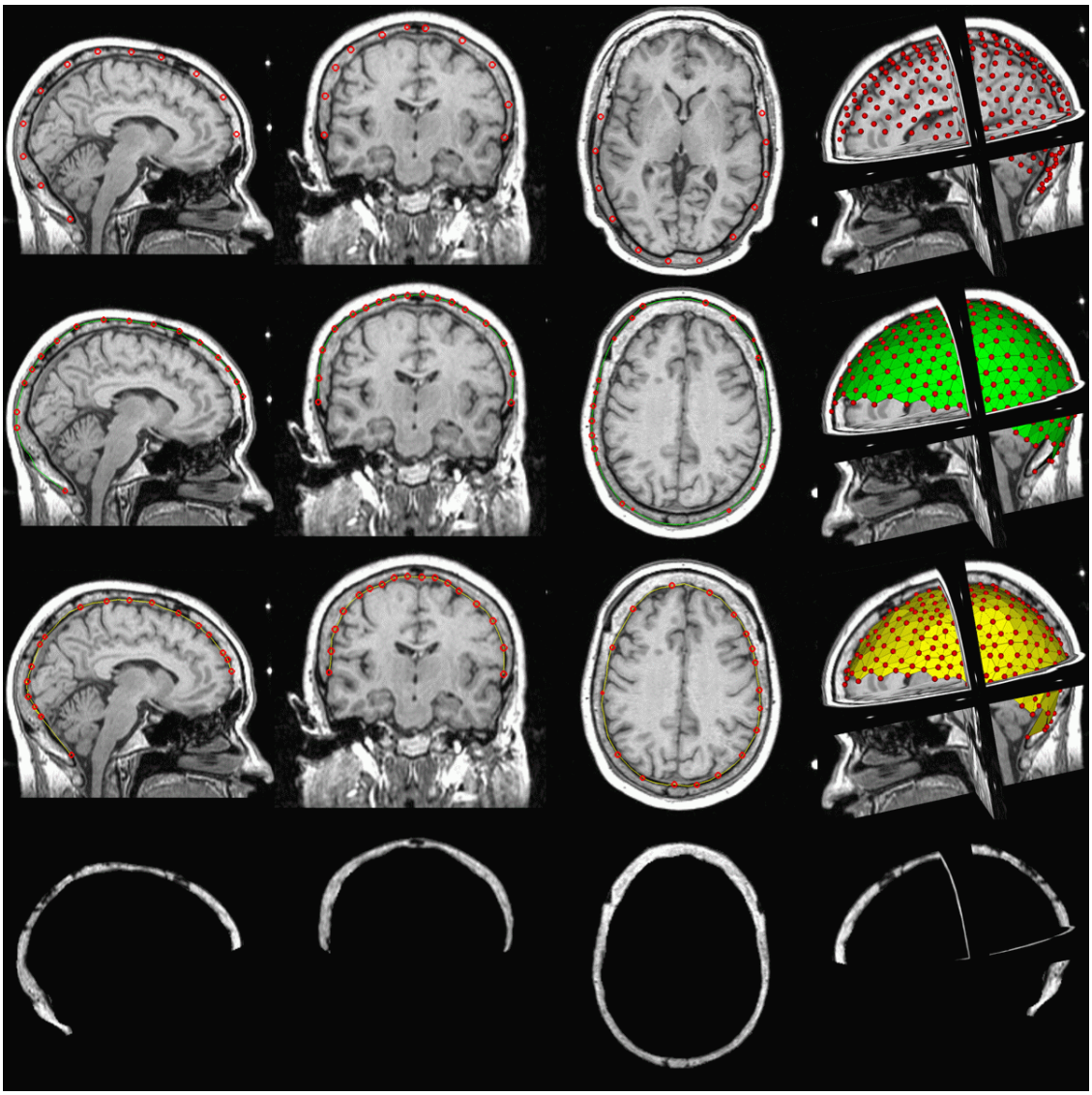

(a) (b) (c) (d)

Figure 3. The semi-automated diploë segmentation procedure involves selection of seed points (first row: a, b, c) and generation of mid-diploë surface control points (first row, d), outer diploë boundary (second row), inner diploë boundary (third row) and diploë region (fourth row). Each row contains a sagittal (a), coronal (b), axial (c) and three-dimensional (d) view.

plates) separated by an intensity maximum (corresponding to the diploë). The locations of the two intensity minima define the corresponding control points of the initial outer (Fig. 3, second row) and inner (Fig. 3, third row) diploë boundary.

- STEP 4 (interactive): The user corrects the position of any misplaced control point on the outer and inner diploë boundary.

- STEP 5 (automated): The segmentation map of the diploë is generated by including all the voxels inbetween the outer and inner diploë boundary (Fig. 3, fourth row).

2.2.2 Rigid Registration

Let I denote the image in which the diploë is segmented, X the segmented region and J the other image. During the registration I is held fixed and J is moving. Let $T_{\theta_x,\theta_y,\theta_z,t_x,t_y,t_z}$ represent a rigid body transformation composed of three rotations $(\theta_x, \theta_y, \theta_z)$ and three translations (t_x, t_y, t_z). To rigidly register I and J we search for the six transformation parameters that maximize the normalized mutual information (NMI) [78] between the two images over the diploë region,

$$T = \max_{\theta_x,\theta_y,\theta_z,t_x,t_y,t_z} NMI\left[I(X), J(T_{\theta_x,\theta_y,\theta_z,t_x,t_y,t_z}(X))\right]. \tag{2.5}$$

NMI in Eq. (2.5) is given by

$$NMI(I,J) = \frac{\sum\limits_{i_a \epsilon I(X)} P(i_a)\log(P(i_a)) + \sum\limits_{j_b \epsilon J(X)} P(j_b)\log(P(j_b))}{\sum\limits_{(i_a,j_b)\epsilon I(X)\times J(X)} P(i_a,j_b)\log(P(i_a,j_b))}, \tag{2.6}$$

where X is the region of overlap of the two images, $I(X)$ and $J(X)$ are the sets of intensities of images I and J respectively, $P(i_a)$ and $P(j_b)$ are the marginal probabilities and $P(i_a, j_b)$ is the joint probability. To determine the joint and marginal intensity distributions needed for the computation of NMI we use the binning approach with 25 bins for the diploë-based registration and 50 bins for the whole-scan registration. We use a multi-resolution optimization method similar to that described by [76] to determine the transformation parameters.

2.3 Protocols and Subjects

Three different types of surgery patients were used as subjects in our studies: DBS surgery, epilepsy surgery and tumor removal surgery.

Table 1. Relevant parameters of 25 DBS subjects. The "DBS lead" column lists the number of DBS leads present in the pre-op and the post-op image. The "side" column means the side of the patient head where stimulator was implanted (R=right, L=left). The midbrain structure in which the deep brain stimulator was implanted is listed under the "target" column. Duration is the total duration of the surgery in hours and delay is the time between the end of surgery and the post-op scan in hours.

Subject No.	DBS Lead		Side	Target	Duration [hr]	Delay [hr]
	preop	postop				
1	0	1	R	STN	3.4	3.05
2	0	1	L	STN	3.6	1.58
3	0	1	L	STN	3.73	5.57
4	0	1	R	STN	3.55	1.22
5	0	2	L/R	GPi/GPi	7	4.05
6	0	2	L/R	STN/STN	6.43	0.53
7	0	2	L/R	STN/STN	6.4	2.29
8	1	2	R	STN	4.47	2.38
9	0	1	R	GPi	4.4	3.12
10	0	1	L	GPi	3.73	1.28
11	0	2	L/R	STN/STN	5.2	4
12	0	2	L/R	GPi/GPi	6.45	0.63
13	0	1	R	GPi	3.63	1.43
14	0	1	L	GPi	4.85	2.68
15	0	1	R	GPi	4.3	4.78
16	0	2	L/R	Vim/Vim	4.6	1.45
17	0	1	L	Vim	4.05	3.4
18	0	2	L/R	Vim/Vim	5.38	2.08
19	1	2	L	STN	2.45	2.05
20	1	2	L	STN	5.25	1.5
21	1	2	L	STN	2.41	2.18
22	0	1	R	Vim	5.43	3.25
23	0	1	R	STN	3.45	4.28
24	0	1	L	STN	4.37	1.7
25	1	2	L	STN	4.1	5.08

2.3.1 DBS Subjects

Twenty-five patients underwent stereotactic implantation of unilateral (18 patients) or bilateral (7 patients) DBS leads into STN (14), GPi (7) or Vim (4). On the day of surgery, a stereotactic frame (CRWfn, Radionics, Burlington, MA) was fitted and volumetric T1

weighted MR images were obtained. The Fast Field Echo protocol with gradient echo (flip angle = 30, repetition time TR = 25 ms and echo time TE = 4.6 ms) was used to acquire both the pre-op and the post-op images. Pre-op MRI images had around 200 slices of 256 x 256 pixels with in-plane resolution of 1 mm and slice thickness of around 0.9 mm. Fifteen post-op MRI images had 120 slices of 256 x 256 pixels with in-plane resolution of 1 mm and slice thickness of 0.8 mm, while 10 post-op MRI images had 150-200 slices of 256 x 256 pixels with in-plane resolution of 1 mm and slice thickness of 0.8 mm. All images were acquired using a Philips Medical System Gyroscan 1.5T MRI scanner. Table 1 shows the relevant parameters of the 25 DBS subjects.

The subjects with the partial post-op scans (120 slices) are labeled as DBS_{p1} through DBS_{p15} and the subjects with the complete post-op scans (200 slices) are labeled as DBS_{c1} through DBS_{c10}. The pre-op scan of each patient is marked with a and the post-op scan with b (e.g. $DBS_{p7,b}$ denotes the post-op scan of patient DBS_{p7}).

2.3.2 Epilepsy Subject

The MRI scans of an epilepsy patient that underwent two subdural electrode implantation surgeries were also used. The patient had a pre-op and two post-op scans, which are labeled EPI_a, EPI_b, and EPI_c, respectively. All three scans had 200 slices of 256 x 256 pixels with the in-plane resolution of 1 mm and slice thickness of 0.9 mm.

2.3.3 Tumor Removal Subject

Intraoperative MRI scans of a patient that underwent a tumor removal surgery were used. The patient was scanned four times over the course of the surgery. The first scan was acquired just before the beginning of the surgery and the other three scans were acquired at different stages of the surgery. The scans had 60 slices of 256 x 256 pixels with the in-plane resolution of 0.9375 mm and slice thickness of 2.5 mm. The four scans are labeled as TR_a through TR_d, where a corresponds to the first and d to the last scan.

2.4 Results

2.4.1 A Simulated Brain Deformation Study

We performed a 2D simulation to analyze the effect of brain deformation on rigid registration in a controlled environment. The brain and the diploë were manually segmented in a 2D axial MRI slice (Fig. 4a). The segmented brain was deformed linearly (a specified displacement value, referred to as the deformation parameter, at the top and 0 mm at the bottom) from the top left side at an angle of 45° as shown by the white arrow in Fig. 4b. The only difference between images in Fig. 4a and Fig. 4b is that the brain is deformed, i.e. the rigid structures are perfectly aligned and the intensities are the same at the corresponding locations.

The original image (Fig. 4a) and the deformed image (Fig. 4b) were rigidly registered by testing all combinations of the angle of rotation (θ), translation in the x (t_x) and translation in the y (t_y) direction and selecting that combination of the transformation parameters that yielded the optimal value of the image similarity measure. While the exhaustive search approach is slow, it guarantees to find the global optimum. The search space was discretized with steps of 1° for θ and 1 mm for t_x and t_y and the minimal and maximal values in the search space were ±25° for θ and ±15 mm for t_x and t_y. We performed the registration with four image similarity measures: mean square difference (MSD), normalized cross correlation (NCC), mutual information (MI), and NMI [76].

We gradually increased the brain deformation (i.e. the deformation parameter) and compared the performance of the whole-scan and diploë-based approaches for the four image similarity measures. For the whole-scan approach we used both diploë and brain image information and for the diploë-based approach we used only the diploë image information. The diploë-based approach in all the cases resulted in the perfect alignment of the rigid structures, i.e. the global optimum was always for $\theta = 0°$, $t_x = 0$ mm, and $t_y = 0$ mm. However, the performance of the whole-scan approach depended on the amount of brain deformation. The graphs in Fig. 4c show the mean registration error distance over the diploë region for the whole-scan approach for the four image similarity measures. The mean registration error distance increased with the amount of brain deformation for all four image similarity measures. The brain deformation was increased with increments of

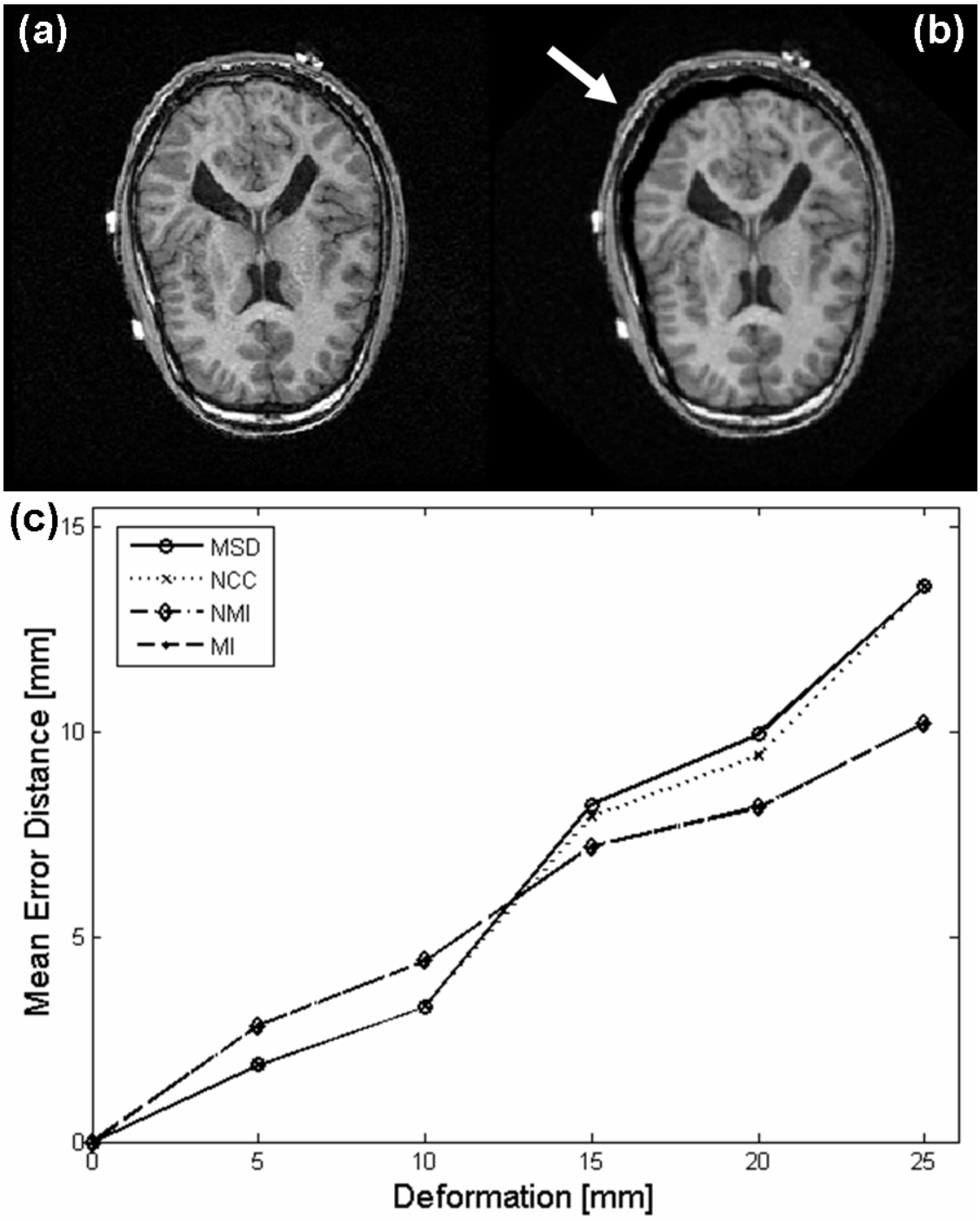

Figure 4. The original and the brain deformed image are shown in (a) and (b), respectively. The white arrow in (b) shows the direction of the simulated brain deformation, which was 10 mm in this image. The graphs in (c) show the mean error distance over the diploe region at different brain deformations for the whole-scan approach for the four image similarity measures.

Table 2. The whole-scan rigid registration errors at the global optimum (θ [deg], t_x [mm], t_y [mm]) of the four image similarity measures at different deformations [mm] for the simulated brain deformation study.

Deformation	MSD			NCC			NMI			MI		
	θ	t_x	t_y	θ	t_x	t_y	θ	t_x	t_y	θ	t_x	t_y
0	0	0	0	0	0	0	0	0	0	0	0	0
5	-1	1	-1	-1	1	-1	0	2	-2	0	2	-2
10	-2	2	-1	-2	2	-1	-1	3	-3	-1	3	-3
15	-2	5	-6	-1	5	-6	-1	5	-5	-1	5	-5
20	-3	6	-7	-3	5	-7	-2	6	-5	-2	6	-5
25	-1	9	-10	-1	9	-10	-2	7	-7	-2	7	-7

5 mm form 0 mm to 25 mm. The results for NMI and MI were exactly the same, while MSD and NCC had very similar performance. Overall, the four image similarity measures exhibited similar behavior. Table 2 shows the rigid registration parameters at the global optimum for the whole-scan approach for the four image similarity measures. The diploë-based approach always resulted in perfect alignment of the rigid structures ($\theta = 0°$, $t_x = 0$ mm, $t_y = 0$ mm) and therefore its results are not shown in Table 2.

2.4.2 Study I

The first study was composed of the pre-op and the post-op scans of 25 DBS surgery patients. Fig. 5 shows the result of the rigid registration of the pre-op and post-op scan for one DBS patient using the whole-scan and diploë-based approach. The registered images are shown using the checkerboard display, which is a visualization technique that shows alternate squares from the two images. There was no ground truth to compare the diploë-based and the whole-scan registration against and the only means to evaluate the quality of the registration was to inspect the registered images. Since brain and scalp tissues possibly deformed between the pre-op and post-op scan acquisitions, we evaluated the quality of the rigid registration by inspection of the alignment of the skull and diploë, which did not deform. One can see from Fig. 5 that the diploë-based registration resulted in a very good alignment of the skull and diploë, whereas the whole-scan registration had visible misalignment of the skull and diploë. We have inspected the registration results for all the 25 DBS subjects for all the slices and there was no measurable misalignment of the skull and diploë for the diploë-based registration.

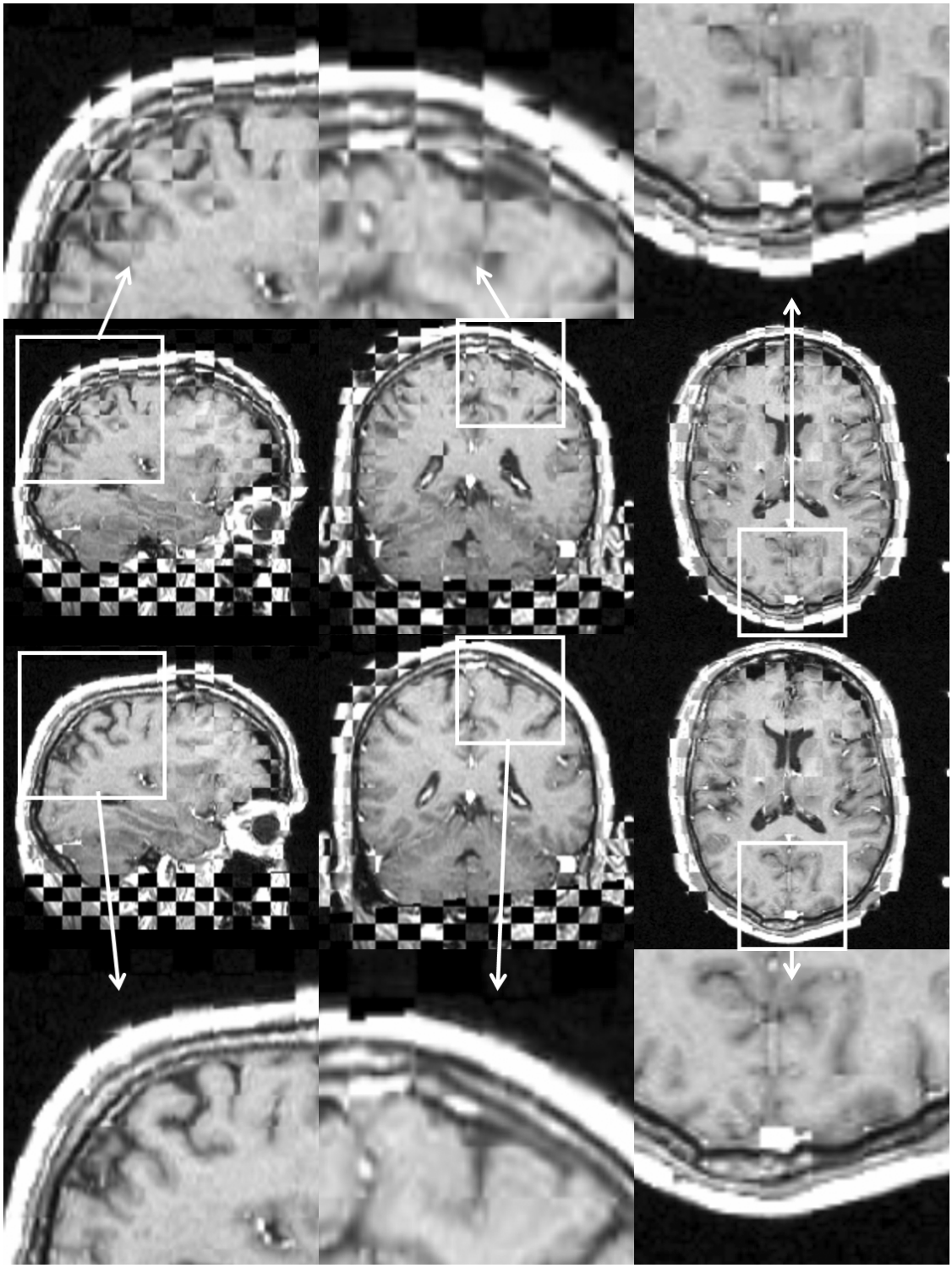

(a) (b) (c)

Figure 5. The checkerboard display of a sagittal (a), coronal (b) and axial (c) slice of the pre-op and the rigidly registered post-op scan of a DBS subject. The whole-scan registration is shown in the second row and the corresponding zoomed-in regions in the first row. The diploë-based registration is shown in the third row and the corresponding zoomed-in regions in the fourth row. Note the misaligned skull and diploë in the first row and the well aligned aligned skull and diploë in the fourth row.

To evaluate the registration error of the whole-scan registration, we compared it to the diploë-based registration, since it had no measurable registration error. Let T_{WS} and T_{DB} represent the rigid transformations obtained by the whole-scan and diploë-based approached, respectively. For each point r in the segmented diploë in the pre-op scan, we define the "whole-scan registration error distance" as

$$ED(r) = |T_{WS}(r) - T_{DB}(r)| . \tag{2.7}$$

Then we computed the mean, standard deviation and maximal error distance over the entire segmented diploë region. The distributions of the mean, standard deviation and maximal error distance for the 25 DBS subjects are shown in Fig. 6.

2.4.3 Study II

The second study was composed of MRI scans of an epilepsy patient that underwent two subdural electrode implantation surgeries. Fig. 7 shows the result of $EPI_a - EPI_b$ and $EPI_a - EPI_c$ rigid registration using the whole-scan and diploë-based approach. One can see from Fig. 7 that the diploë-based registration resulted in a very good alignment of the skull and diploë, whereas the whole-scan registration had visible misalignment of the skull and diploë. We have inspected the registration results for all the slices for $EPI_a - EPI_b$ and $EPI_a - EPI_c$ registration and there was no measurable misalignment of the skull and diploë for the diploë-based registration. The mean, standard deviation, and maximal error distance for the whole-scan registration of EPI_a and EPI_b were 1.2 mm, .5 mm and 2.3 mm, respectively, and of EPI_a and EPI_c were 1.5 mm, .3 mm and 2.2 mm, respectively.

2.4.4 Study III

The third study was composed of intraoperative MRI scans of a patient that underwent a tumor removal surgery. The patient was scanned four times over the course of the surgery. Fig. 8 shows the result of $TR_a - TR_d$ rigid registration using the whole-scan and diploë-based approach. One can see from Fig. 8 that both the whole-scan and diploë-based registration resulted in a good alignment of the skull and diploë. We have inspected the registration results for all the slices for $TR_a - TR_b$, $TR_a - TR_c$ and $TR_a - TR_d$ registration and the skull and diploë alignment for both the whole-scan and diploë-based approaches

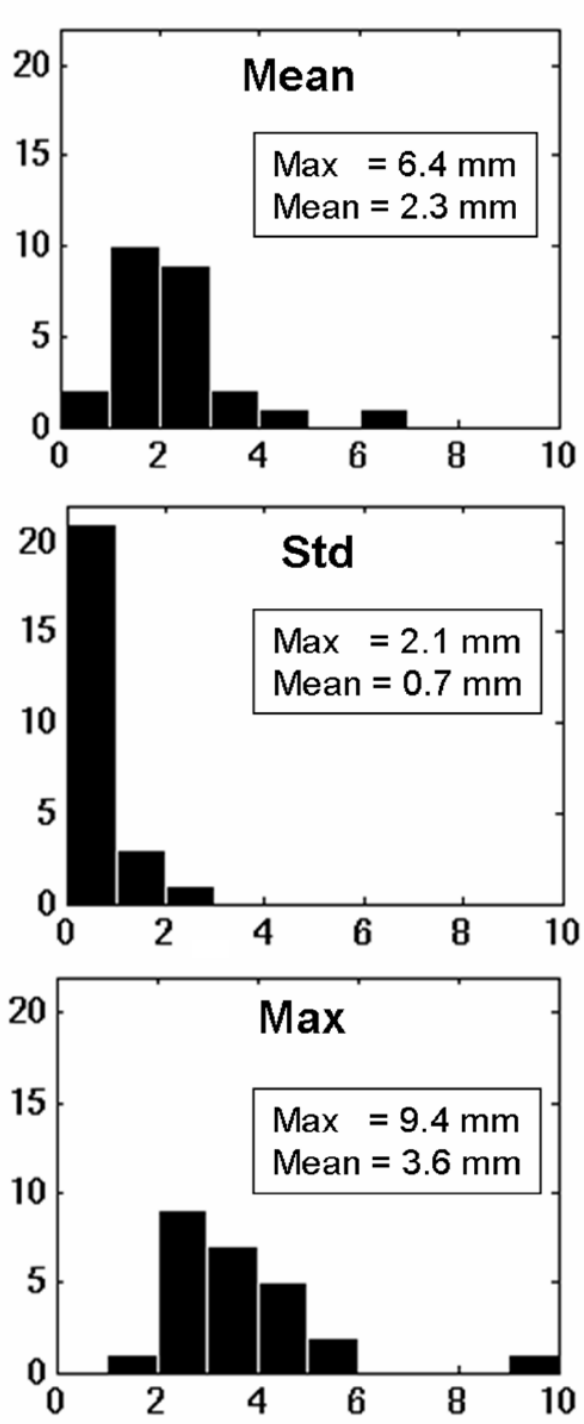

Figure 6. The distributions of the mean, standard deviation and maximal error distance for the 25 DBS subjects for the whole-scan registration.

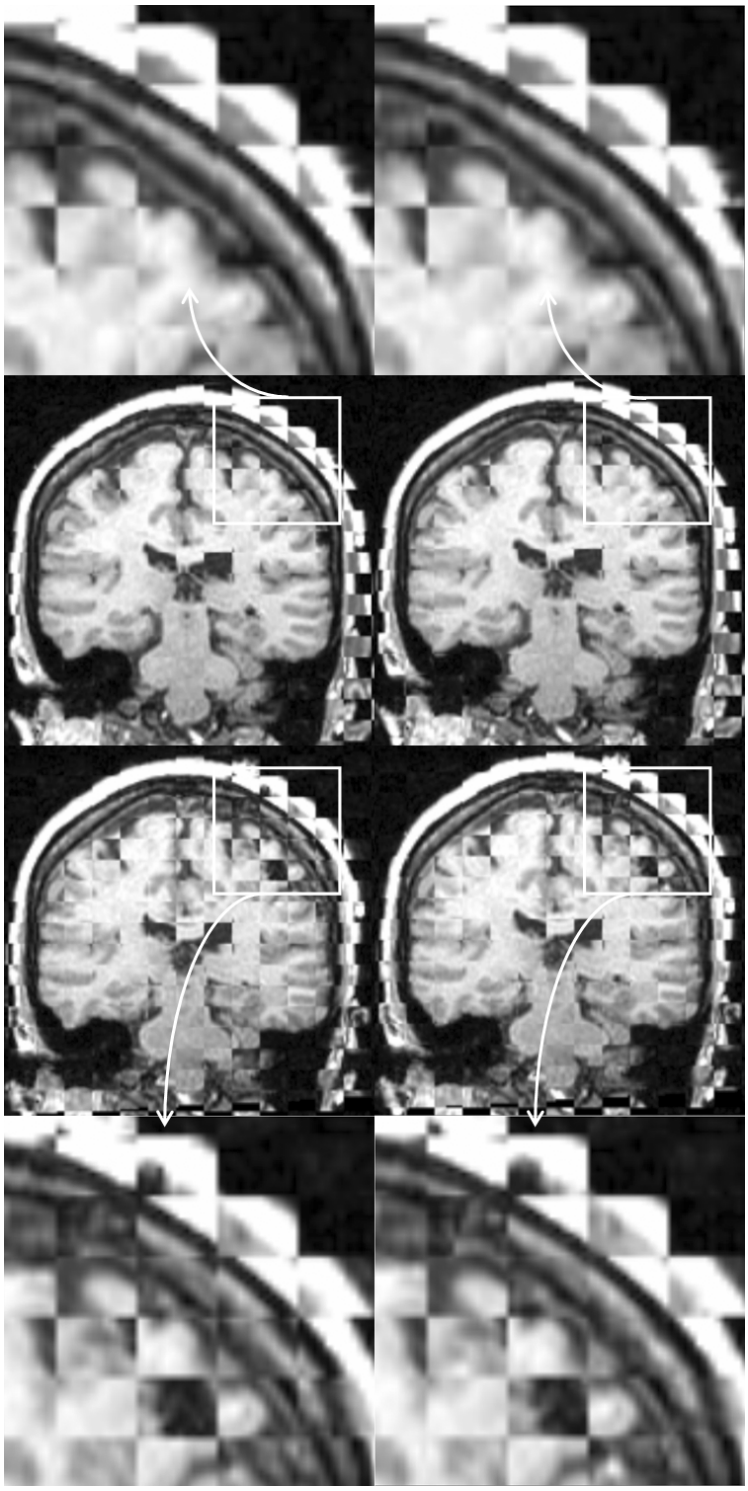

(a) (b)

Figure 7. The checkerboard display of a coronal slice of EPI_a and rigidly aligned EPI_b (first two rows), and EPI_a and rigidly aligned EPI_c (bottom two rows). The whole-scan registration is shown in (a) and the diploë-based registration is shown in (b). Note the misaligned skull and diploë in (a), especially in the fourth row, and the well aligned skull and diploë in (b). The image differences in the scalp and brain regions are visible for both cases.

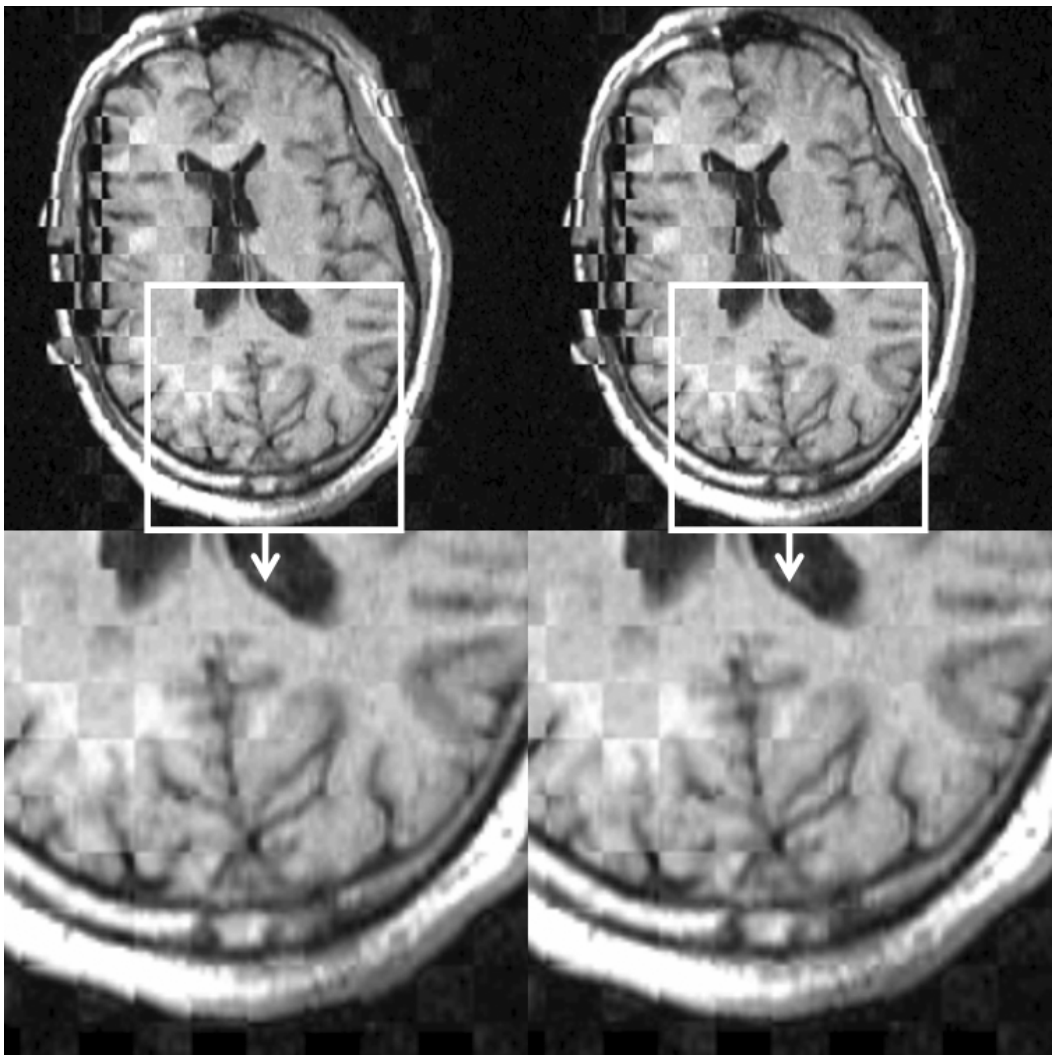

(a) (b)

Figure 8. The checkerboard display of an axial slice of TR_a and rigidly aligned TR_d. The whole-scan registration is shown in (a) and the diploë-based registration is shown in (b). Note the well aligned skull and diploë in both (a) and (b).

was similar to that in Fig. 8. The mean, standard deviation, and maximal error distance for the whole-scan registration of TR_a and TR_b were 1.2 mm, .4 mm and 2.0 mm, respectively, of TR_a and TR_c were 1.4 mm, .2 mm and 1.8 mm, respectively, and of TR_a and TR_d were 1.2 mm, .3 mm and 2.0 mm, respectively. Given the slice thickness of 2.5 mm for these scans, which can be considered the voxel size in the out-of-plane direction, the errors were certainly within the voxel size. Thus, the whole-scan and diploë-based registrations generated very similar results for these scans.

2.4.5 Semi-Automated vs. Manual Segmentation

To evaluate the quality of the segmented diploë obtained by the semi-automated tool we compared it to the manual segmentation, which was considered ground truth. We computed the Dice coefficient [81] between the semi-automated and manual segmentation for six MRI scans. The Dice coefficient, a frequently used measure of the segmentation agreement, is defined as

$$\frac{2V(S_1 \cap S_2)}{V(S_1) + V(S_2)}, \tag{2.8}$$

where S_1 and S_2 represent two segmented regions and $V(\cdot)$ is a function that returns the volume of a region. The Dice coefficient takes values between 0, in the case of no overlap, and 1, if the two regions coincide. The Dice coefficients for $DBS_{p3,a}$, $DBS_{p13,a}$, $DBS_{c1,a}$, $DBS_{c8,a}$, EPI_a and TR_a were .94, .91, .93, .88, .92 and .95, respectively, indicating a relatively high agreement between the two segmentations.

We also performed the diploë-based rigid registration using the semi-automated and manual segmentations for the six scans. The registration results corresponding to the two segmentation approaches are virtually indistinguishable by visual inspection. We computed the mean, standard deviation, and maximal distance over the diploë region between the rigid registrations when the two segmentation approaches were used and the values are reported in Table 3. The fact that the distance values in Table 3 are within the voxel size of the respective scans confirms that there is little difference in the diploë-based rigid registration if manual or semi-automated segmentation is used.

Table 3. The mean, standard deviation and maximal distance over the diploë region between the diploë-based rigid registrations using the manual and semi-automated segmentation approaches.

Scans	Mean [mm]	Std [mm]	Max [mm]
$DBS_{p3,a} - DBS_{p3,b}$	0.99	0.36	1.55
$DBS_{p13,a} - DBS_{p13,b}$	0.75	0.24	1.13
$DBS_{c1,a} - DBS_{c1,b}$	0.42	0.16	0.78
$DBS_{c8,a} - DBS_{c8,b}$	1.07	1.12	2.05
$EPI_a - EPI_b$	0.47	0.13	0.7
$EPI_a - EPI_c$	0.43	0.15	0.74
$TR_a - TR_b$	0.38	0.13	0.71
$TR_a - TR_c$	1.38	0.19	1.78
$TR_a - TR_d$	1.09	0.36	1.95

2.4.6 A Brain Shift Analysis Example

To illustrate the consequence of inaccurate rigid registration on subsequent analysis, we rigidly registered $DBS_{c1,a}$ and $DBS_{c1,b}$ using the whole-scan and diploë-based approaches, and then for both cases computed the brain shift vectors using the nonrigid registration algorithm described by [82]. A 3D view of the vectors is shown in Fig. 9. The brain shift was a result of a bilateral pneumocephalus and action of gravity. The patient was in approximately supine position, i.e. the gravity direction was approximately in the anterior-posterior direction. One can see in Fig. 9 that the red vectors are mainly in the anterior-posterior direction and that their magnitudes gradually decrease from the anterior to the posterior side of the brain. On the other hand, a rotational pattern is clearly visible in the green vectors, which is a consequence of inaccurate rotational component of the whole-scan rigid registration. The differences between the two sets of brain shift vectors are quantified in Fig. 10.

2.5 Discussion

If the goal is to non-rigidly align two scans, then one can first align them using the whole-scan (or any other) rigid registration and then follow that with nonrigid registration. Even if the whole-scan rigid registration introduces errors, a good nonrigid registration method will still accurately register the two scans, i.e. the final result will not depend on the error of the whole-scan rigid registration, assuming it is not extreme. However, if the goal is to

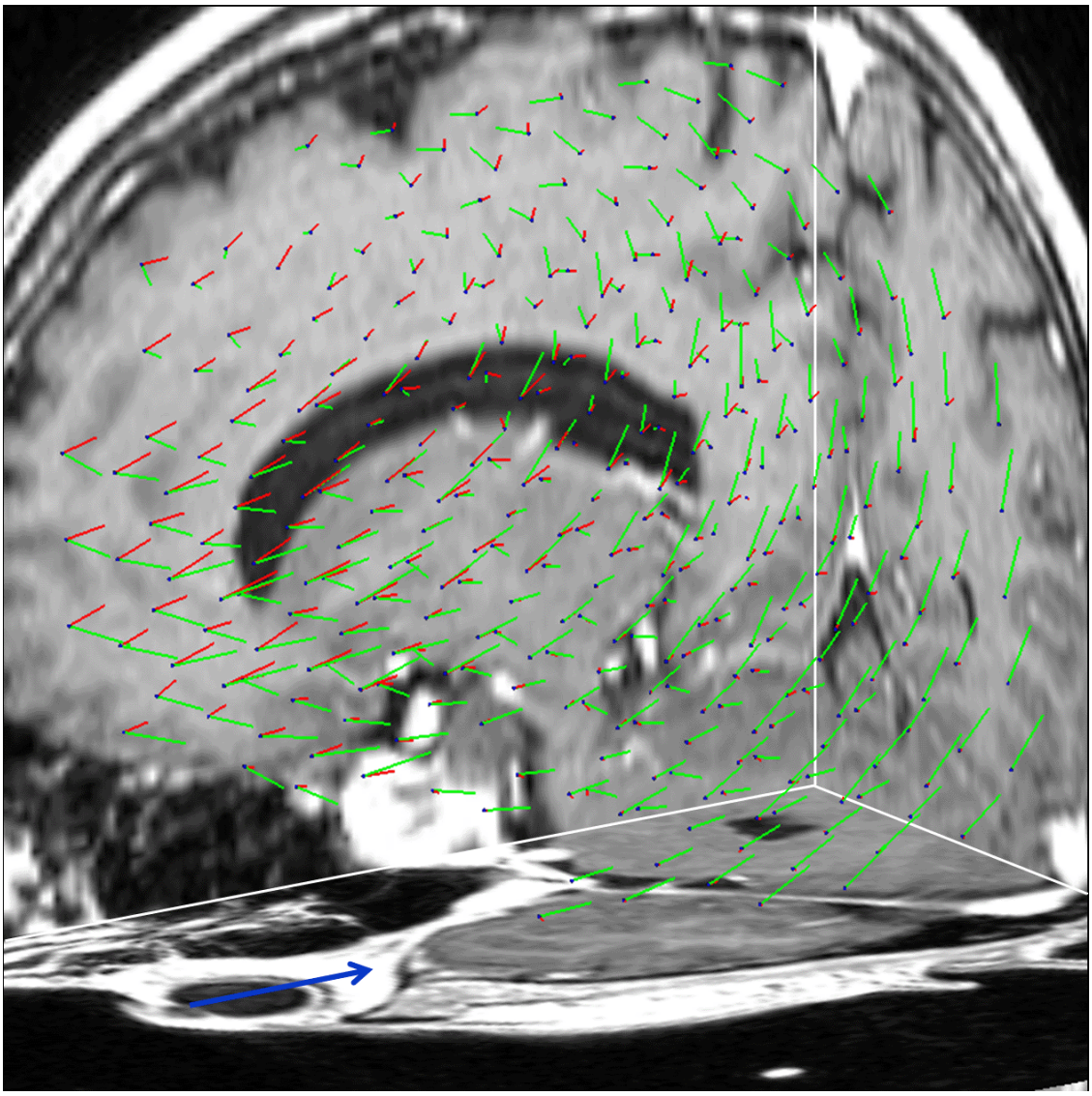

Figure 9. Three orthogonal slices of the pre-op scan of a DBS subject are shown together with brain shift vectors. The green vectors were computed using the whole-scan approach and the red vectors were computed using the diploë-based approach. The blue dots are the vector bases and the blue vector shows the gravity direction. Note the significant differences between the green and red vectors.

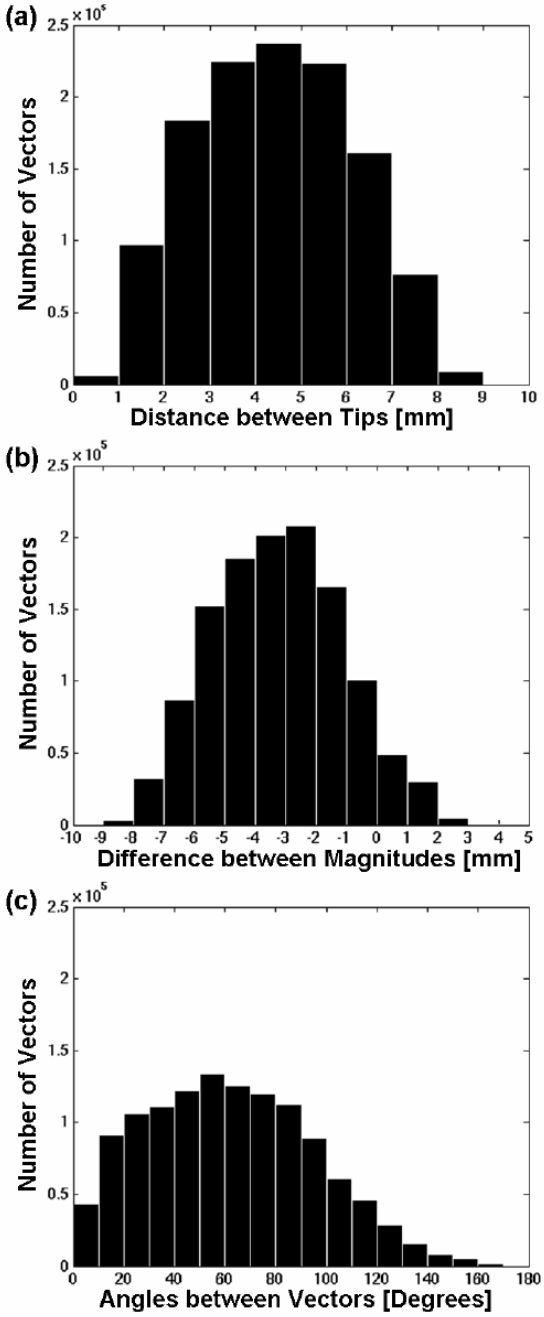

Figure 10. Histograms of (a) the distance between vector tips [mm], (b) the magnitude difference [mm] and (c) the angle between vectors [deg] are shown for the brain shift vectors corresponding to the whole-scan and the diploë-based rigid registration for DBS_{c1} subject.

measure differences between the two scans (e.g. soft tissue deformation), then the result is directly affected by the error of the rigid registration, which is illustrated in Section 2.4.6.

We showed mathematically for a one-dimensional object (Section 2.1.1) and for a general case (Section 2.1.2) that when the sum of squared differences is used as the image similarity measure for the rigid registration, the resulting registration does not align the rigid structures if there is a region that nonrigidly deformed. This conclusion can be mathematically shown to hold for other image similarity measures. In Section 2.4.1 we obtained the same conclusion using a simulated brain deformation. In the simulation we used four image similarity measures (MSD, NCC, MI, NMI) and the results were very similar for all of them. The simulation was intensionally done in 2D to be able to perform an exhaustive search for the global optimum of the image similarity measures. While the 2D rigid transformation has only three parameters (one rotation and two translations), the 3D rigid transformation had six parameters (three rotations and three translations), which makes an exhaustive search for the global optimum impractical even for a one-time simulation. The common conclusion of Sections 2.1.1, 2.1.2, and 2.4.1 is that the whole-scan rigid registration of two scans that contain rigid structures but differ by a deformed region does not align the rigid structures. To avoid the influence of nonrigid regions on the rigid registration one can segment the rigid structures and then register them.

The proposed rigid registration of serial MRI head scans is based on the diploë registration. The main advantage of this approach is that the results are independent of the scan differences inside and outside the diploë. The method requires the diploë to be segmented in one of the scans. Manual segmentation of the diploë takes several hours and the semi-automated method described in Section 2.2.1 reduces the segmentation time to less than 30 minutes for scans of 200 slices with 256 x 256 pixels. The rigid registrations based on the diploë segmented manually and by the semi-automated tool are for practical purposes identical; the difference between the two is less than the voxel size, as shown in Table 3. The user interaction in the segmentation process could be further reduced by a more sophisticated segmentation tool.

The accuracy of the whole-scan rigid registration depends on intensity, geometric and topological differences between the two scans. The pre-op and post-op scans of the DBS

subjects have mainly geometric differences. They were acquired on the same scanner with the same protocol and consequently their intensities are very similar. The topological differences between the two are minor: the post-op scans contain the implanted DBS leads (the two black dots in the midbrain region in Fig. 1b), which are relatively small and not likely to affect the rigid registration. The geometric differences between the two scans can be substantial since the brain deforms for up to several millimeters as a result of the DBS surgery (Fig. 1). These geometric differences are present over a large portion of the brain and they have a strong negative effect on the accuracy of the whole-scan rigid registration. The skull and diploë misalignment is clearly visible in the top row of Fig. 5. The maximal errors for the whole-scan rigid registration for the 25 DBS subjects were typically a few millimeters and as much as 9.4 mm (Fig. 6). Given that the size of the target structures for the implantation of the DBS leads is a few millimeters [19], the registration errors of the whole-scan approach are prohibitively large to allow for reliable analysis of the intraoperative brain deformation from the pre-op and post-op scans. In fact, they can lead to completely incorrect conclusions about the intraoperative brain deformation, as demonstrated in Sec. 2.4.6. While the rigid misalignment visible in Fig. 5 for the whole-scan registration might seem relatively small, the subsequent nonrigid registration of the pre-op and the rigidly aligned post-op scan inherits the error of the rigid registration, which in the case shown in Fig. 9 was larger than the brain shift itself in most of the brain. E.g. by using the whole-scan approach one might conclude that there was a relatively significant intraoperative deformation in the posterior part of the brain (green arrows in Fig. 9) while in fact there was almost no shift (red arrows in Fig. 9). Fig. 10 confirms that the whole-scan approach resulted in an incorrect characterization of the brain shift: the magnitudes were off for up to several millimeters and the orientations of the shift vectors were on average off for 60^o.

The pre-op and post-op scans of the epilepsy surgery patient contained a mixture of intensity, geometric and topological differences. The patient had about one hundred subdural electrodes implanted. Their presence in the post-op scans and absence in the pre-op scan represent topological changes. The implanted electrodes corrupted the magnetic field

in the MRI scanner and caused image artifacts in their vicinity, resulting in localized intensity differences between the pre-op and post-op scans. Finally, the brain underwent some deformation during the implantation of the electrodes, which represents geometric changes between the scans. The skull and diploë misalignment for the whole-scan approach are visible in the top and bottom row of Fig. 7a, but they are smaller than the corresponding misalignment in Fig. 5. While the scans of the DBS patient shown in Fig. 5 contained little intensity and topological differences, they had more geometric differences than the scans of the epilepsy patient, which is likely the reason for the larger registration error of the whole-scan approach for the DBS patient than for the epilepsy patient.

The scans of the tumor removal patient were taken intraoperatively with the same MRI scanner and protocol, which resulted in little intensity differences. The removal of the tumor represents a topological change. In addition, it caused the surrounding brain tissues to deform, i.e. it also resulted in geometric changes. Despite the topological and geometric differences between the scans there was no measurable error for the whole-scan registration, as shown by the very good alignment of the skull and diploë in Fig. 8a. A likely reason for the accurate whole-scan registration is that the geometric differences affected a relatively small portion of the brain.

The results of the three studies suggest that the geometric differences between the scans decrease the accuracy of the whole-scan registration more than the intensity and topological differences. On the other hand, the diploë-based approach is not affected by the image differences inside and outside the diploë. This resulted in a very good alignment of the skull and diploë, as visible in Figs. 5 (bottom row), 7b and 8b. There was no measurable error for all 27 serial MRI scan diploë-based registrations, which means that the method achieved sub-voxel accuracy over the diploë. Since the the diploë surrounds the brain, the rigid registration errors over the brain were the same or smaller than the errors over the diploë.

The diploë region can also have intensity differences. During the craniotomy a part of the skull with the corresponding diploë is removed, resulting in a topological difference if the patient is scanned without the removed part of the skull. The presence of electrodes, frames, or wires in the vicinity of the skull can result in intensity differences at parts of the diploë.

However, topological and intensity differences of the diploë region, unless extreme, are not likely to affect the accuracy of the diploë-based rigid registration. The diploë normally does not deform since it is contained inbetween the hard inner and outer skull bone plates. In the cases where the diploë deforms, e.g. during the normal head growth or in hydrocephalus, the rigid assumption is no longer valid and one needs to use non-rigid registration.

In this work we used T1-weighted MRI head scans. The diploë is also visible in T2-weighted MRI scans, which means that the diploë-based rigid registration can be used for the registration of any combination of T1 and T2 weighted MRI head scans.

CHAPTER 3
BRAIN SHIFT ANALYSIS

Brain shift has been recognized as a possible source of inaccuracy in DBS surgery and initial efforts to quantify this phenomenon have been reported. Winkler *et al.* [18] analyzed the brain shift of one DBS patient on the surface of the brain and around the implantation site. Khan *et al.* [19] analyzed the brain shift of 25 patients at and around the implantation site. Halpern *et al.* [20] analyzed the shortening of the length from the anterior commissure to the posterior commissure during DBS surgery and its correlation to the shift at the cortical surface in 50 patients. We also note related work by Wester and Kråkenes [22] who observed mean brain shift of 5 mm and 3.5 mm in cortical surface and thalamus, respectively, in a study of 12 stereotactic thalamotomies. The common conclusion of these studies is that brain structures in vicinity of the implantation site move for a couple of millimeters approximately in the gravity direction.

To analyze the brain shift, for each patient we non-rigidly register the pre-op and post-op MRI scans over the brain region and then compute the displacement (brain shift) vectors. The non-rigid registration is initialized with rigid registration of the two scans. We have developed a diploë-based rigid registration technique (Chapter 2) that registers two 3D MR images based on diploë only, which is a rigid structure in the head. This takes care of any differences (like deformations, tumors, etc) between the two images, which would have resulted in inaccurate rigid registration if used during the registration process. Once we have a rigidly registered pair of the pre-op and the post-op image based on diploë only, we then register them non-rigidly to get the brain deformation between them. Each step of the brain shift analysis procedure is shown in block diagram of Fig. 11. The details of each step are explained in the subsequent sections.

3.1 Methods

The basic idea for performing the brain shift analysis is to first rigidly align the pre-op and the post-op patient images based on the rigid structures only present in the head MRI, like diploë. Once the pre-op and the post-op images are satisfactorily registered using only the

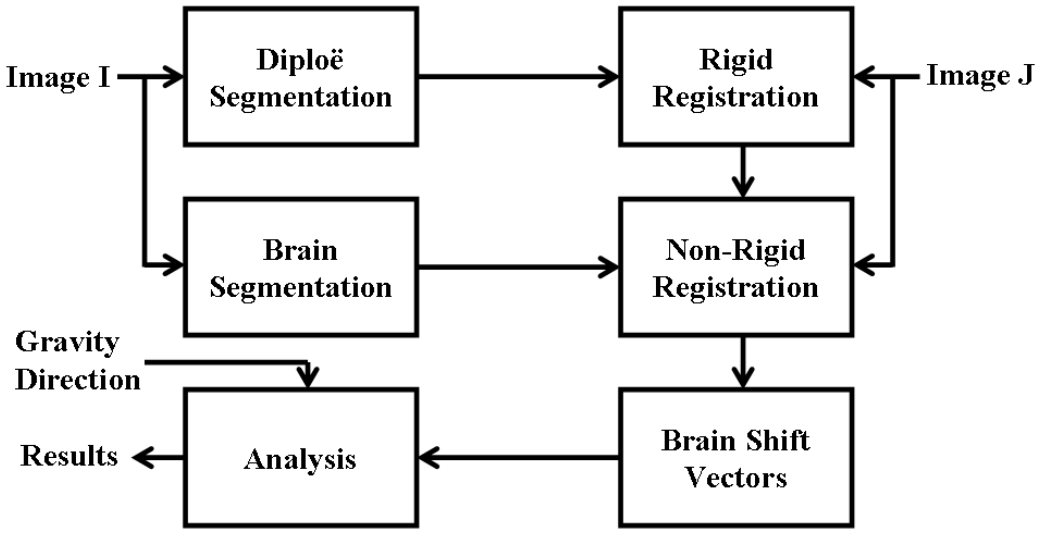

Figure 11. Block diagram of the brain shift analysis procedure. The analysis is performed using the pre-op (I) and post-op (J) 3D MR images.

diploë, any difference/mismatch/deformation present in this registered image pair is believed to be the brain shift or brain deformation during the surgery. This brain shift is measured by non-rigidly registering the rigidly registered image pair over the segmented brain tissue. The non-rigid registration parameters will give the movement or shift of the brain. Thus our brain shift analysis procedure involves image segmentation, rigid registration, non-rigid registration, and their validation as shown in a block diagram in Fig. 11.

Let I be the pre-op and J be the post-op 3D MRI scans (intensity images) of a DBS surgery patient, under study for possible brain shift during the surgery. First we segment the diploë in the pre-op image, let us call it I_d. Then the rigid registration is performed between I_d and J over the domain of segmented diploë. After performing the rigid registration, we segment the brain I_b, also in the pre-op image I, and perform the non-rigid registration between I_b and J over the domain of segmented brain in I. Rigid registration parameters are used as the initialization of the non-rigid registration algorithm and brain shift is recorded as the non-rigid brain movement. All the steps involved in our brain shift analysis procedure are validated to ensure the accuracy of each step and minimization of the overall error. Since the brain shift is only a few millimeters for DBS surgeries, a small error due to wrong segmentation and registration may easily bias the brain shift results. Once we have the

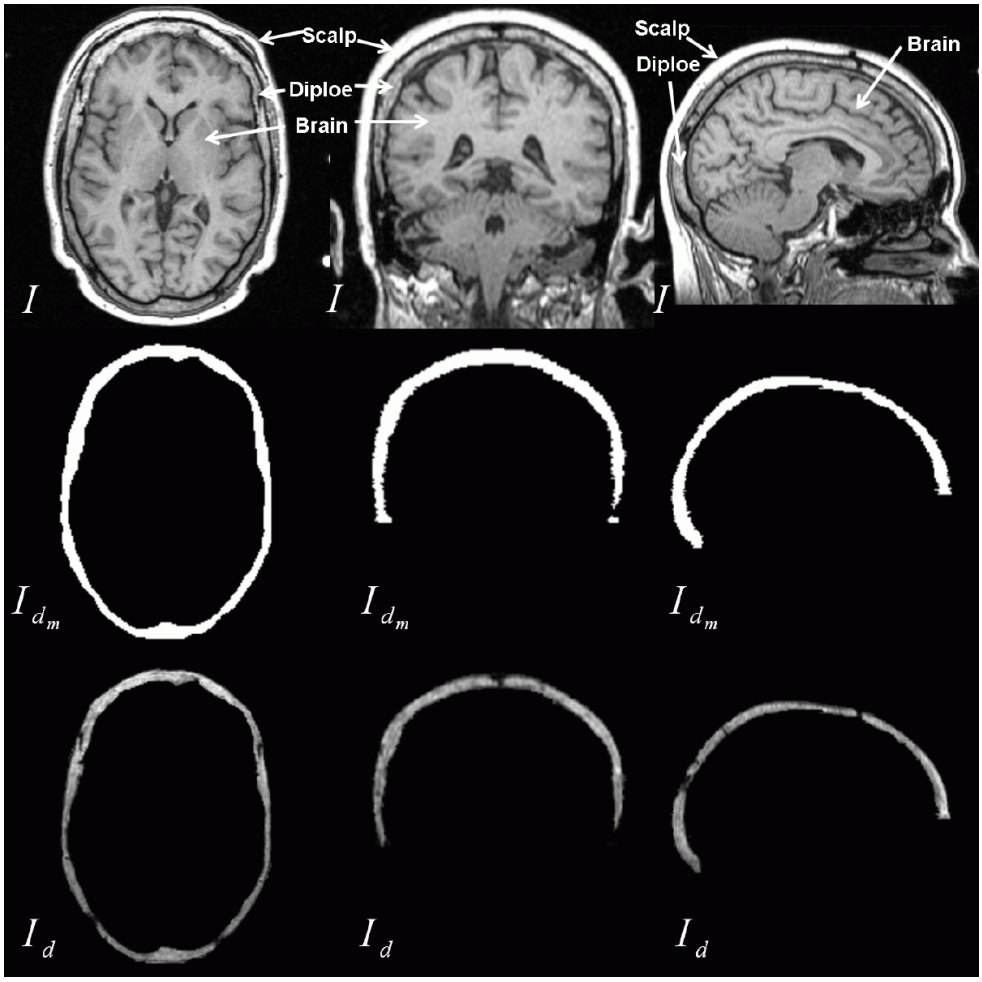

Figure 12. Axial, coronal and sagittal slices of a subject before and after the diploë segmentation using our interactive diploë segmentation procedure. Image I is the original image in which diploë is to be segmented, I_{d_m} is the mask of the segmented diploë, and I_d is the segmented diploë intensity image.

non-rigid registration parameters, we generate the brain shift vectors over entire brain and analyze them.

3.1.1 Segmentation

The diploë and the brain are segmented in the pre-op images of all the subjects for our brain shift analysis procedure. The diploë segmentation is performed on the pre-op image I using our interactive diploë segmentation procedure as explained in Chapter 2, which takes only 15-30 mins per MRI as opposed to 6-8 hrs of manual diploë segmentation work. Let N be the number of voxels in I, such that $N = m \times n \times o$, where m, n and o are the image

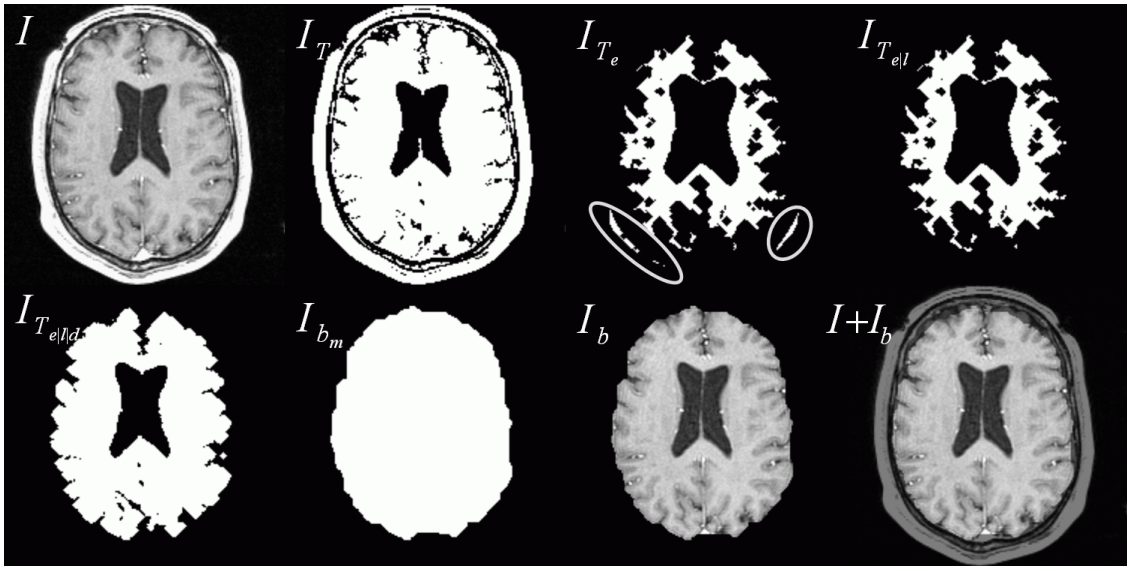

Figure 13. An axial slice of a subject as seen after each step during the brain segmentation process. Image I is the original image in which brain is to be segmented, I_T is the thresholded image of I with a threshold value of T, and I_{T_e} is the image I_T after erosions. The ellipses in image I_{T_e} show the portions of the scalp that need to be left out using largest object extraction. The image $I_{T_{e|l}}$ is the image after the largest object extraction and image $I_{T_{e|l|d}}$ is the image after dilations of $I_{T_{e|l}}$. I_{b_m} is the mask of the segmented brain, I_b is the segmented brain intensity image, and $I + I_b$ is the fused image of original intensity image and segmented brain intensity image.

sizes in X, Y and Z directions respectively. Then $I(x, y, z)$ would represent an intensity of a voxel at (x, y, z), where $x = 1 \rightarrow m$, $y = 1 \rightarrow n$ and $z = 1 \rightarrow o$. The interactive diploë segmentation procedure gives I_{d_m} (middle row of Fig. 12), same size as I, which is the mask of the segmented diploë in I with ones where diploë is present and zeros elsewhere. The image I_d (bottom row of Fig. 12), given by $I_d = I \otimes I_{d_m}$ ($\otimes$ represents element wise multiplication of two matrices), is the diploë intensity image that carries only the intensity values of the voxels belonging to the diploë and zero elsewhere.

The brain segmentation is done using morphological methods like thresholding, dilation, erosion, largest object extraction and region filling. The idea is to threshold the head scan and divide it in to major head structures by breaking the links in between. Brain being the largest object in the head MRI can thus be easily extracted. The first step to segment the brain in the pre-op image I is to threshold it with a suitable value T. The thresholded image I_T (Fig. 13) of image I is a binary image given by:

$$I_T(x,y,z) = \begin{cases} 0 & \text{if } I(x,y,z) < T, \\ 1 & \text{if } I(x,y,z) \geq T. \end{cases}$$

The next step is to erode the thresholded image in order to break the week links in the binary image. The erosion of I_T by a structuring element S in Z^3 is represented as $I_T \ominus S$ and given by

$$I_T \ominus S = \{u \mid (S)_u \subseteq I_T\}, \tag{3.1}$$

where $(S)_u$ is the shifting of S by u. Thus the erosion of I_T by S is the set of all points u, such that S translated by u, is contained in I_T. The erosion step is repeated n_e number of times to give $I_{T_e} = (I_T \ominus S)_{n_e}$, where I_{T_e} (Fig. 13) is image I after thresholding and erosions. The image I_{T_e} in Fig. 13 shows the eroded image that mainly contains the brain and some portions of the skin and scalp (shown in ellipses). The brain being the largest connected object is extracted in the thresholded and eroded image I_{T_e}. Let $X_k = (x,y,z)^T$ be the location of the voxels (^{T} means transpose), then the connected object Y in binary eroded image I_{T_e} is given by the following iterative expression,

$$X_k = \{(X_{k-1} \oplus k) \cap I\}, \quad k = 1,2,3,.... \tag{3.2}$$

where $X_{k-1} \oplus k$ is a dilation process explained by equation (3.3), X_0 may be any starting voxel with value 1. If $X_k = X_{k-1}$, the algorithm is terminated and $Y = X_k$. We find all the connected objects in I_{T_e} and select the largest connected object with the largest volume. The voxels belonging to this largest connected object are left as 1 and the remaining voxels are set to 0. The resulting binary image is denoted as $I_{T_{e|l}}$ (Fig. 13), where l shows the largest connected object only.

The image $I_{T_{e|l}}$ is dilated n_d number of times to bring to the size of the original object. The dilation of $I_{T_{e|l}}$ by a structuring element S in Z^3 is represented as $I_{T_{e|l}} \oplus S$ and given by

$$I_{T_{e|l}} \oplus S = \{u \mid [(\hat{S})_u \cap I_{T_{e|l}}] \subseteq I_{T_{e|l}}\} \tag{3.3}$$

where $\hat{S}$ is the reflection of S and $(\hat{S})_u$ is the shifting of this reflection by u. The dilation of $I_{T_{e|l}}$ by S is the set of all displacements, u, such that $I_{T_{e|l}}$ and $\hat{S}$ overlap by at least one element. The resulting binary image is denoted as $I_{T_{e|l|d}}$ (Fig. 13), given by $I_{T_{e|l|d}} = (I_{T_{e|l}} \oplus S)_{n_d}$, where d shows the dilations.

The thresholded, eroded, largest object extracted and dilated image, $I_{T_{e|l|d}}$, still has holes (black regions) in the brain area (as seen in the $I_{T_{e|l|d}}$ image of Fig. 13) because CSF voxels have intensity values less than T and were thus left out in the thresholding step. In order to include CSF region in the mask image of the segmented brain, I_{b_m} (Fig. 13), we dilate and erode $I_{T_{e|l|d}}$ for n_m times with a structuring element S_m to fill up the CSF holes. Therefore,

$$I_{b_m} = ((I_{T_{e|l|d}} \oplus S_m)_{n_m} \ominus S_m)_{n_m}, \tag{3.4}$$

and

$$I_b = I \otimes I_{b_m}, \tag{3.5}$$

where I_b (Fig. 13) is the segmented brain intensity image of I with 0 at voxel locations outside the brain. The extraction of connected objects was performed using 6/26-neighborhood in 3D space. The S_m used was simple set of ones of dimension $3 \times 3 \times 3$, whereas S used was again of the same dimension as S_m and given by:

$$S_m(a,b,c) = \begin{cases} 1 & \text{if} \geq 2 \text{ out of a,b and c are even} \\ 0 & \text{else,} \end{cases}$$

where a,b,c=1,2,3. Fig. 14 shows typical diploë and brain segmentations.

3.1.2 Rigid Registration

The currently used rigid registration algorithms use all the image information (whole head scan) and are therefore affected by the brain shift between the pre-op and the post-op images. We use diploë-based rigid registration as explained in Chapter 2. The diploë-based registration algorithm optimizes the six rigid transformation parameters, three rotations $(\Theta_r, \Theta_p, \Theta_y)$ and three translations (t_x, t_y, t_z), where $\Theta_r, \Theta_p, \Theta_y$ stand for roll, pitch and yaw

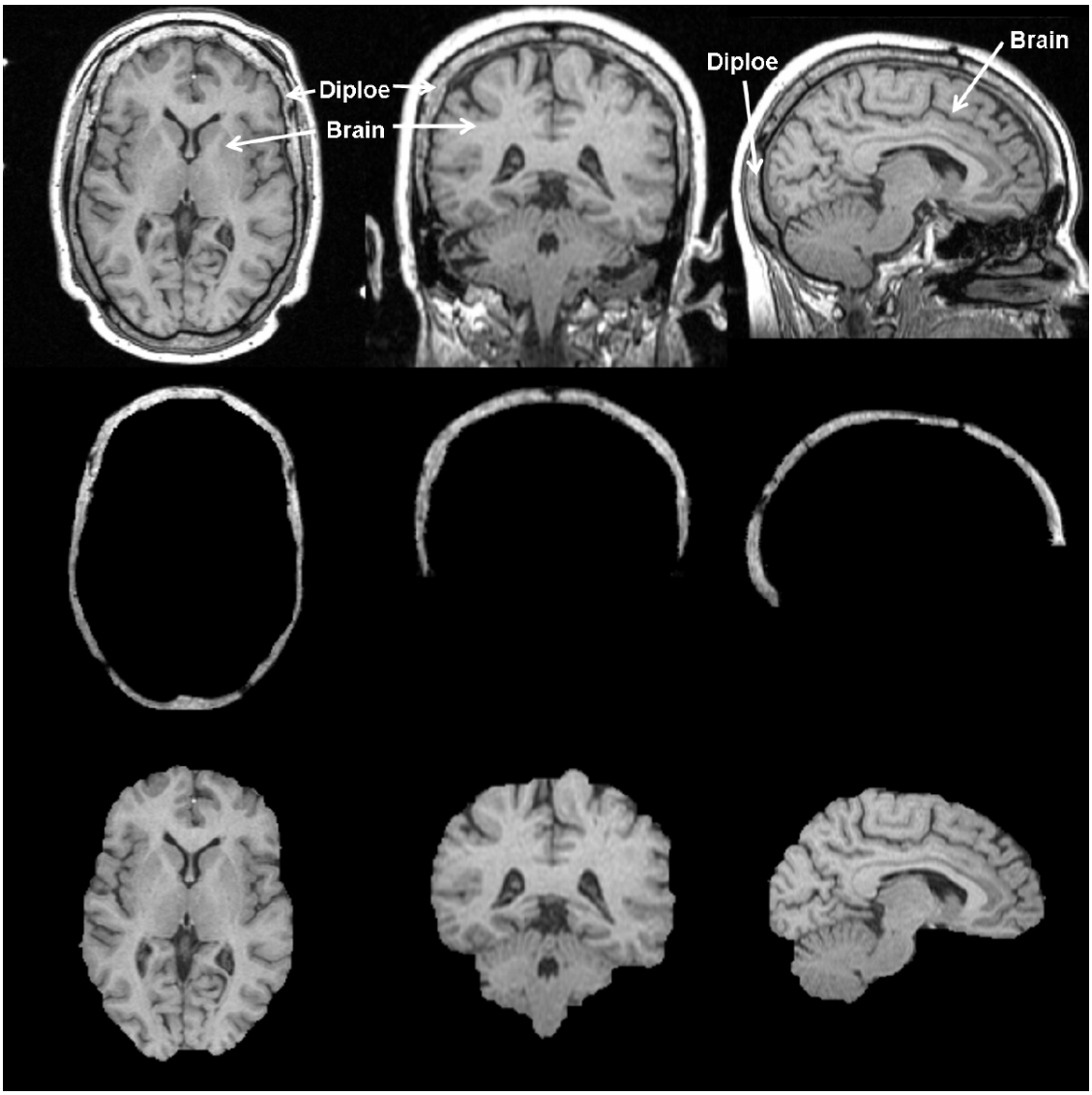

(a) (b) (c)

Figure 14. Axial (a), coronal (b) and sagittal (c) slices of MRI head scan (first row), diploë segmentation (second row) and brain segmentation (third row) are shown for one subject.

angles respectively, and t_x, t_y, t_z are the translations in the three axis directions. The diploë is segmented in only pre-op image I, and this segmented dipoë is used for the registration with the other image. The corresponding image portion in the post-op image J is found by optimizing the six rigid transformation parameters over a similarity measure. The NMI [78] is used as the image similarity measure between the two images. The NMI is maximized using gradient descent method as given by:

$$T_R(\Theta_r, \Theta_p, \Theta_y, t_x, t_y, t_z) = \arg\max_{T_R} NMI(I_d, J(T)), \tag{3.6}$$

where T_R is the rigid body transformation. The optimization algorithm runs iteratively till the NMI maxima is achieved. We use multi resolution approach to avoid the false maxima and speed up the algorithm. The multi resolution approach is implemented by changing the step size for the numerical computation of the gradient at each resolution level.

3.1.3 Non-Rigid Image Registration

Our non-rigid registration algorithm uses thin plate splines (TPS) to define the non-rigid transformation from the pre-op image I to the post-op image J [83]. Non-rigid registration is performed over the domain of segmented brain in image I. Thus we can say that the registration is done from I_b to J over the domain of $I_{b_m} = 1$. The basic idea in using TPS as an interpolant is to minimize the bending energy of the splines while interpolating the specified set of points i.e. sum of squares of all second order partial derivatives is minimized. The space integral of the second order derivatives of the mapping function is one of the simplest smoothness measures which is used in TPS. If $f : \mathbf{R}^3 \rightarrow \mathbf{R}$ is a 3-dimensional TPS mapping function, the bending energy (E) to be minimized is given by:

$$\begin{aligned} E=&\iiint_{R^3} \left(\frac{\partial^2 f}{\partial x^2}\right)^2 + \left(\frac{\partial^2 f}{\partial y^2}\right)^2 + \left(\frac{\partial^2 f}{\partial z^2}\right)^2 \\ &+2\left(\frac{\partial^2 f}{\partial x \partial y}\right)^2 + 2\left(\frac{\partial^2 f}{\partial x \partial z}\right)^2 + 2\left(\frac{\partial^2 f}{\partial y \partial z}\right)^2 dx\, dy\, dz \end{aligned} \tag{3.7}$$

TPS is the fundamental solution to the biharmonic equation,

$$\Delta^2 U = \left(\frac{\partial^2}{\partial x^2} + \frac{\partial^2}{\partial y^2} + \frac{\partial^2}{\partial z^2}\right)^2 U \propto \delta_{(0,0,0)}, \tag{3.8}$$

in $\mathbf{R}^3$, and has the form $U(r) = |r|$ in 3D, where r is distance $\sqrt{x^2+y^2+z^2}$. The right hand side of equation (3.8) is proportional to the delta function, $\delta_{(0,0,0)}$, zero everywhere except at origin but having an integral equal to 1.

The TPS functions are globally smooth and can be easily separated into affine and non-affine components. Let $\{P \mid P_1 = (x_1, y_1, z_1),\ P_2 = (x_2, y_2, z_2),\ \cdots,\ P_n = (x_n, y_n, z_n)\}$ and $\{Q \mid Q_1 = (x'_1, y'_1, z'_1),\ Q_2 = (x'_2, y'_2, z'_2),\ \cdots,\ Q_n = (x'_n, y'_n, z'_n)\}$ be two sets of corresponding landmark points in images I and J respectively, where (x, y, z) represents the physical domain of image I and (x', y', z') represents the physical domain in image J. The set of points P and Q define the non-rigid transformation from I to J. A TPS interpolation mapping function that maps the domain of image I to the domain of image J can be written as

$$f(x,y,z) = \overbrace{a_1 + a_x x + a_y y + a_z z}^{\text{affine}} + \underbrace{\sum_{i=1}^{n} w_i U(\mid P_i - (x,y,z) \mid)}_{\text{non-affine}}, \tag{3.9}$$

where a_1, a_x, a_y and a_z are the affine coefficients, and w_i are the weights. If we know a_1, a_x, a_y, a_z, and w_i, we can map every point in image I to image J using the TPS transformation of equation (3.9). In 3D, it is done by using three separate TPS functions f_x, f_y and f_z which model the displacement of the landmark points in x, y and z directions respectively and we arrive at a vector-valued function $\mathbf{F}$ which maps each point of the image I into a new point in the image J as

$$(x, y, z) \rightarrow (f_x(x, y, z), f_y(x, y, z), f_z(x, y, z)). \tag{3.10}$$

The values of a_1, a_x, a_y, a_z, and w_i for a given set of P and Q can be computed in the following way. Let $r_{ij} = \mid P_i - P_j \mid$ be the distance from point i to point j in image I, then define matrices

$$K = \begin{bmatrix} 0 & U(r_{12}) \ldots U(r_{1n}) \\ U(r_{21}) & 0 & \ldots U(r_{2n}) \\ \vdots & \vdots & \ddots & \vdots \\ U(r_{n1}) U(r_{n2}) \ldots & 0 \end{bmatrix}_{n \times n} , \tag{3.11}$$

$$P = \begin{bmatrix} 1 x_1 y_1 z_1 \\ 1 x_2 y_2 z_2 \\ \vdots \vdots \vdots \vdots \\ 1 x_n y_n z_n \end{bmatrix}_{n \times 4} , \tag{3.12}$$

and

$$L = \left[\begin{array}{c|c} K & P \\ \hline P^T & O \end{array}\right]_{(n+4)\times(n+4)} , \tag{3.13}$$

where O is a 4×4 matrix of zeros. Let $V = (v_1, ..., v_n)$ be any n-vector, and write $Y = (V \mid 0\ 0\ 0\ 0)^t$, a column vector of length $n + 4$. Define the vector $W = (w_1, ..., w_n)$ and the coefficients a_1, a_x, a_y, a_z are given by

$$L^{-1}Y = (W \mid a_1\ a_x\ a_y\ a_z). \tag{3.14}$$

We use $V = (x'_1, \ldots, x'_n)$ to get f_x, $V = (y'_1, \ldots, y'_n)$ to get f_y and $V = (z'_1, \ldots, z'_n)$ to get f_z using equations (3.9) and (3.14).

A multi-resolution approach was adopted in the implementation of the non-rigid registration algorithm with three resolutions of 40 mm, 20 mm and 10 mm of node spacing as shown in Fig. 15. A grid of nodes with 40 mm spacing (as shown in the left most image of Fig. 15) was placed over the segmented brain image at the lowest resolution level. The corresponding nodes in the post-op image were initially set using the transformation obtained by the rigid registration. The optimization was done using the Powell's method [84] for moving the nodes in order to maximize NMI at each resolution. The iterative maximization of NMI yields the final transformation

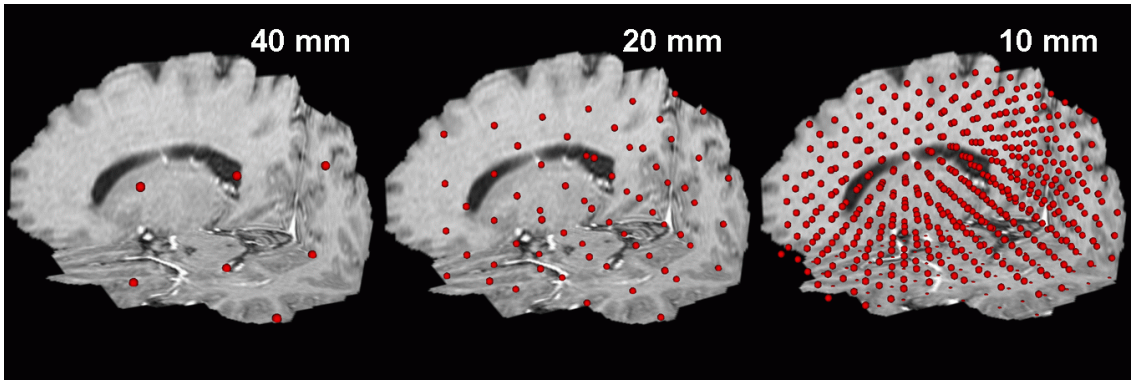

Figure 15. The nodes in the pre-op scan at three resolution levels shown together with three orthogonal slices of the segmented brain.

$$\mathbf{T}_{TPS}^{optimal} = \arg\max_{\mathbf{T}_{TPS}} NMI(I(B), J(\mathbf{T}_{TPS}(B))). \tag{3.15}$$

$T_{TPS}^{optimal}$ is the optimal TPS transformation from the pre-op to the post-op image. Once a maximum of NMI was achieved at a given resolution, the node spacing was reduced to move to a higher resolution and the optimization procedure was repeated. The TPS parameters corresponding to the maximal NMI at the highest resolution were used to compute the brain shift vectors over the segmented brain region.

3.1.4 Brain Shift Analysis

At any point $\mathbf{r} \in B$ one can compute the displacement, i.e. the brain shift vector as

$$\mathbf{u}(\mathbf{r}) = \mathbf{T}_{TPS}^{optimal}(\mathbf{r}) - \mathbf{r}. \tag{3.16}$$

Since the brain shift vectors can be determined over the entire brain, one can compute the distribution of the brain shift magnitude and orientation over the entire brain, the corresponding mean, standard deviation and maximal values, as well as analyze brain shift at any point of interest.

3.1.5 DBS Lead Dislocation Computation

The actual location of the implanted DBS lead is in general at a certain distance from the intended site of implantation. We refer to the vector from the intended site of implantation to the actual location of the implanted DBS lead as the "DBS lead dislocation" and we

correlated it to the brain shift at the location of the implantation. The intended site of the implantation was recorded by software during MEM in the coordinate system of the stereotactic frame and then mapped to the coordinate system of the pre-op image using the surgical navigation system. The actual location of the implanted DBS lead was manually determined with the same proprietary software by superimposing an exact 3D model of the DBS electrode on its image representation in the post-op MRI. The location was then mapped to the coordinate system of the pre-op image using the diploë-based rigid registration between the pre-op and the post-op image. The center of the bottom edge of contact 0 was chosen in each case as the reference point. Once the two reference points were in the same coordinate system, we computed the DBS lead dislocation as the vector from the first to the second point. DBS lead dislocation vector may be used as a measure of the implantation inaccuracy.

3.1.6 Statistical Analysis

For the statistical analysis we computed the square of the Pearson correlation coefficient (r^2 value) and used the two-sided Student's t-test to determine the significance (p value) of the correlation. For each set of data we plotted the regression line to show the trend.

3.2 Study I

3.2.1 Subjects

Pre-op and post-op T1-weighted MR images of 25 subjects that underwent DBS surgery were used for this brain shift analysis study. The Fast Field Echo protocol with gradient echo (flip angle = 30, repetition time TR = 25 ms and echo time TE = 4.6 ms) was used to acquire both the pre-op and the post-op images. Pre-op MRI images had around 200 slices of 256 x 256 pixels with in-plane resolution of 1 mm and slice thickness of around 0.9 mm. Fifteen post-op MRI images had 120 slices of 256 x 256 pixels with in-plane resolution of 1 mm and slice thickness of 0.8 mm, while 10 post-op MRI images had 150-200 slices of 256 x 256 pixels with in-plane resolution of 1 mm and slice thickness of 0.8 mm. All images were acquired using a Philips Medical System Gyroscan 1.5T MRI scanner. Pre-op images were acquired in the axial plane while post-op images were acquired in the coronal plane. The relevant details of the 25 DBS subjects used for this study are given in Table 1.

3.2.2 Results

First study of brain shift analysis was mainly based on the four points manually selected in the pre-op image: the posterior edge of the anterior commissure (AC), the anterior edge of the posterior commissure (PC), the medial-anterior corner of left putamen (PL) and the medial-anterior corner of right putamen (PR).

Fig. 16 shows the result of the two-stage registration process for a representative subject using checkerboard displays. A detailed visual inspection of the registered images for all the 25 subjects showed that there was no measurable misalignment of the diploë after the rigid registration and of the brain tissues after the non-rigid registration, which means that the registration had subvoxel accuracy.

Fig. 17 shows the brain shift vectors at AC, PC, PL and PR of one of the subjects. The distributions of the shift magnitude for the four points are shown in Fig. 18. The mean ± SD (max) shift magnitudes for the AC, PC, PL, PR points were 1.8 ± 0.7 (2.9) mm, 1.6 ± 0.8 (2.9) mm, 1.8 ± 0.9 (3.5) mm, and 2.0 ± 0.7 (3.9) mm, respectively. The mean ± SD (max) shift magnitudes of all the shift vectors combined was 1.8 ± 0.8 (3.9) mm.

Fig. 19a shows the AC, PC, PL and PR shift vectors of one of the subjects, projected to the axial plane. A high directional correlation of the four shift vectors indicates that the diencephalic structures shifted approximately in the same direction. For each subject we computed the six angles between the four shift vectors. The distribution of the average angle for the 25 subjects is shown in Fig. 19b and the mean average angle was 22°.

Fig. 20 shows the signed percentage of the recorded brain shift vectors in the direction of gravity and direction of the DBS lead implantation. The signed percentage of a vector in the direction of another vector is defined as the cosine (multiplied by 100%) of the angle between the two vectors. Note that the signed percentage can take values from -100% to 100%. A positive signed percentage means that the angle between the two vectors is smaller than 90°, while a negative signed percentage means that the angle is larger than 90°. If the two vectors have exactly the same direction (the angle was 0°) the signed percentage is 100% and if they are pointing exactly in opposite directions (the angle is 180°) the signed percentage is -100%. The direction of the DBS lead implantation was computed using the post-op images, but the exact gravity direction is unknown as it was not recorded during

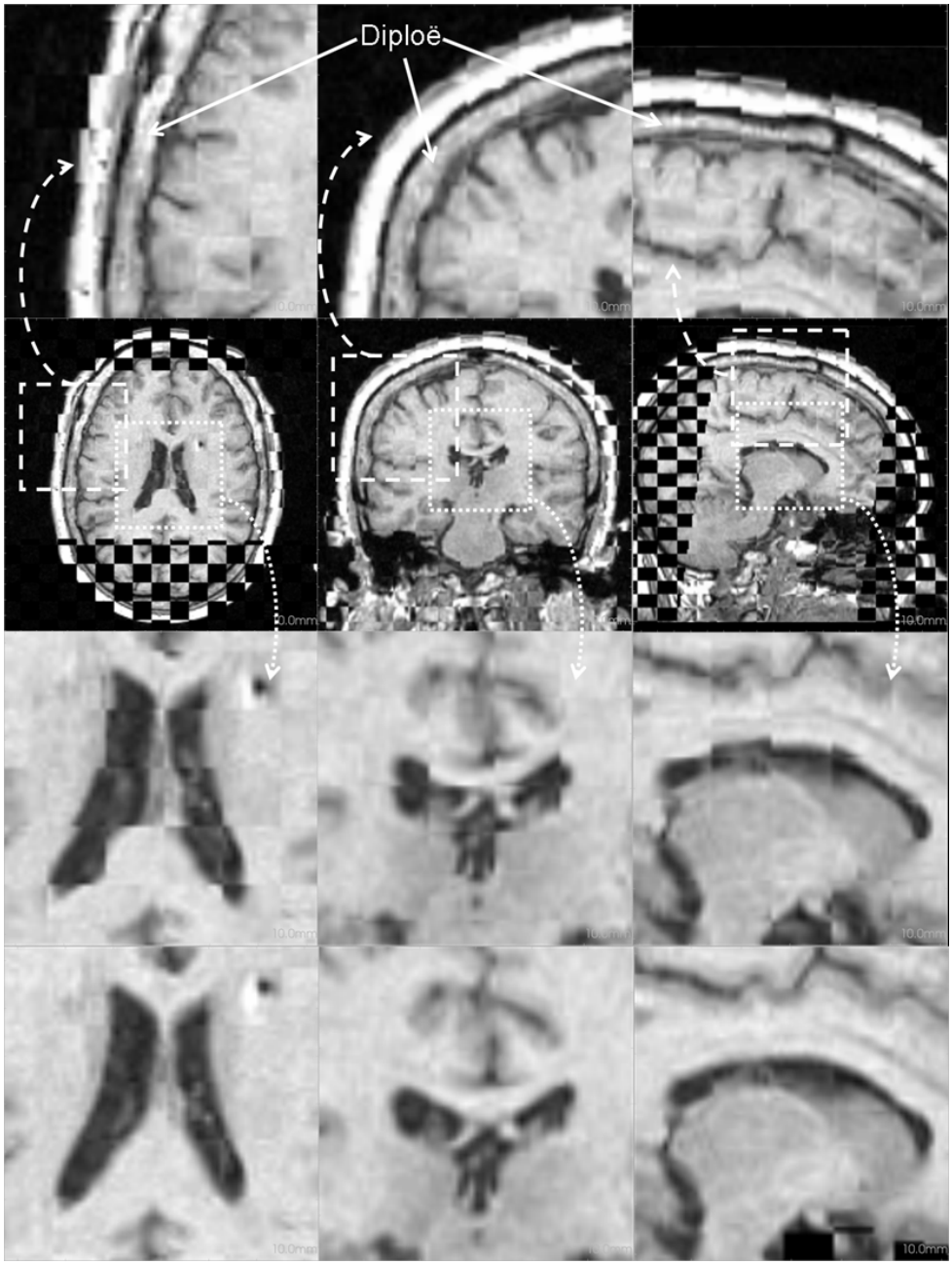

Figure 16. The result of the two-stage registration process for one of the subjects is shown in axial (first column), coronal (second column), and sagittal (third column) views. The second row shows the full slices of the rigidly aligned pre-op and post-op images, while the first row shows the corresponding zoomed-in skull regions and the third row shows the corresponding zoomed-in ventricular regions, all after the rigid registration. The fourth row shows the same ventricular regions after the non-rigid registration. All the views contain checkerboard displays of the pre-op image and the registered post-op image. Note the good alignment of the diplo in the top row, which suggests that the rigid registration was accurate. The misalignment of the outer edge of the skin in the pre-op and the post-op image in the top row was likely caused by the deformation of the soft tissues outside the skull. The misaligned ventricles in the third row show that the soft structures deformed between the two scans, while the well aligned ventricles in the fourth row suggest that the non-rigid registration was accurate.

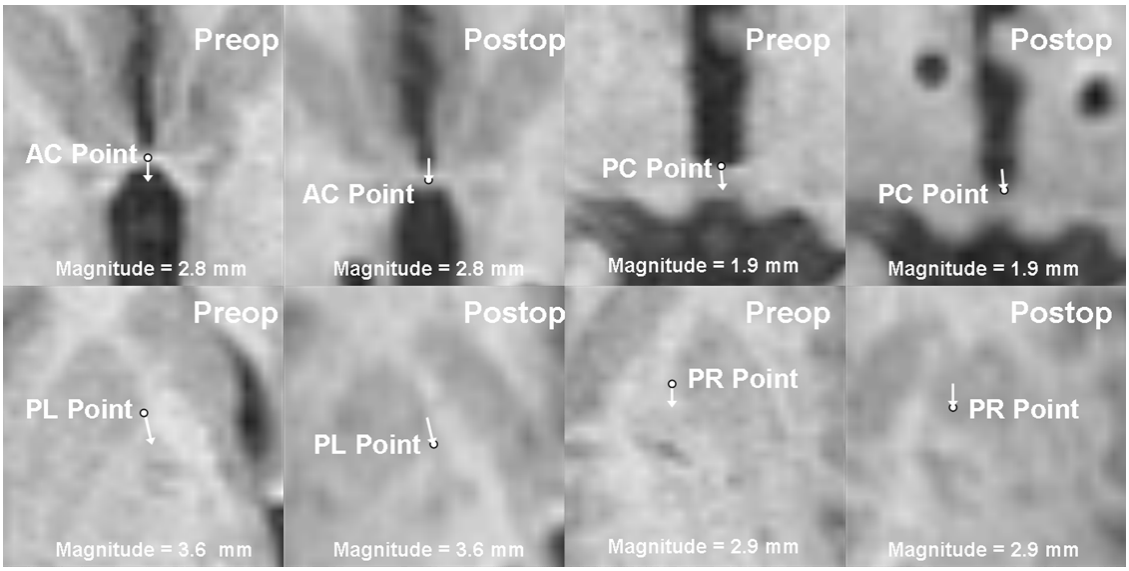

Figure 17. Brain shift vectors of AC, PC, PL and PR points (marked as white points) superimposed on the axial slices of the pre-op and the rigidly registered post-op image of a subject. The magnitude and projection to the axial plane of each brain shift vector are shown in the pre-op image and in the corresponding position in the post-op image.

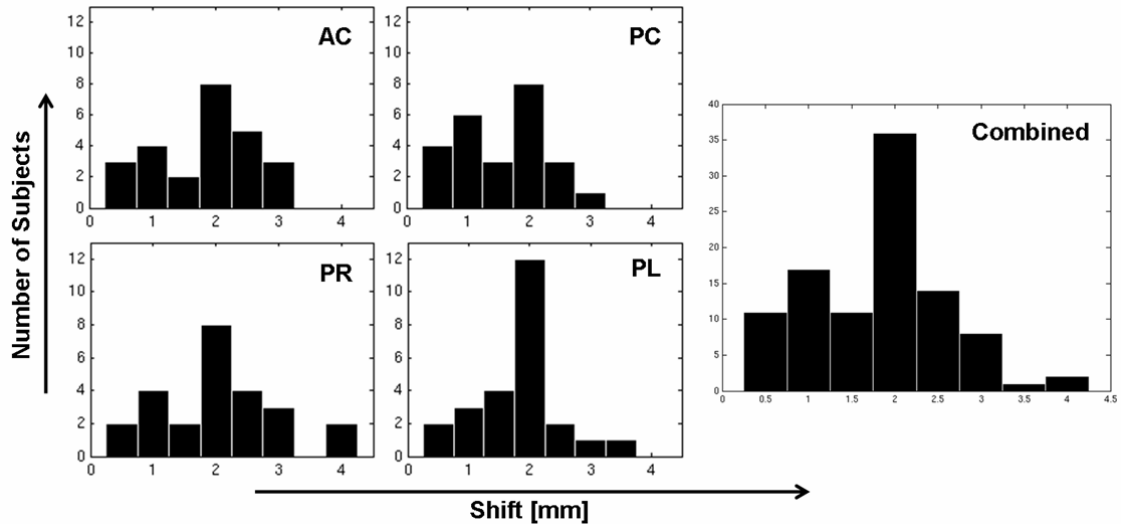

Figure 18. Histograms of the magnitude of AC, PC, PL, PR and combined shifts for the 25 subjects.

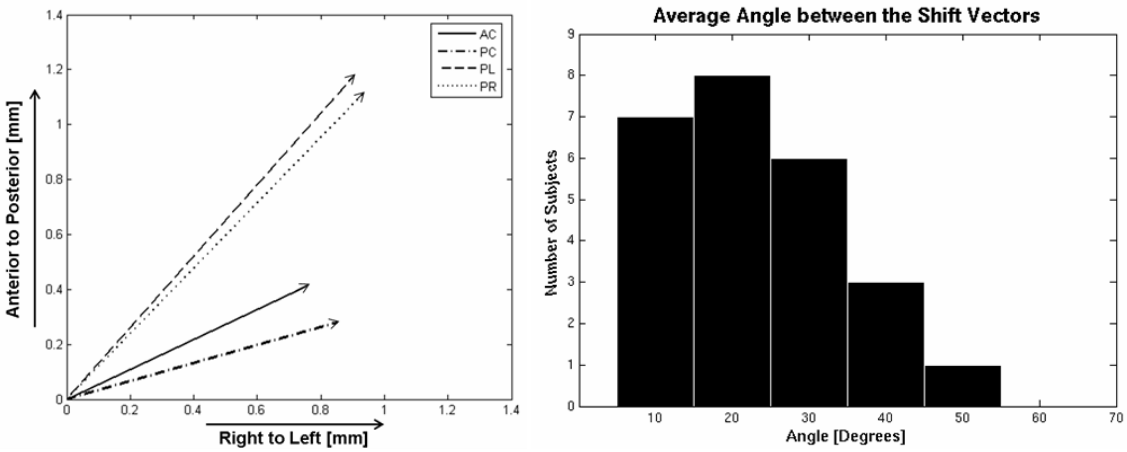

(a) (b)

Figure 19. Shift vectors for a subject projected to the axial plane (a) and the histogram of the average of the six types of angles between the shift vectors of the 25 subjects (b).

the surgery. Since the patients were in a quasi-supine position during the surgery with head elevated at an angle of approximately 5° to 20°, the main component of the gravitational force was in the anterior posterior direction. As can be seen, the majority of the shift vectors were in the gravity direction, whereas the direction of the DBS lead did not have a strong influence on the shift direction.

To see if the amount of shift was related to the time after the surgery, we evaluated the average shift versus the delay (time between the end of the surgery and the post-op scan time). The scatter plot ($r^2 = 0.04$, $p = 0.30$) with the regression line is shown in Fig. 21 (left image). Similarly, the scatter plot between the average shift and length of the surgical procedure ($r^2 = 0.02$, $p = 0.49$) together with the regression line is shown in Fig. 21 (right image). These data demonstrate no relationship between the length of surgery or the delay to post-op imaging and the degree of brain shift.

The case with the largest recorded shift (3.9 mm) had a transventricular DBS lead implantation (Fig. 22a). Another case with a transventricular DBS lead implantation is shown in Fig. 22b. A case with bilateral pneumocephalus had shift which was above the average (Fig. 22c), while another case with bilateral pneumocephalus (Fig. 22d) had shift that was below the average. Since only three patients had a transventricular insertion of the DBS electrode, and only two patients had bilateral pneumocephalus, the relevance of

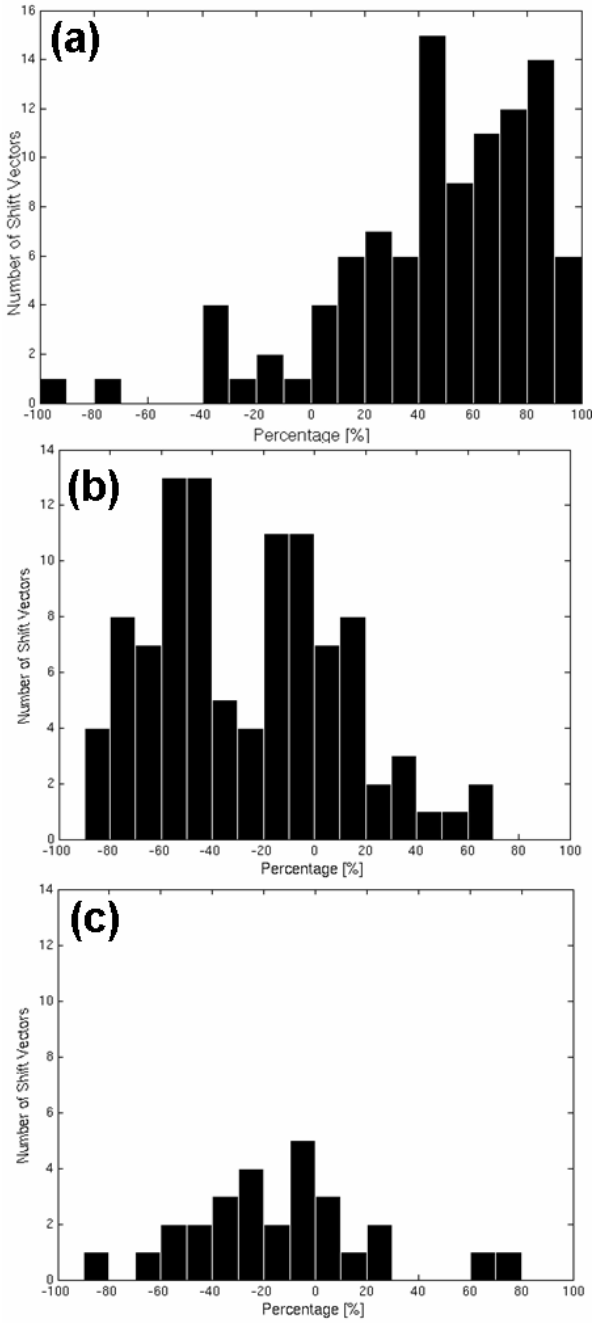

Figure 20. Histograms showing the signed percentage of the recorded brain shift in the direction of gravity (a), direction of the first DBS lead (b), and direction of the second DBS lead (c).

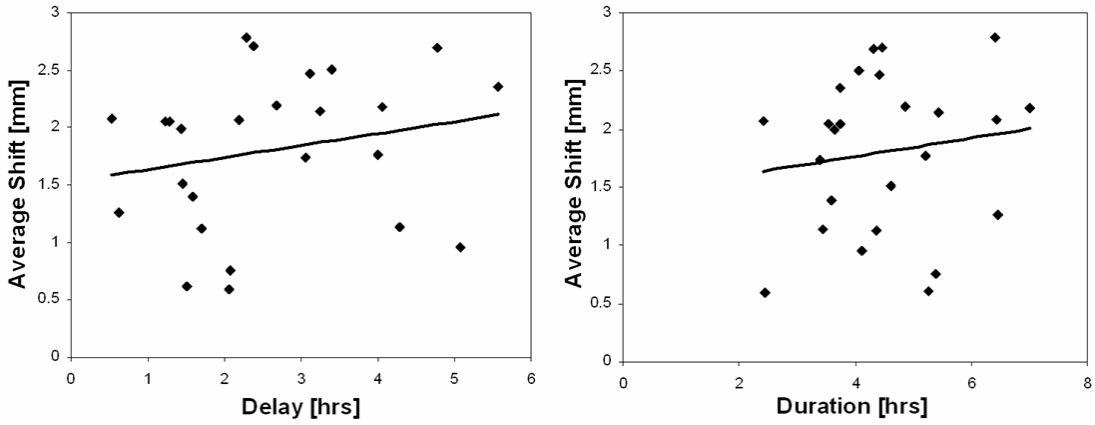

Figure 21. The average of the four types of brain shift vectors vs. delay (left image) and the average of the four types of brain shift vectors vs. duration of the surgery (right image). The regression lines are shown in both graphs.

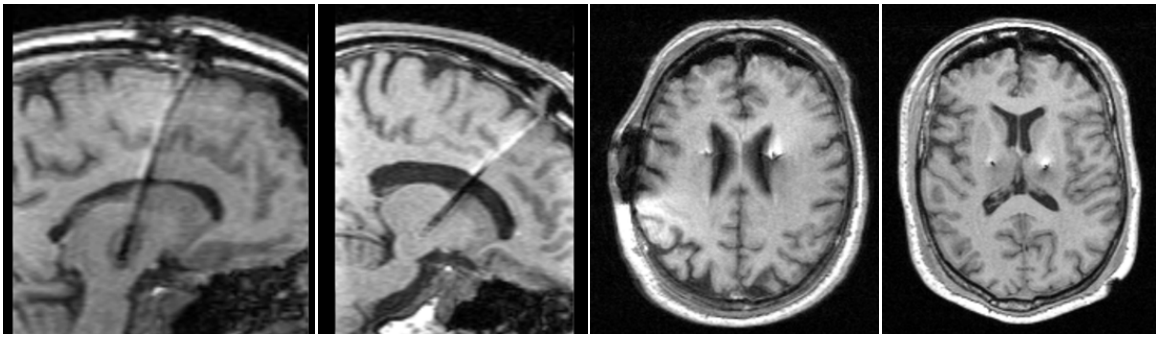

(a) (b) (c) (d)

Figure 22. Examples of post-op MRI of subjects with transventricular DBS lead implantation (a and b) and bilateral pneumocephalus (c and d). Their mean/max shifts were (a) 2.7/3.9 mm , (b) 2.0/2.8 mm, (c) 2.1/2.9 mm, and (d) 1.5/1.9 mm.

these factors to the degree of shift could not be addressed rigorously.

To test if there was a relationship between the brain shift and the dislocation of the DBS lead (determined as the vector from the intended site of implantation to the actual DBS lead position in the post-op scan), we correlated the components and magnitude of the brain shift vector at the intended site of implantation with the corresponding components and magnitude of the dislocation vector. The scatter plot of the magnitudes of the two vectors ($r^2 = 0.25$, $p < 0.05$) with the regression line is shown in Fig. 23. The correlation between the magnitudes of the two vectors was mainly caused by the correlation of their respective superior-to-inferior components (left-to-right components: $r^2 = 0.04$, $p = 0.42$;

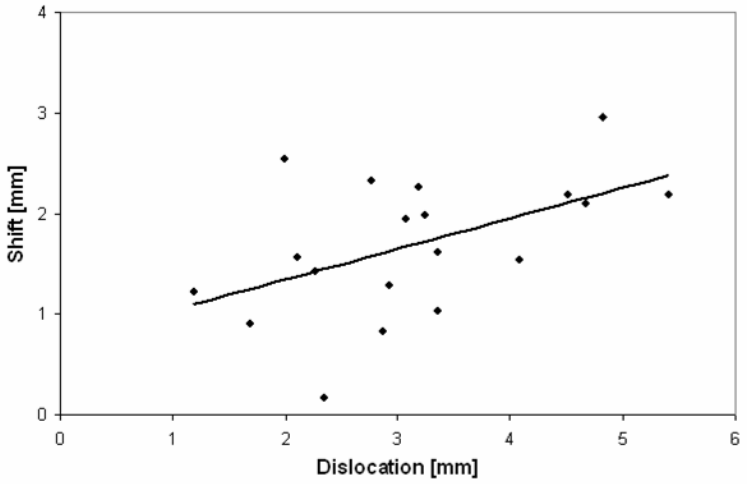

Figure 23. The magnitude of the brain shift vector at the intended site of implantation vs. the magnitude of the dislocation of the DBS lead.

anterior-to-posterior components: $r^2 = 0.01$, $p = 0.66$; superior-to-inferior components: $r^2 = 0.22$, $p < 0.05$).

Finally, we tested a possible relationship between the shift magnitude and the number of microelectrode tracks necessary to complete the mapping ($r^2 = 0.001$, $p = 0.87$) and the relationship between the shift magnitude and the distance from the initially selected target to the final intended site of implantation ($r^2 = 0.035$, $p = 0.44$) and in either case we found no significant correlation.

3.2.3 Discussion

A brain shift analysis was done on 25 subjects that underwent DBS surgery. Pre-op and post-op images were aligned using 3D rigid registration and then brain shift vectors were determined using a 3D non-rigid registration. An average shift of 1.8 ± 0.8 mm and a maximal shift of 3.9 mm were observed. Since the registration had subvoxel accuracy and the voxel size was about 1 mm, the recorded shift of 1 to 4 mm was unlikely to be significantly influenced by the registration error. Rather, these measurements were consistent with the presence of intraoperative brain deformation. Nevertheless, we cannot rule out that other factors positively or negatively influenced our measurements. For example, the brain may have partly recovered its original shape during the few hours from the end of the surgery to the time of the post-op scan, or post-op imaging itself may have affected the brain movement.

The patient was positioned completely supine in the MRI scanner, while during the surgery the head position was quasi-supine (5-20 deg from supine), which may have caused the shift to be overestimated due to an additional shift. The brain might have moved slightly or deformed after the surgery while the patient was waiting or being transported to the MRI scanner, which might have affected the measured shift. The position of the patient during the surgery, waiting, transportation, and imaging was not measured and recorded, which prevents us from quantitatively analyzing the effect of these positions on the brain shift.

There was a relatively high directional correlation of the four brain shift vectors for each subject, indicating that the diencephalic structures shifted approximately in the same direction. While on average the brain shifted approximately in the gravity direction, the directional correlation between the gravity and the brain shift was not strong since the gravity was just one of the factors affecting the brain deformation.

Although the four shift points moved in approximately the same direction which, on average, was approximately in the gravity direction (Fig. 20a), there was some difference in shift at each point. On average the shift was maximal in the putamen points, followed by AC, with the least shift evident at PC. This decrease in the shift magnitude (as seen in Fig. 17 for a representative subject) may be explained by the fact that the putamina are lateral and anterior to AC which in turn is anterior to PC, and the gravity vector was in the anterior to posterior direction. Thus, the more posterior and deeper structures experienced smaller shift as compared to the anterior and outer structures.

There was no relationship between the length of the surgical procedure or the delay until post-operative imaging and the average shift. A possible explanation for this is that the brain shifts in a fixed time that is independent of the surgery duration, after which it achieves a steady state and it does not deform any more. The same finding was reported for epilepsy patients that underwent subdural electrode grid implantation surgery [21]. A number of factors, including gravity, loss of CSF, pneumocephalus, change in intracranial pressure due to skull opening, and forces due to the insertion of the DBS lead may have affected the brain shift and consequently caused the spread in the scatter plots in Fig. 21.

The largest shift was recorded for a subject with a transventricular DBS lead implant. The penetration of the ventricular system possibly caused larger CSF loss which in turn

may have caused the brain to shift more. A visual inspection suggests that the penetrated lateral ventricle in Fig. 22a partly collapsed and possibly had more CSF loss than the one in Fig. 22b, which might explain why the subject in Fig. 22a experienced larger shift than the subject in Fig. 22b. In addition to these two subjects, there was only one more subject with transventricular DBS lead implantation. Two of the 25 subjects had bilateral pneumocephalus (Figs. 22c and 22d): the degree of shift was above the average in one and below the average shift in the other. Since there were only three patients with transventricular lead insertion, and two patients with bilateral pneumocephalus, we were unable to statistically analyze the relationship between these factors and the amount of shift, but they are unlikely to account for the degree of shift observed in the group as a whole.

We found that brain shift may account in part for DBS lead placement inaccuracy, i.e. failure of the lead to be implanted at the intended stereotactic coordinates. Other factors that can contribute to DBS implantation inaccuracy include mechanical inaccuracy of the stereotactic frame and imaging distortion, which likely also account for the variance in this measurement. In addition to these factors, the measurement error of the shift and dislocation vectors may have contributed to the spread of the data points in Fig. 23. The measurement error of the shift vectors is equal to the error of rigid and non-rigid registration. Given that the registration had subvoxel accuracy and that the largest voxel dimension was 1 mm, the brain shift measurement error was within 1 mm. The measurement error of the dislocation vector is more difficult to estimate since it was affected by several factors including the error of the registration between the stereotactic frame and the pre-op image coordinate system (this registration was provided by the surgical navigation system), the inaccuracy of the stereotactic frame, the distortion and voxel size of the post-op image, the error of diplo-based registration between the pre-op and post-op image, and the error of manual selection of the DBS lead location in the post-op image. Despite the spread of the data point in Fig. 23, there is some correlation between the magnitudes of the shift and dislocation vectors, as well as between their superior-to-inferior components. How might brain shift contribute to lead implantation inaccuracy? Brain shift that occurs prior to or during the mapping procedure is presumably compensated for by

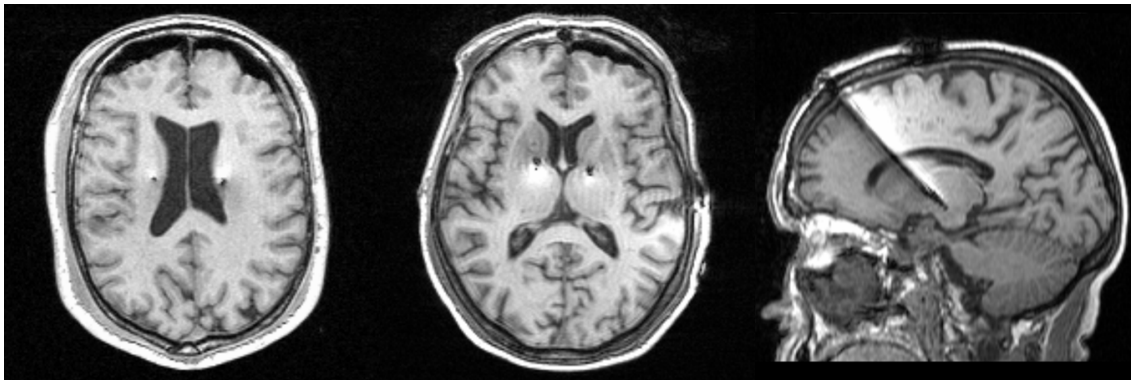

Figure 24. Examples of post-op MRI of subjects with bilateral pneumocephalus (left image - axial view), bilateral pneumocephalus (center image - axial view) and transventricular DBS lead implantation (right image - sagittal view).

MEM which should reasonably well track the shifted tissue. In this case, if no more shift occurs after implantation, DBS placement accuracy would not be affected by the amount of brain shift. Conversely, the number of tracks and/or the amount of mapping-related adjustment of initial targeting would correlate to brain shift, and we did not observe this. On the other hand, brain shift that occurs after the implantation of the DBS electrode would lead to a correlation between degree of brain shift and DBS implantation inaccuracy, as we observed. In this study we could only measure composite shift from pre-operative imaging to post-operative imaging, and therefore we could not determine exactly when or how during the procedure brain shift occurred or how much it contributed to the lead dislocation.

3.3 Study II

3.3.1 Subjects

The brain shift analysis over entire brain was performed using the pre-op and the post-op T1 weighted MR images of the eight patients that underwent DBS surgery. The Fast Field Echo protocol with gradient echo (flip angle = 30°, TR = 25 ms, TE = 4.6 ms) was used to acquire both the pre-op and the post-op scans on a Philips Medical Systems Gyroscan 1.5T MRI scanner. The scans had 200 slices of 256 x 256 pixels with in-plane resolution of 1 mm and slice thickness of 0.9 mm.

Some of the relevant parameters of these eight subjects are listed in Table 4. Two

Table 4. Relevant parameters of 8 DBS surgery subjects. The "DBS lead" column lists the number of DBS leads present in the pre-op and the post-op image. The "side" column means the side of the patient head where stimulator was implanted (R=right, L=left). The midbrain structure in which the deep brain stimulator was implanted is listed under the "target" column. Number of tracks are the listening microelectrode tracks that were used to help determine the location of the target in the midbrain region. "Pneumo" stands for pneumocephalus and "Tv Pen" stands for transventricular penetration. ✓ if a condition is present, × if a condition is absent and ? may be or unsure. Duration is the total duration of the surgery in hours and delay is the time between the end of surgery and the post-op scan in hours. Age is in years, M means male and F means female in sex column.

Subject	DBS Lead		Side	Target	No. of	Pneumo		Tv	Duration	Delay	Age	Sex
No.	pre-op	post-op			Tracks	Left	Right	Pen	[hr]	[hr]	[yr]	
1	0	2	L/R	Vim/Vim	2/3	✓	✓	?	4.6	1.45	63	M
2	0	2	L/R	Vim/Vim	2/6	×	×	?	5.38	2.08	84	F
3	1	2	L	STN	2	×	✓	×	2.45	2.05	55	M
4	1	2	L	STN	7	✓	×	×	5.25	1.5	27	M
5	1	2	L	STN	6	✓	✓	×	2.41	2.18	64	M
6	0	1	R	STN	6	×	×	×	3.45	4.28	43	F
7	0	1	L	STN	6	×	×	?	4.37	1.7	56	F
8	1	2	L	STN	2	×	✓	✓	4.1	5.08	65	F

patients had unilateral implant, two patients had bilateral implant whereas four patients were treated for the second side (as shown in the table under the DBS lead column). Deep brain stimulators were either implanted in Vim or STN. Two patients suffered from bilateral pneumocephalus (left image of Fig. 24) and three patients suffered from unilateral pneumocephalus (center image of Fig. 24) during the surgery. Pneumocephalus is a medical condition due to the presence of air or gas within the cranial cavity. Only one patient had transventricular penetration (right image of Fig. 24) and three showed that the lead in the post-op image was too close to the lateral ventricle but could not be said for certain if it was a transventricular penetration or not. The passing of the DBS lead through lateral ventricles is called transventricular penetration in the DBS surgery.

3.3.2 Results

Second study of brain shift analysis was mainly based on the entire brain and its shift in relation to DBS surgery. Fig. 25 shows checkerboard displays of rigidly and non-rigidly

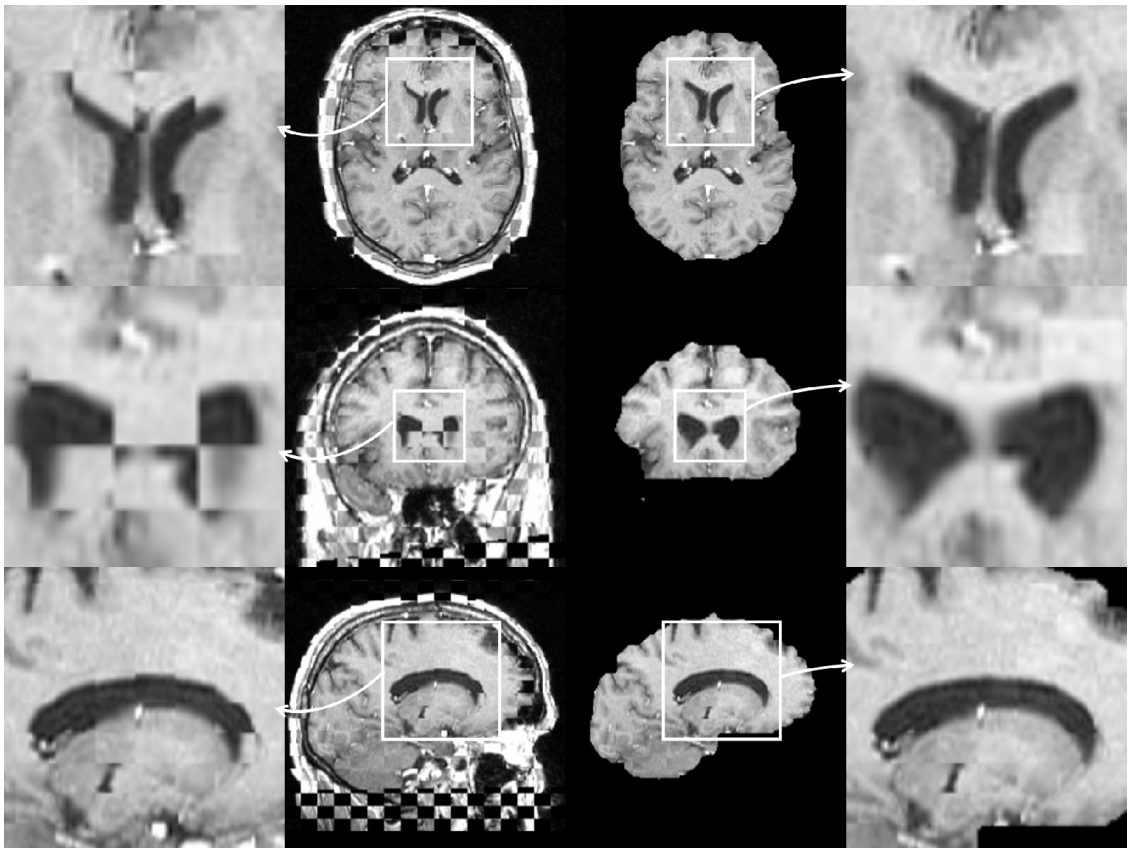

Figure 25. Checkerboard displays of axial (first row), coronal (second row), and sagittal (third row) slices of the pre-op and post-op scans for one of the subjects are shown after rigid (a and b) and non-rigid (c and d) registration. The regions from b and c that are enclosed with white squares are shown enlarged in a and d, respectively.

registered pre-op and post-op scans of one of the subjects. Note the well aligned diploë after the rigid registration (Fig. 25b). A clear misalignment in the lateral ventricles and surrounding structures can be seen after the rigid registration (Fig. 25a), while the non-rigid registration managed to almost perfectly align them (Fig. 25d). The misaligned structures in Fig. 25a show that soft tissues deformed between the two scans. A visual inspection of all the slices of all the subjects over the diploë region for rigid registration and over the brain region for the non-rigid registration revealed no measurable misalignment errors.

Fig. 26 shows the displacement (brain shift) fields overlaid on the pre-op scan for a subject with bilateral pneumocephalus and a subject with unilateral pneumocephalus. Note

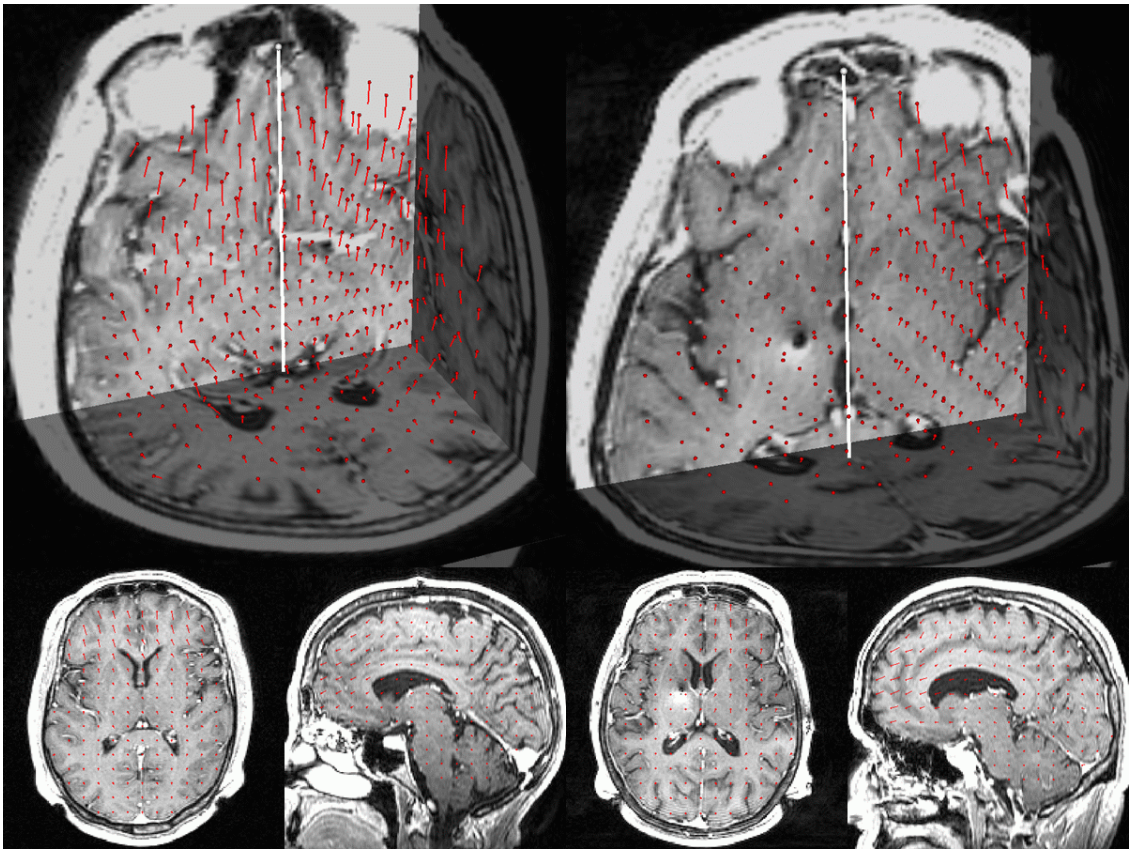

Figure 26. 3D view with three orthogonal slices of the pre-op scan of a subject with bilateral pneumocephalus (top left) and a subject with unilateral pneumocephalus (top right) are overlaid with the respective shift vectors (red). The white vectors show the gravity direction. The spheres represent the bases of the vectors. The bottom row shows the axial and sagittal slices of the respective subject overlaid with the 2D projections of the shift vectors. While the displacement fields are continuous, for visualization purposes they are sampled with a spacing of 12 mm.

that large shift vectors are present on both sides for the subject with bilateral pneumocephalus, whereas, large shift vectors are present only on the side of the pneumocephalus (right side) for the subject with unilateral pneumocephalus.

The shift magnitudes over the brain region for three subjects are shown in Fig. 27. The maximal, mean, and standard deviation of the shift magnitude over the entire brain is given in Table 5 for each subject. The angles of the brain shift vectors having magnitude 1 mm or more are shown in Fig. 28 and all the voxels locations with brain shift vectors of magnitude less than 1 mm are given white color. This is done because the vectors with magnitude of less than 1 mm may not represent the true direction of shift as it is smaller than the voxel size. The head orientation was approximately supine during the DBS surgery for all the

Table 5. For each of the eight subjects listed are the type of the pneumocephalus, maximal, mean, and standard deviation of the shift magnitude over the brain, and the shift magnitude at the left and right implant locations. All the values are in millimeters.

Subject	Pneumocephalus	Max	Mean	Std	Left	Right
1	Bilateral	8.2	1.6	1.4	0.8	1.4
2	-	2.9	0.9	0.4	0.2	1.2
3	Unilateral	4.2	0.8	0.5	0.6	-
4	Unilateral	4.8	0.9	0.6	0.4	-
5	Bilateral	8.3	1.8	1.4	1.6	-
6	-	3.2	1.0	0.5	-	1.0
7	-	3.0	1.0	0.4	0.6	-
8	Unilateral	5.8	1.0	0.8	1.6	-

subjects, i.e. the gravity direction was approximately in the anterior-to-posterior direction. Fig. 29 shows that the shift magnitude dropped from the anterior to the posterior side of the brain for all the subjects.

At each point in B we computed the angle between the shift vector and the gravity direction. Fig. 30 shows the distributions of the angle of the shift vector relative to the gravity direction for the eight subjects. In addition to analyzing the shift over the entire brain, we calculated the shift vectors at the locations of the DBS lead implantation. The magnitudes of these vectors are given in Table 5.

3.3.3 Discussion

The axial, coronal and sagittal checkerboard slices of the pre-op and the registered post-op images of a subject along with their zoomed portions are shown in Fig. 25 after rigid and non-rigid registrations. This figure validates two important points: firstly, the misalignment in the lateral ventricles is due to the brain shift during the surgery as diploë is almost perfectly aligned; and secondly, the non rigid registration algorithm performance is good as almost all the misalignment in the brain structures is recovered by it with visibly no error to measure. This can be clearly seen in the Fig. 25d where the boundaries of the lateral ventricles are almost perfectly aligned as compared to the Fig. 25a after rigid registration.

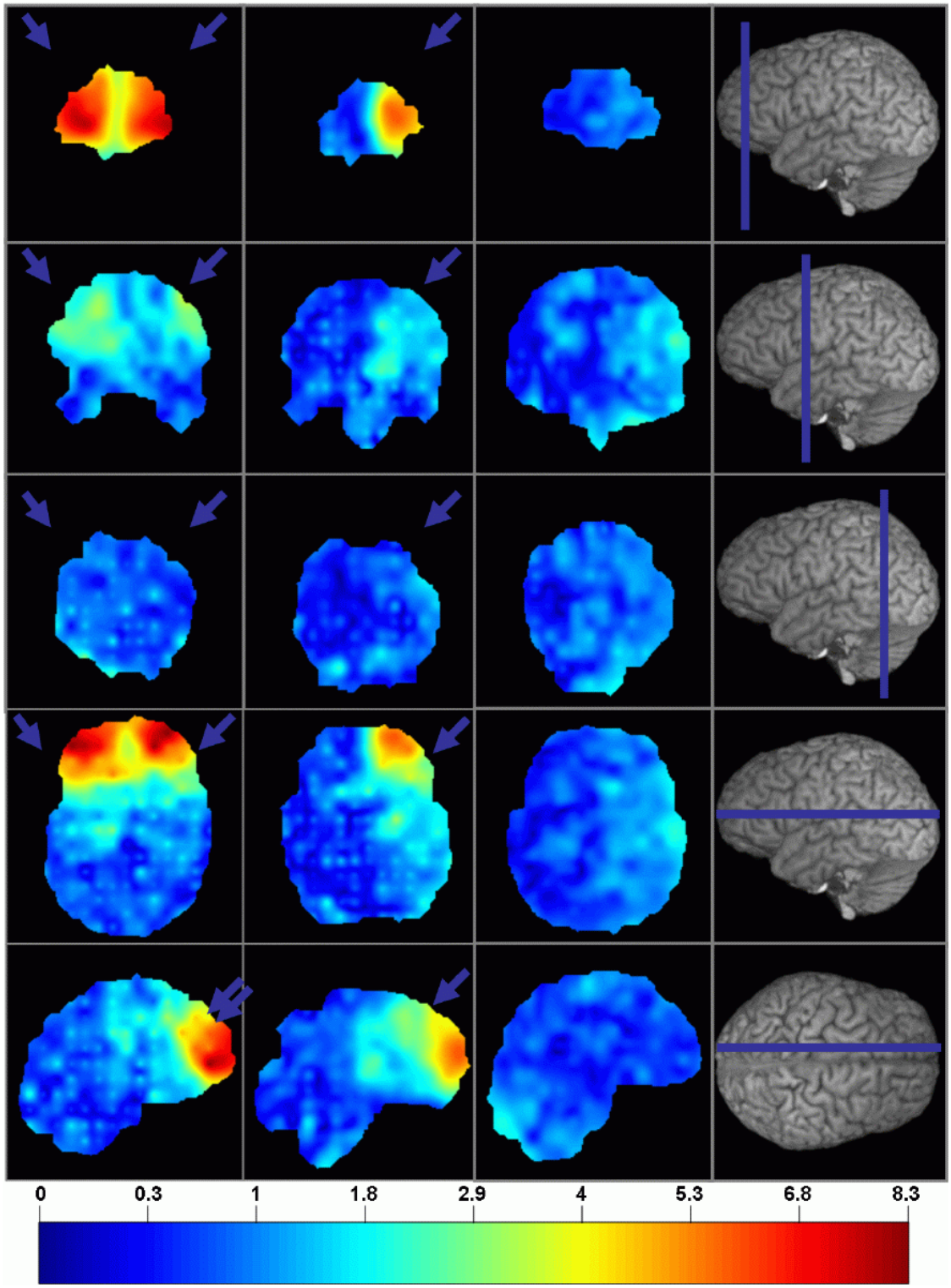

Figure 27. Color-coded shift magnitude [mm] of three subjects with bilateral pneumocephalus (first column), unilateral pneumocephalus (second column), and no pneumocephalus (third column), respectively. The fourth column shows the approximate location of the slice in the brain (blue line). The top three rows are coronal slices at anterior, middle and posterior part of the brain. The fourth row shows axial slices and the fifth row shows sagittal slices. The blue arrows indicate the presence of pneumocephalus.

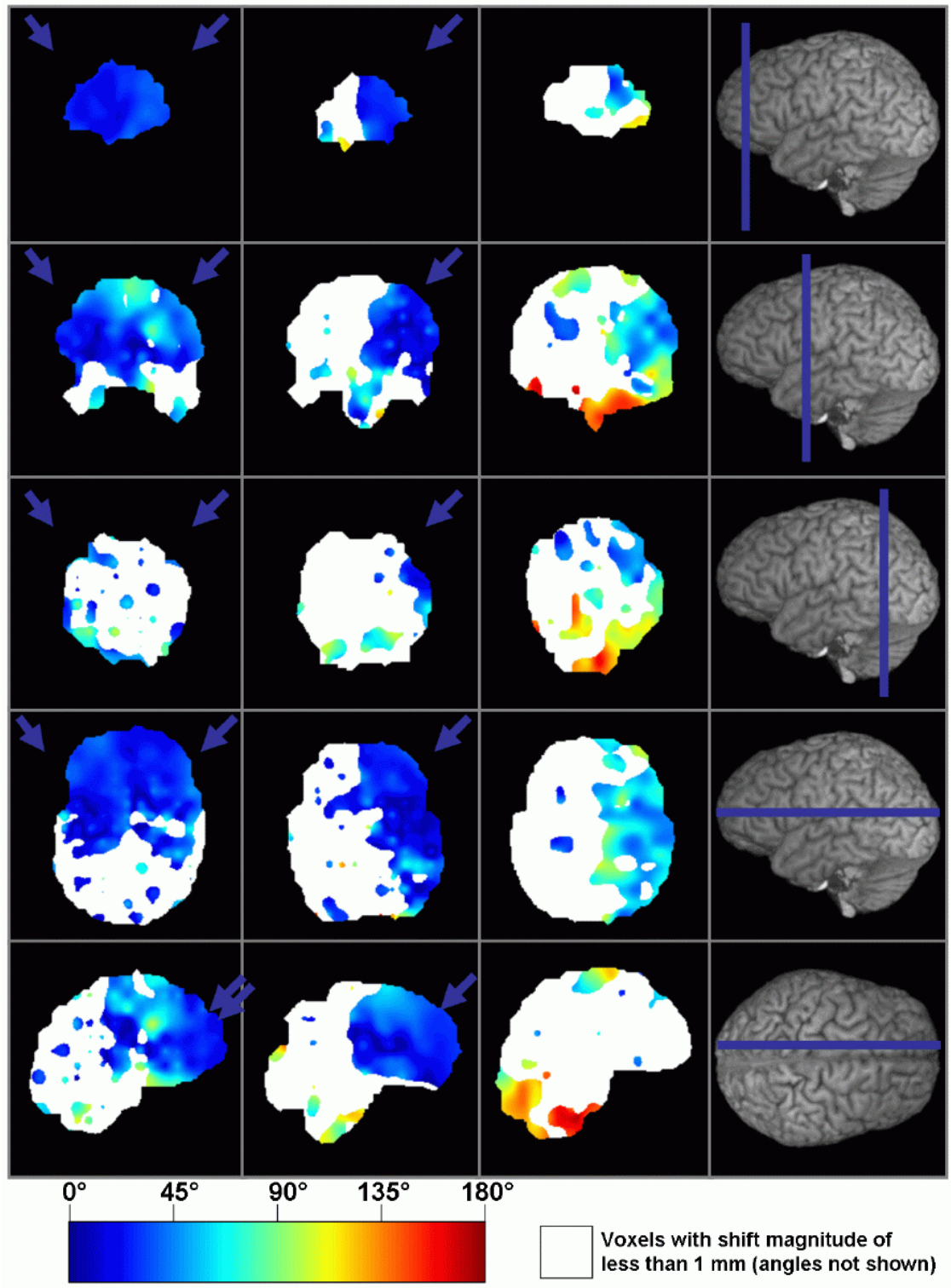

Figure 28. Color coded shift angle images (with the direction of gravity) of three subjects. The type and location of each slice is exactly same as Fig. 27. The darkest shade of blue shows angle of 0° and the darkest shade of red shows angle of 180° with the distribution in between shown by the color bar at the bottom of the image. White color in each image shows the voxel locations with shift magnitude less than 1 mm, which were not used for analysis being smaller than a voxel size.

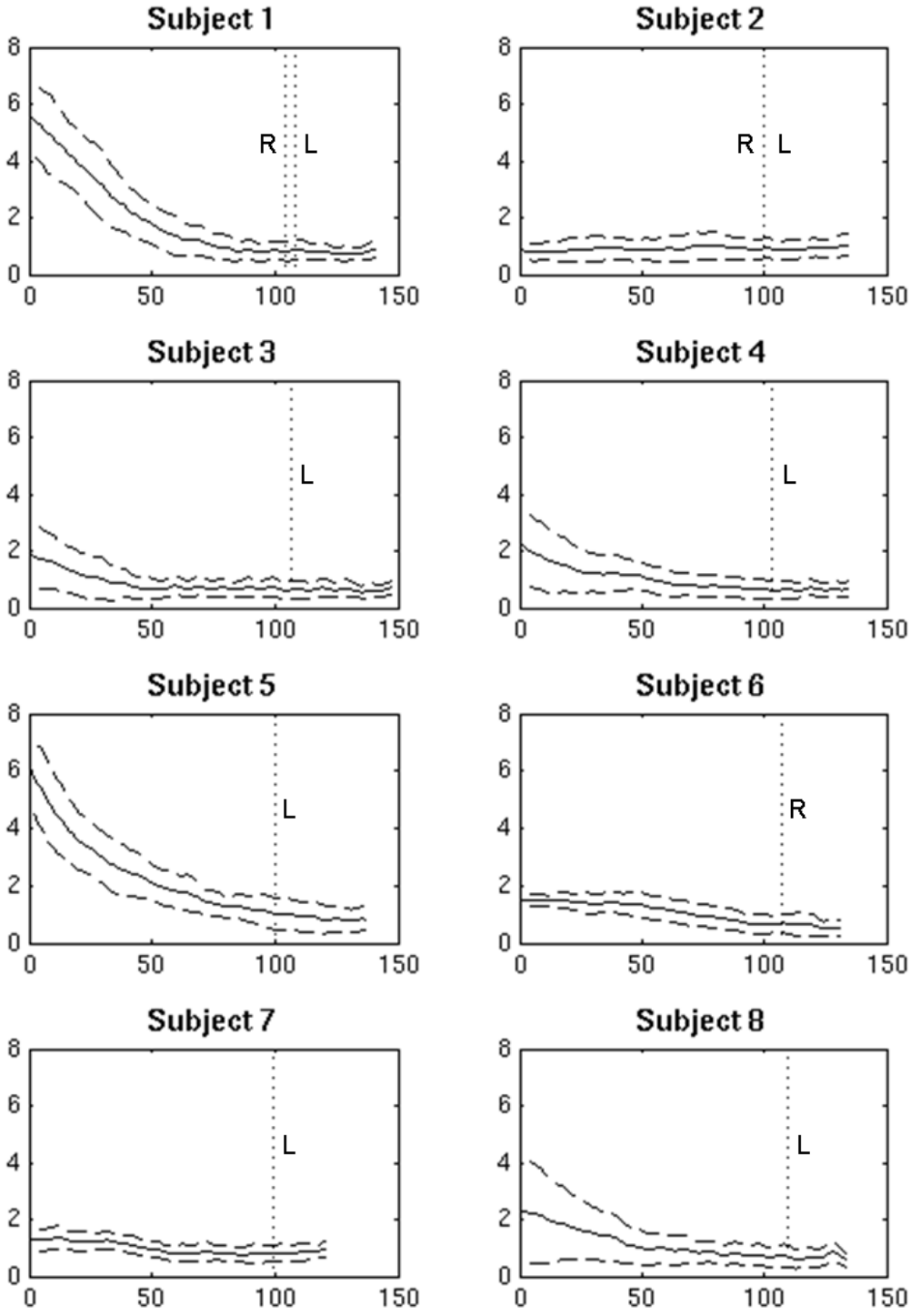

Figure 29. The average brain shift magnitude [mm] in each coronal slice as a function of the slice position in the anterior-to-posterior direction for the eight subjects are shown as solid curves, while the dashed curves are one standard deviation away from the solid curves. The vertical dotted lines denote the slice position of the implant, while the letter denotes the side of the implant (L - left, R - right). Note that subjects 1 and 2 had implants on both sides, while the other subjects had only one implant.

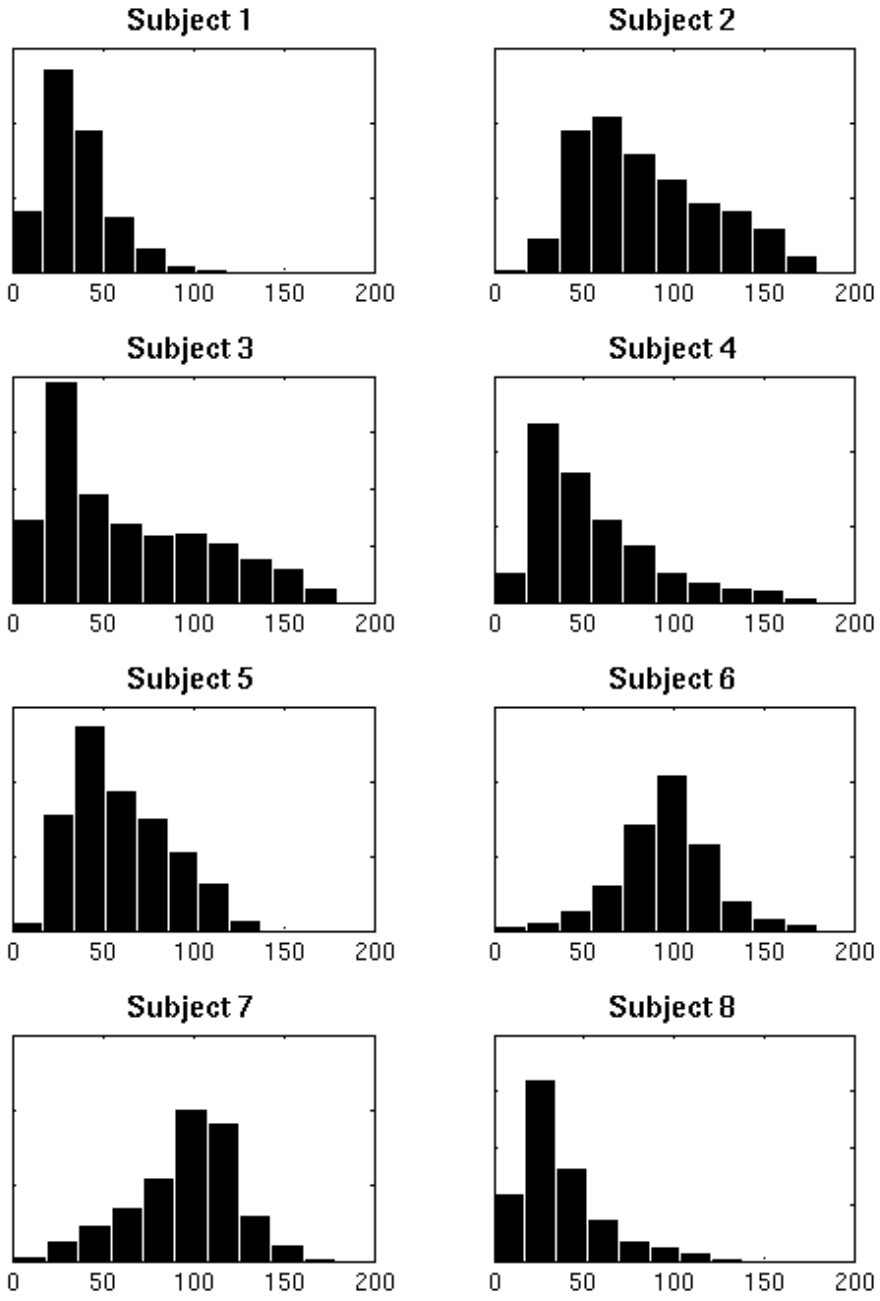

Figure 30. The distributions of the angle of the shift vector relative to the gravity direction computed over the entire brain are shown for the eight subjects. The vectors with shift magnitude of less than 1 mm are not included in the distributions.

Little misalignment or information mismatch in the Fig. 25d is because of the difference in the information between the pre-op and the post-op images in the lateral ventricle areas like presence of DBS lead and electrode in the post-op image which is missing in the preop image. The DBS lead appears as the dark black area in and around the lead and electrodes, whereas, sometimes the brain area outside the DBS lead appear as bright white.

A careful look at the max, mean and std of the magnitude of brain shift vectors over entire brain given in Table 5 in relation to the pneumocephalus column in Table 4 reveals some important relationships. Subjects 1 and 5 had bilateral pneumocephalus and they experienced larger shifts (larger than 8 mm). Subjects 3, 4 and 8 had unilateral pneumocephalus and they experienced medium shifts (4-6 mm), and subjects 2, 6 and 7 had no pneumocephalus and experienced smaller shifts (less than 4 mm). The same observations can be made from Figs. 26, 27, and 29. In Fig. 26 one can see that for the subject with unilateral pneumocephalus the side of the brain without pneumocephalus had much smaller shifts in the anterior region than the side with the pneumocephalus, while for the subject with bilateral pneumocephalus, both sides of the brain had larger shifts in the anterior region. In Fig. 27 it is evident that larger shifts were present at both sides of the anterior region of the brain for the subject with bilateral pneumocephalus and on the side of the pneumocephalus in the anterior region of the brain for the subject with unilateral pneumocephalus, while the subject with no pneumocephalus had smaller shifts everywhere over the brain. Fig. 29 reveals that the subjects with bilateral pneumocephalus (subjects 1 and 5) had larger shifts in the anterior coronal slices than other subjects, and subjects 2, 6, and 7 (without pneumocephalus) had small shifts in all coronal slices.

When the pneumocephalus was present, then the shift magnitude dropped from the anterior to the posterior part of the brain. This is clearly visible for the subject with bilateral pneumocephalus and for the subject with unilateral pneumocephalus on the side of the pneumocephalus in Figs. 26 and 27, as well as for the subjects with pneumocephalus (subjects 1, 3, 4, 5, and 8) in Fig. 29. When the pneumocephalus was not present, the shift was relatively small and approximately equal everywhere over the brain, as visible for the subject with no pneumocephalus in Fig. 27, as well as for subjects with no pneumocephalus (subjects 2, 6 and 7) in Fig. 29. For the subjects with unilateral pneumocephalus, the side

of the brain without pneumocephalus had relatively small shifts over that side of the brain, as visible in Figs. 26 and 27.

One can see from Fig. 26 that the shift vectors were mainly in the gravity direction. Fig. 30 shows that the subjects with bilateral pneumocephalus (subjects 1 and 5) had shifts mainly in the gravity direction, i.e. most of the shift vectors had small angles relative to the gravity direction. The subjects with unilateral pneumocephalus (subjects 3, 4 and 8) had a similar trend with a little more spread out histograms, whereas the subjects with no pneumocephalus (subjects 2, 6 and 7) had even more spread out histograms. The brain shift vectors with larger magnitudes were oriented mostly in the gravity direction, while the brain shift vectors with smaller magnitudes had various orientations. The reason for this may be that the larger shifts were mainly the result of the gravity and pneumocephalus, while smaller shifts were caused by a number of factors. Note that both the gravity and pneumocephalus cause the brain to sag.

The shift at the implant location (columns "left" and "right" in Table 5) was up to 1.6 mm, which was relatively small compared to the maximal shift over the entire brain. From Fig. 29 one can see that the shifts at the implant locations (marked by vertical dotted lines) were relatively small and even in the subjects with pneumocephalus the shifts dropped significantly from the anterior part of the brain to the implant location. However, the shift at the implant locations was non-negligible for implantation of the DBS lead in STN (which is approximately 4 x 6 mm in the axial plane), GPi (which has a maximal diameter of approximately 8 mm), or thalamus (which in the Vim/Vop target area measures approximately 2 x 3 x 6 mm).

CHAPTER 4

AN INTEGRATED ELECTROPHYSIOLOGICAL AND ANATOMICAL MRI ATLAS FOR IMAGE GUIDED DEEP BRAIN STIMULATION SURGERY

DBS surgery is an effective treatment for the patients of movement disorders that can no longer be treated by medications [1, 2, 3, 4, 5]. An electrode lead is permanently implanted in a deep brain structure, used as target, to deliver continuous high-frequency electrical stimulation in the DBS surgery [9, 10, 16]. Deep brain structures are the anatomical structures in and around midbrain and ventricular regions [34]. The small size and surrounding neuronal structures make it difficult to identify most of the deep brain structures in the common imaging modalities like MRI or CT. Typical DBS targets are STN (approximately 4x6 mm in the axial plane), GPi (radius of approximately 4 mm) and ventral intermediate nucleus (Vim) of the thalamus (approximately 2x3x6 mm). This chapter describes an atlas based method for improving the DBS implantation accuracy over the currently used procedure.

4.1 Materials and Methods

4.1.1 MRI Protocols and Subjects

One atlas image and twenty subject T1 weighted 3D MR images, pre-op and post-operative (post-op), that underwent DBS surgery were used in this study. The atlas image was acquired using 3D Turbo Flash MRI protocol at a 3T MRI scanner with repetition time (TR) of 2300 ms and echo time (TE) of 3.9 ms. The MRI scan had 192 slices of 256 x 256 pixels with isotropic voxels of 1 mm^3. The acquisition time for the atlas image was 30 minutes which resulted in higher signal to noise (SNR) ratio. Higher SNR values helped distinguish the deep brain structures from their surroundings.

The pre-op and the post-op subject images were acquired using the Fast Field Echo protocol with gradient echo (flip angle = 30°, TR = 25 ms, TE = 4.6 ms) on a Philips Medical Systems Gyroscan 1.5T MRI scanner. The pre-op MRI scans had around 200 slices of 256x256 pixels with in-plane resolution of 1 mm and slice thickness of around 0.9 mm. Thirteen post-op MRI scans had 120 slices and seven post-op MRI scans had 150-200 slices

of 256x256 pixels with in-plane resolution of 1 mm and slice thickness of 0.8 mm.

4.1.2 Surgical Procedure

The current surgical procedure followed at the Emory University starts with a fitting of a stereotactic frame (CRW*fn* , Radionics, Burlington, Mass., USA) on the subject's head on the day of surgery and volumetric T1 weighted images are obtained in the axial plane as described in Section 4.1.1. In the operating room, planning is performed for initial target localization on the Stealth® workstation (Medtronic, Littlefield, Colo., USA) using indirect targeting based on the anterior and posterior commissures and, for Vim, the wall of the third ventricle. In most cases the entry point is selected to avoid penetration of the lateral ventricle. Accuracy is checked on the phantom base. Under local anesthesia, unilateral or bilateral burr hole craniotomy and dural opening is performed. Target refinement is performed using microelectrode mapping with a Guideline System 3000® micropositioner and microelectrode recording system (Axon Instruments, Frederick Haer, Inc., Bowdoinham, Me., USA). During microelectrode mapping (MEM) proprietary software developed at Emory University is used to monitor the advancement of the microelectrode and track locations relative to anatomical targets. After a case-dependent number of tracks, the final target selection is made based on neurophysiological and clinical criteria [85] and a DBS electrode array (Model 3389 or 3387, Medtronic, Minn., USA) is inserted through a guide tube. After clinical testing (Medtronic screener Model 3625) the DBS electrode is affixed to a burr hole anchoring assembly (IGN Medtronic, Melbourne, Fla., USA). Following the procedure patients routinely undergo post-operative MRI as described in Section 4.1.1.

4.1.3 Atlas Construction

The atlas image is a high SNR MRI head scan of a healthy volunteer as explained in Section 4.1.1. The following eleven deep brain structures were manually segmented by a trained expert: Striatum (Str) includes caudate nucleus (CN), putamen (Pu) and some internal capsule; Globus Pallidus External (GPe); Globus Pallidus Internal (GPi); Optic Tract (OT); Anterior Commissure (AC); Posterior Commissure (PC); Reticular Nucleus of the Thalamus (Ret); Thalamus (Th); Subthalamic Nucleus (STN); Zona Incerta (ZI); and Substantia Nigra Reticularis (SN). In addition, left ventricle (LV), right ventricle (RV)

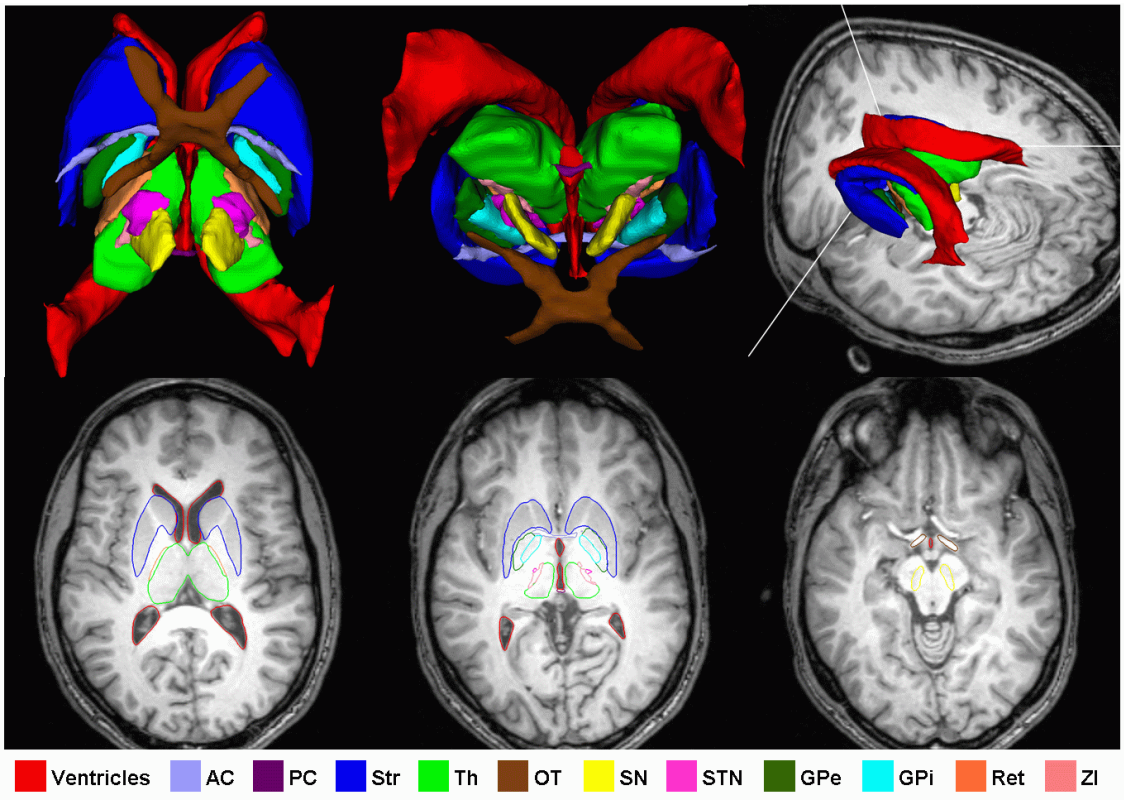

Figure 31. Manually segmented deep brain structures shown as 3D models (top row) and 2D contours (bottom row). Zoomed inferior view (top left image) and posterior view (top center image) of the 3D models of segmented deep brain structures in the atlas MR image. Segmented 3D models in 3D view (top right image) seen from superior-posterior side of the head. Bottom row shows three 2D axial slices along with the contours of the segmented deep brain structures. The abbreviations in the color coding at the bottom are defined in Section 4.1.3.

and third ventricle (V3) were also manually segmented. The segmentation maps of each segmented structure were used to generate the 3D models using marching cubes algorithm [86]. The surfaces of these structures are then smoothed using curve and surface smoothing without shrinkage [87]. Fig. 31 shows the manually segmented deep brain structures in the atlas MR image.

4.1.4 Registration

The image registration between the atlas and the subject image is performed in two stages.

4.1.4.1 Stage - 1

The Stage-1 is initialized by affinely registering the subject image to the atlas image. Approximately uniformly spaced nodes (with a spacing of 5 mm) are placed over the LV, RV

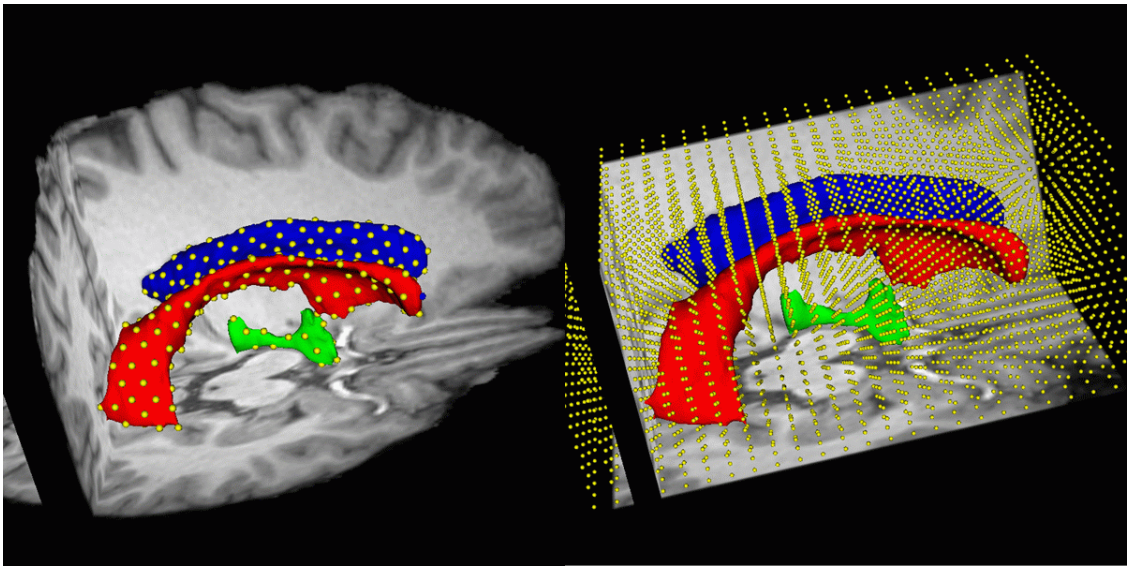

Figure 32. Positioning of the nodes in the 3D view of the atlas image during Stage-1 (left image) and Stage-2 (right image) of registration. The brain region shown in each image is considered for computation of image similarity measure. The RV is shown in red, LV in blue and V3 in green.

and V3 of the atlas (as shown in Fig. 32, left image) and the corresponding nodes in the subject images are placed using the initial affine transformation. The two sets of nodes are used to define non-rigid transformation using thin plate splines (TPS) between the atlas and the subject image [83]. The nodes are optimized using the Powell's method [84] to maximize normalized cross correlation (NCC) over the segmented brain in the atlas image. Let I be the atlas image, J be the subject image and X be the brain region in the atlas. The optimization process is given by

$$\mathbf{T_{TPS}} = \arg\max_{\mathbf{T_{TPS}}} NCC(I(X), J(\mathbf{T_{TPS}}(X))), \tag{4.1}$$

where $\mathbf{T_{TPS}}$ is the TPS transformation from the atlas image to the subject image. The NCC between image I and J with N number of voxels in the area of overlap X is given by

$$NCC(I,J) = \frac{1}{N^2} \frac{\sum_{x \epsilon X} (i(x) - \bar{i})(j(x) - \bar{j})}{\sigma_i \sigma_j}, \tag{4.2}$$

where $\bar{i}$ and $\bar{j}$ are the mean intensities of $I(X)$ and $J(X)$, $i(x)$ and $j(x)$ are the voxel intensity values at voxel location $x \epsilon X$ of $I(X)$ and $J(X)$, and

$$\sigma_i = \frac{1}{N}\sqrt{\sum_{x\epsilon X}(i(x)-\bar{i})^2},$$

$$\sigma_j = \frac{1}{N}\sqrt{\sum_{x\epsilon X}(j(x)-\bar{j})^2}.$$

4.1.4.2 Stage - 2

The Stage-2 uses NCC as the similarity measure, Cubic-B splines (CBS) to represent the non-rigid transformation and the Powell's method for optimization over the deep brain region (Fig. 32, right image). The deep brain region is defined by adding ±20 mm to the minimum and maximum extent of LV, RV, and V3, as shown in the right image of Fig. 32. A uniformly spaced grid of nodes with a spacing of 5 mm over the deep brain region is placed on the atlas image. The final TPS transformation of Stage-1 is used to initialize the CBS transformation. A smoothness term is introduced to regularize the transformation. The total energy function (E_{total}) to be maximized is

$$E_{total} = E_{similarity} - \lambda E_{smooth}, \tag{4.3}$$

where

$$E_{similarity} = NCC(I(D), J(\mathbf{T}(D))),$$

$$E_{smooth}=\frac{1}{V_D}\iiint_D \left[\left|\frac{\partial^2\mathbf{T}}{\partial x^2}\right|^2 + \left|\frac{\partial^2\mathbf{T}}{\partial y^2}\right|^2 + \left|\frac{\partial^2\mathbf{T}}{\partial z^2}\right|^2 + 2\left|\frac{\partial^2\mathbf{T}}{\partial x\partial y}\right|^2 + 2\left|\frac{\partial^2\mathbf{T}}{\partial x\partial z}\right|^2 + 2\left|\frac{\partial^2\mathbf{T}}{\partial y\partial z}\right|^2 \right] dv,$$

and $\mathbf{T}$ is the CBS transformation from the atlas image to the subject image, D is the deep brain region and V_D is its volume. λ is used to control the amount of deformation allowed and we use the value of 0.5 for all the subjects.

4.1.5 Segmentation

The final transformation of the Stage-2 is used to map the segmented deep brain structures from the atlas image to the subject image. This provides the eleven segmented structures in each subject whose boundaries are not visible in the images.

4.1.6 Validation

We manually segmented LV, RV, left Pu (PL), right Pu (PR), left CN (CL) and right CN (CR) in 2D slices and considered them to be the ground truth for the evaluation and validation of the automatic segmentation results of these structures. The reason for selecting these structures is that they are the only deep brain structures whose boundaries could be seen with reasonable confidence in all the 20 subjects. The automatic segmentation results were compared against the manual segmentation using true positive (TP), false positive (FP) and false negative (FN) measures. An automatically segmented voxel of a structure is considered to be a TP if that voxel is also present in the manual segmentation map of that structure and a FP if that voxel is not present in the manual segmentation map of that structure. An automatically segmented voxel is considered a FN if that voxel is not detected by the automatic segmentation whereas the same voxel is present in the manual segmentation map. Using the number of TP and FN we calculated sensitivity (S) which measures the ability to detect the automatically segmented structure when the structure is present as per the manual segmentation map. We also measured positive predictive value (PPV) which is the proportion of positives that correspond to the presence of the voxel in the manual segmentation map. Sensitivity and PPV are given by:

$$S = \frac{TP_n}{TP_n + FN_n}, \tag{4.4}$$

$$PPV = \frac{TP_n}{TP_n + FP_n}, \tag{4.5}$$

where TP_n, FP_n and FN_n are the number of true positives, false positives and false negatives respectively.

We also computed the Dice coefficient(D) [81], as given by Equation (2.8), between the automated and manual segmentation for six seep brain structures (LV, RV, PL, PR, CL and CR).

We also computed the mean boundary distance (MBD) between the manually segmented structures and the automatically segmented structures. The MBD is defined as the mean of the minimum distance between the boundary voxel of one structure to the boundary voxels

of the other structure. Let M be the manually segmented voxels and A be the automatically segmented voxels with $m \subset M$ and $a \subset A$ be the boundary voxels of each structure. The MBD is given by:

$$MBD = \frac{1}{N_a} \sum_{a_i \epsilon a} \min |a_i - m|, \tag{4.6}$$

where N_a is the total number of automatically segmented boundary voxels.

4.1.7 Electrophysiological Atlas and Target Localization

The final implant location of the DBS electrodes were manually recorded in the 20 post-op patient MR images. The tip of the electrode lead was recorded. These recorded final implant locations are taken to their respective pre-op images using the pre-op to post-op non-rigid registration as explained in [19, 33]. From the pre-op images, these final implant locations are than collected in the atlas image using the registration results of section 4.1.4. This gives us four clusters, one each for left STN, right STN, left GPi and right GPi. The Vim implant points were not used as there were only 3 available for both left and right Vim, which are too less for any analysis. These four clusters gave us an electrophysiological MR atlas that also has the deep brain structures segmented in it. The cluster centroids using leave one out method were transformed to the subject images to compare our automated initial target selection method as opposed to the currently followed manual target selection by a trained expert (as explained in 4.1.2). These cluster centroids may be used to predict the initial implant location for the future DBS surgeries.

4.2 Results

The manually segmented deep brain structures in the atlas MR image are shown in Fig. 31. All the deep brain structures are within or around the LV, RV and V3 regions. If the alignment of the LV, RV and V3 is good the surrounding structures will also be well aligned, even if their boundaries are not visible.

4.2.1 Registration

There is no ground truth to compare our registration results against. We qualitatively assessed the registration results by using the checkerboard display of the atlas and the

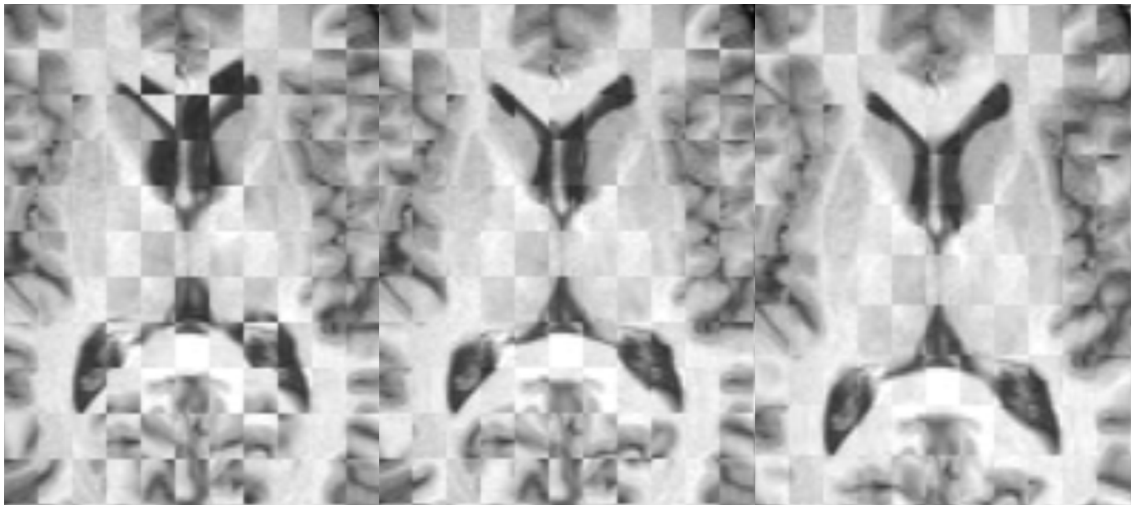

Figure 33. Axial checkerboard slices of the atlas image and a registered subject image after affine initialization (left), Stage-1 (center) and Stage-2 of registration. Note the improvement in the alignment of the ventricles, PU and CN after each stage.

registered subject images (Fig. 33). Fig. 33 shows the axial checkerboard slices of the atlas image and one of the subjects MR image registered to atlas after affine initialization (left most image of Fig. 33), Stage-1 (left most image of Fig. 33) and Stage-2 (right most image of Fig. 33). Clear misalignment can be seen in the ventricles and brain tissue around it in the deep brain region after the initialization. The alignment of the ventricles is improved after Stage-1 but the tissues around ventricles are still misaligned. The checkerboard slice after Stage-2 shows good alignment of the ventricles and the tissues around them. Fig. 34 shows the axial, coronal and sagittal checkerboard slices of the atlas and a registered subject image after final registration of Stage-2 along with the contours of segmented LV, RV and Str in the atlas image. The boundaries of the registered visible structures (LV, RV, Pu and CN) show good alignment with the segmented contours of the atlas.

We also averaged the 20 subject images registered to atlas after initialization, Stage-1 and Stage-2 respectively, as shown in Fig. 35. The average image is obtained by summing up the intensities of the 20 registered subject images and dividing it by the number of subjects, which is 20 in this case. It can be seen in Fig. 35 that the average image after initialization is very hazy (Fig. 35b). The average image after Stage-1 (Fig. 35c) shows clear ventricles but brain around ventricles is still hazy. This is due to the fact that Stage-1

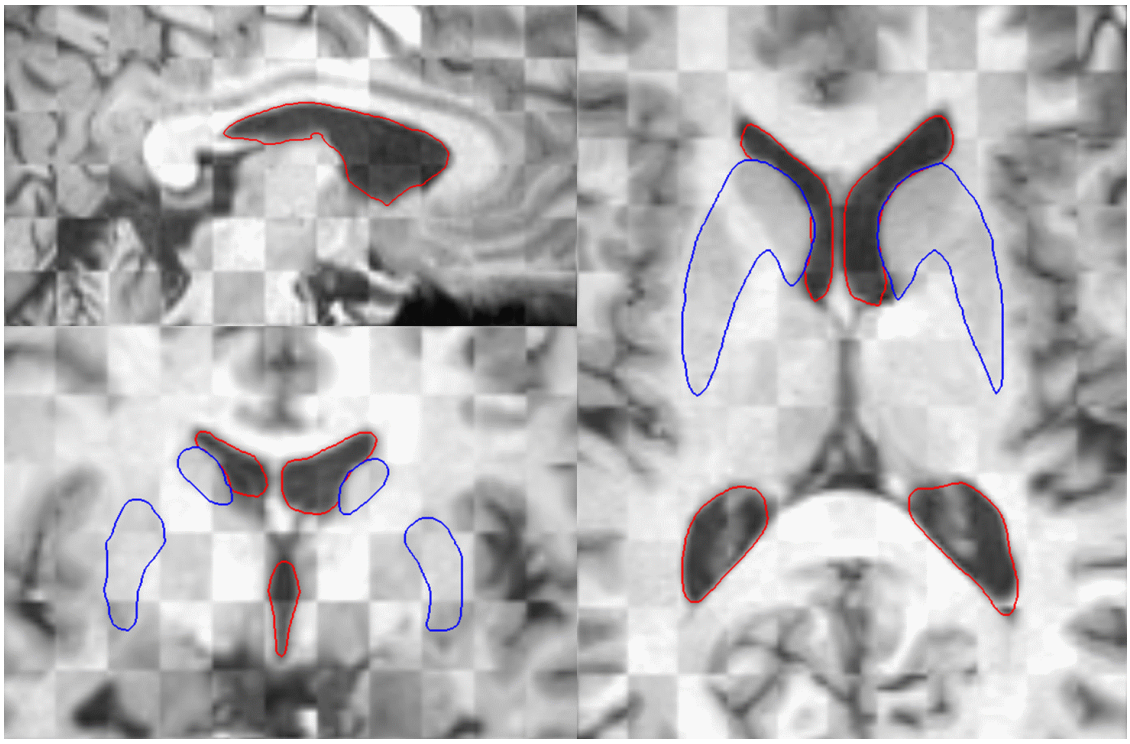

Figure 34. Axial (right), sagittal (top left) and coronal (bottom left) checkerboard slices of the atlas image and a non-rigidly registered subject image along with the contours of Str, LV and RV. Note the alignment of the ventricles, Pu and CN. The color coding is same as in Fig.31.

of registration focuses on the alignment of the ventricles only. The average image after Stage-2 (Fig. 35d) shows good and clear structures around ventricles as well.

4.2.2 Segmentation

Fig. 36 shows the contours of the segmented deep brain structures in axial slices of the atlas MR image (left column). The boundaries of LV, RV, V3, Pu, and CN are clearly visible due to the intensity differences between the structures and the tissues around them (Fig. 36). The right column of Fig. 36 shows axial slices of a registered subject image together with the contours of the segmented atlas structures. It can be seen that the contours of the ventricles, PU and CN mapped from the atlas are well aligned with the boundaries of the actual subject structures. Since the visible structures (ventricles, Pu, CN) are well aligned, the deep brain structures that are not clearly visible in the subject images (AC, PC, GPe, GPi, Ret, ZI, OT, Th, STN, and SN) are likely reasonably well aligned to the actual subject structures.

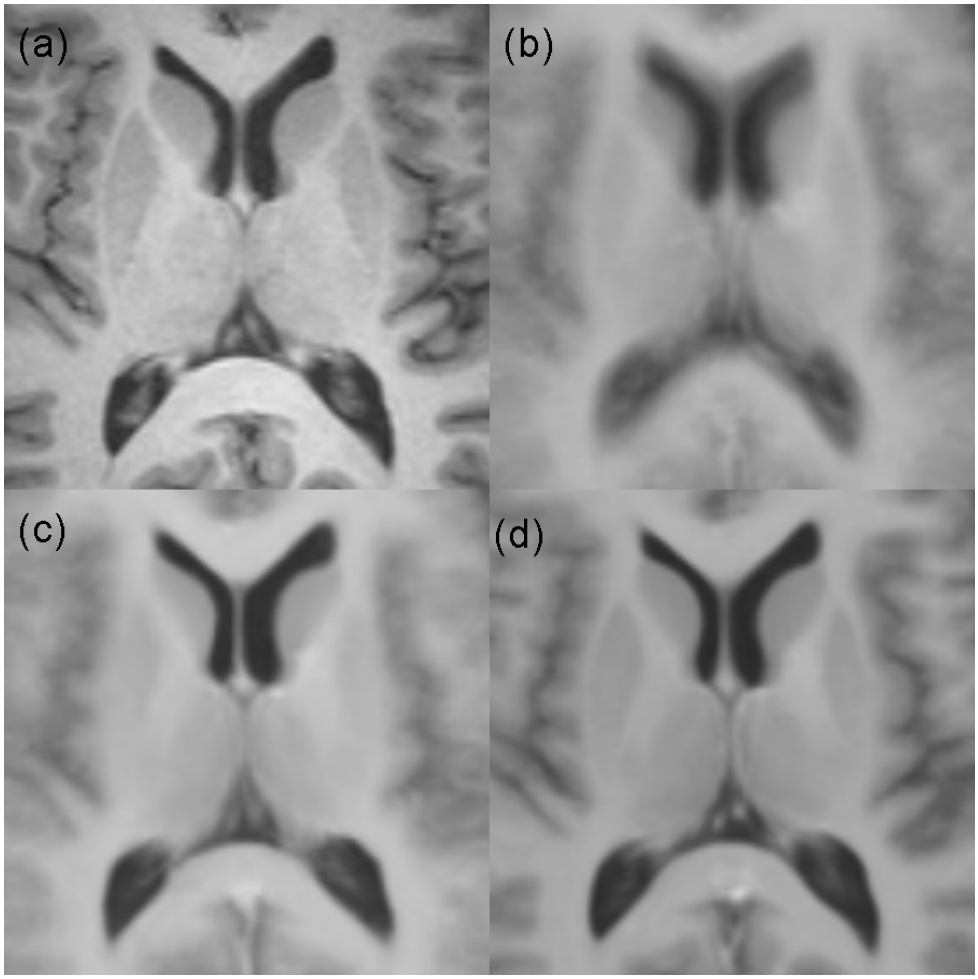

Figure 35. Deep brain region axial slice of the atlas image (a) and the corresponding slices of the average of 20 subject images registered to atlas image after affine initialization (b), Stage-1 of registration (c) and Stage-2 of registration (d).

4.2.3 Validation

The box plot of the sensitivity is shown in Fig. 37, of PPV in Fig. 38, of Dice coefficient in Fig. 39 and of MBD in Fig. 40 for the six deep brain structures (PL, PR, CL, CR, LV and RV) that were segmented automatically and manually for 20 subjects. The box plots show the spread of the values and the quartiles. Most of the values are around 0.9 for sensitivity, PPV and Dice coefficient, and the values of MBD are around 0.5 mm. The $mean \pm std$ of the sensitivity is 0.89 ± 0.013, of PPV is 0.93 ± 0.013, of Dice coefficient is 0.91 ± 0.03 and of MBD is 0.55 ± 0.18 mm over six structures. These values of means and standard deviations show that automatic segmentation of the structures by our method is acceptably close to

the manual segmentation. The tables in Appendix C show the detailed values of TP, FP, FN, S, PVP, D and MBD for the six deep brain structures (PL, PR, CL, CR, LV and RV) over 20 DBS surgery patients.

4.2.4 Electrophysiological Atlas and Target Prediction

Electrophysiological atlas was constructed by gathering the final implant locations of the 20 DBS subjects on to the atlas image. This resulted as four clusters of electrophysiological data points, one each for left STN, right STN, left GPi and right GPi as shown in Fig. 41. Most of the STN points and their centroids fall inside the structure (top row of Fig. 41). The GPi points cluster just outside the inferior-posterior edge of the GPi. This may be due to the fact that the recorded location is the tip of the array of electrodes (four in this case), thus if the tip is just outside the structure, the electrodes will be inside the structure. We also calculated the distance of each point of the cluster from its respective centroid. The mean, std, min and max of these distances for each cluster are shown in Table 6. The mean $\pm$ std of the distance form the centroid for STN clusters is 2.1 ± 1.4 mm and GPi clusters is around 3.5 ± 2.6 mm that shows the tightness of clusters.

We had the implant locations of the initial target recorded by the expert for 13 implants out of 20 subjects. Table 7 shows the distance between the automatic selection and the actual implant location, the distance between the manual selection and the actual implant location, and the distance between the manual and automatic selection points. Positive values of "auto-manual" in Table 7 means that the automatic selection is closer to the actual implant location and negative values mean otherwise. The results show that automatic selection of target is 85% of the times closer to the final implant location as opposed to the manual selection of points. The automatic selection method brings the predicted target point 1 mm on average closer to the actual implant location than the manual target selection.

Fig. 42 shows a zoomed axial and sagittal slice of a subject along with the segmented STN contour and the final implant location (blue point), automatically selected implant location (red point) and the manually selected implant location (yellow point). It is clearly visible that the automatically selected implant location is closer to the final implant location, whereas, manually selected implant location is 3-4 mm off from the final implant location.

Table 6. The mean, std, min and max of the distance from the cluster centroid to each point of the cluster for left STN, right STN, left GPi and right GPi (in mm).

Structure	Mean	Std	Min	Max	No of Points
Left STN	2.05	1.26	0.77	3.77	4
Right STN	2.15	1.54	0.44	5.35	8
Left GPi	3.63	2.64	1.26	7.06	4
Right GPi	3.45	2.58	1.44	7.74	5

Table 7. Comparison of automatic vs manual prediction error of initial target location (in mm).

Point	**Structure**	**Side**	**Manual**	**Auto**	**Manual-Auto**	**Better**
P_1	STN	L	4.06	2.35	1.71	Auto
P_2	STN	R	2.05	0.46	1.59	Auto
P_3	STN	L	3.4	4.62	-1.22	Manual
P_4	STN	L	4.34	0.93	3.41	Auto
P_5	STN	L	3.37	2.69	0.68	Auto
P_6	STN	R	2.06	4.45	-2.39	Manual
P_7	STN	R	1.62	1.58	0.04	Auto
P_8	STN	R	3.66	2.83	0.83	Auto
P_9	GPi	R	7.18	1.9	5.28	Auto
P_{10}	GPi	L	10.52	8.52	2	Auto
P_{11}	GPi	L	6.95	5.47	1.48	Auto
P_{12}	GPi	R	3.61	2.13	1.48	Auto
P_{13}	GPi	R	11.05	10.33	0.72	Auto
Mean	-	-	**3.85(4.91)**	**2.67(3.71)**	**1.17(1.20)**	-
Std	-	-	**1.81(3.09)**	**1.51(2.94)**	**2.06(1.90)**	-

4.3 Discussion

The currently used atlas based segmentation or localization approaches, as explained in section 1.3, have some caveats. The problem with the use of anatomical atlases is their digitization. The digitization of the atlases is not a trivial task since the inter slice difference is not uniform, which needs interpolation and reslicing to make it a uniformly spaced 3-D volume. Than registration of these anatomical atlases with the patient's MR image requires either manual marking of control points in the atlas and pre-op image to guide the non-rigid registration or segmentation of structures like cortex and ventricles in the atlas and the pre-op MR image. Manual marking of control points is a laborious job since 200-400 control points are required to reasonably match the patient image with the atlas. The segmentation of brain structures in the atlas and the patient images may introduce errors due to imperfect segmentation and an added step in between. [40] and [41] have used this approach by digitizing the Talairach-Tournoux atlas and non-rigidly registering the atlas with the subject MR images. To guide the non-rigid registration step, they segment cortex and ventricles in the Patient MR images.

The manual segmentation of the deep brain structures or segmentation through registration with anatomical atlases gives a MR atlas image with segmented structures. It gives a good estimation of the structures boundaries once registered to a subject image but the exact target location within the structure is not identified. The preparation of electrophysiological atlases and their subsequent use for target localization is a good approach but they do not give the deep brain structure boundaries which are helpful during the microelectrode mapping. Our approach gives both, the boundaries of the segmented deep brain structures as well as the electrophysiological data of the target locations (for STN and GPi).

The exact location of the placement of DBS electrode within a target structure is not known, which is decided by the surgeon based on neurophysiological and clinical criteria. Fig. 41 shows the clustering of the final implant points of 20 subjects brought on to the atlas image. The STN clusters show that the final implant location selected by the surgeon based on neurophysiological and clinical criteria is the anterior part of the STN. Whereas, the final implant locations of the GPi in Fig. 41 show that the selected location is just

outside the inferior-posterior part of the GPi. This location does not mean that the DBS electrodes were implanted outside the GPi, rather the recorded point is the tip of the electrode lead, therefore the electrodes must have be within the GPi. Fig. 42 shows that the initial estimate of target location was within the STN but the final implant location was selected somewhere else in the STN based on neurophysiological and clinical criteria. This suggests that segmented structures boundaries may not be enough for accurate target localization without the availability of the electrophysiological target data available in the atlas MR image.

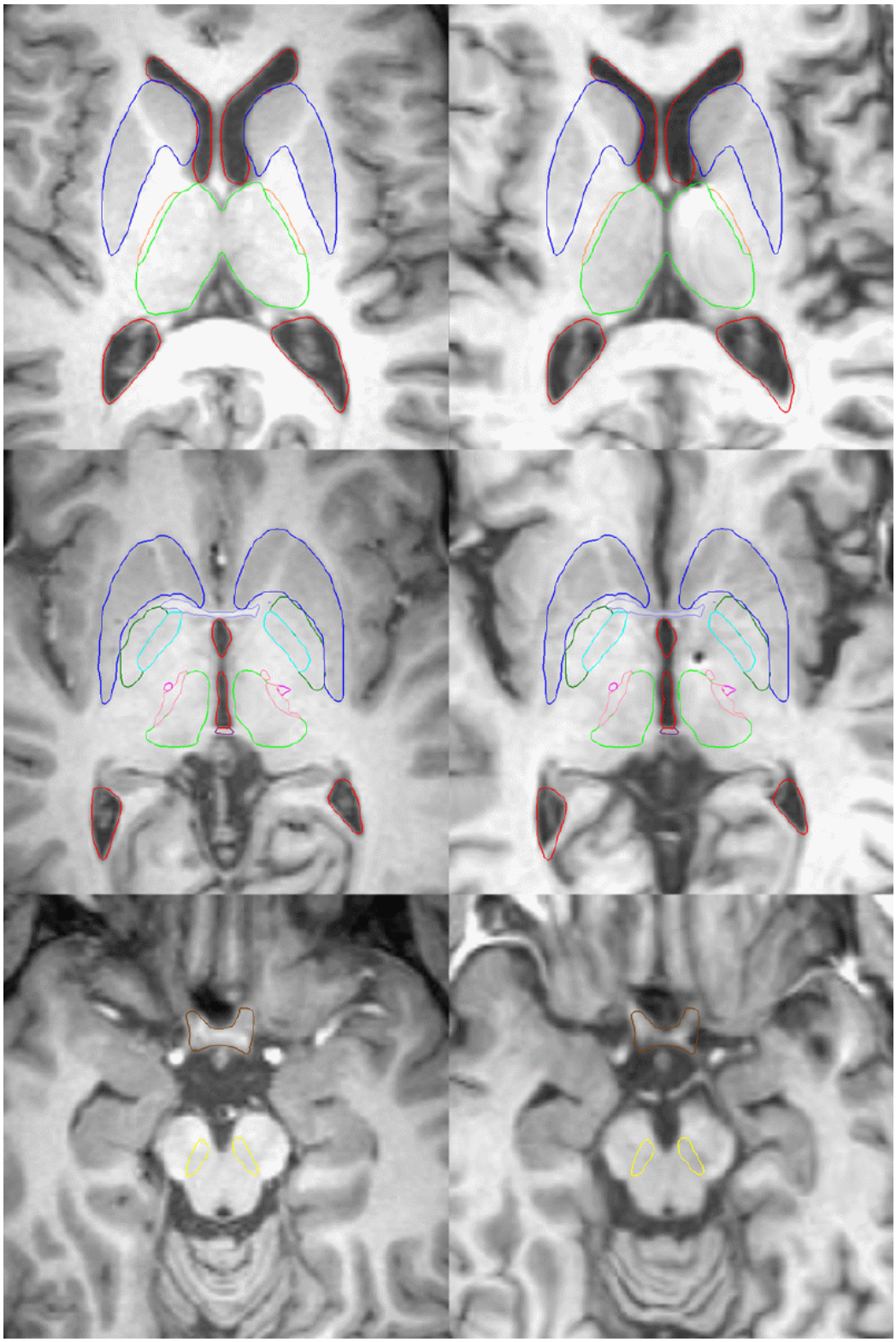

Figure 36. Deep brain region axial slices of the atlas image (left column) and a registered subject (right column) are overlaid with the contours of the segmented structures. The color coding is the same as in Fig. 31. Note the alignment of the ventricles, PU and CN, which are visible.

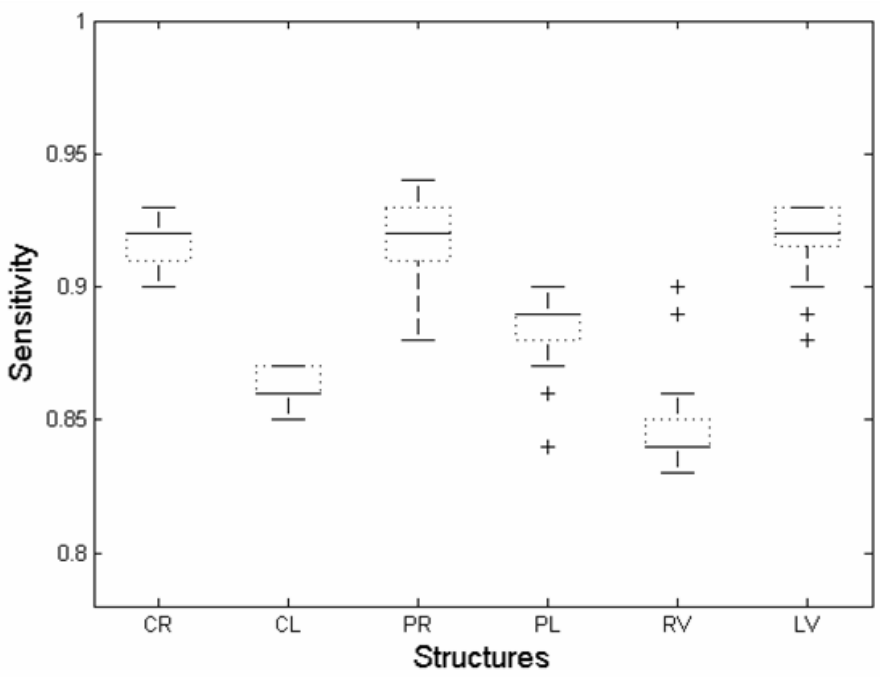

Figure 37. The box plot of the sensitivity of the six structures (CR, CL, PR, PL, RV and LV).

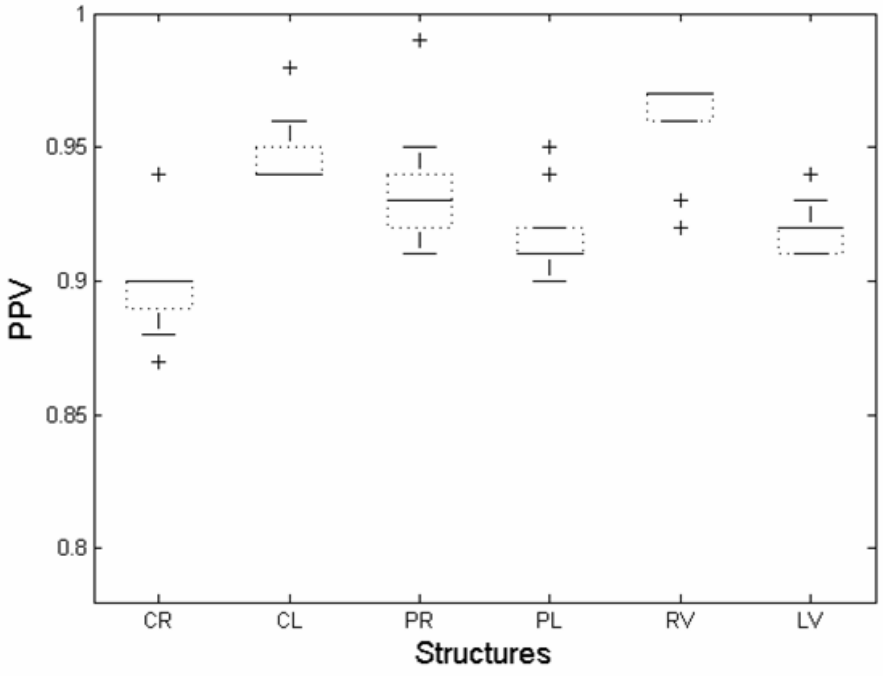

Figure 38. The box plot of the PPV of the six structures (CR, CL, PR, PL, RV and LV).

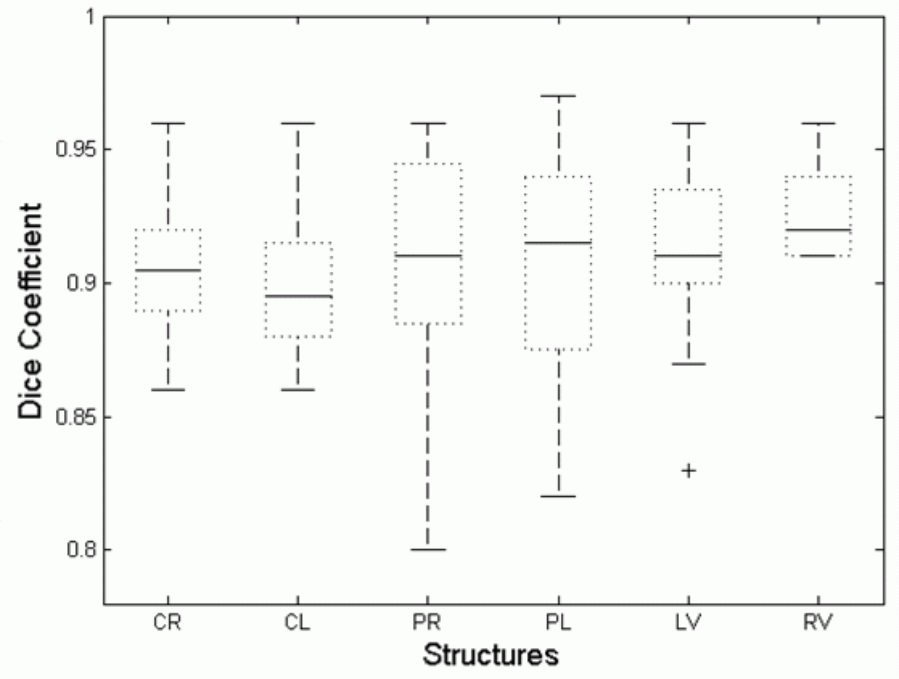

Figure 39. The box plot of the Dice coefficient of the six structures (CR, CL, PR, PL, RV and LV).

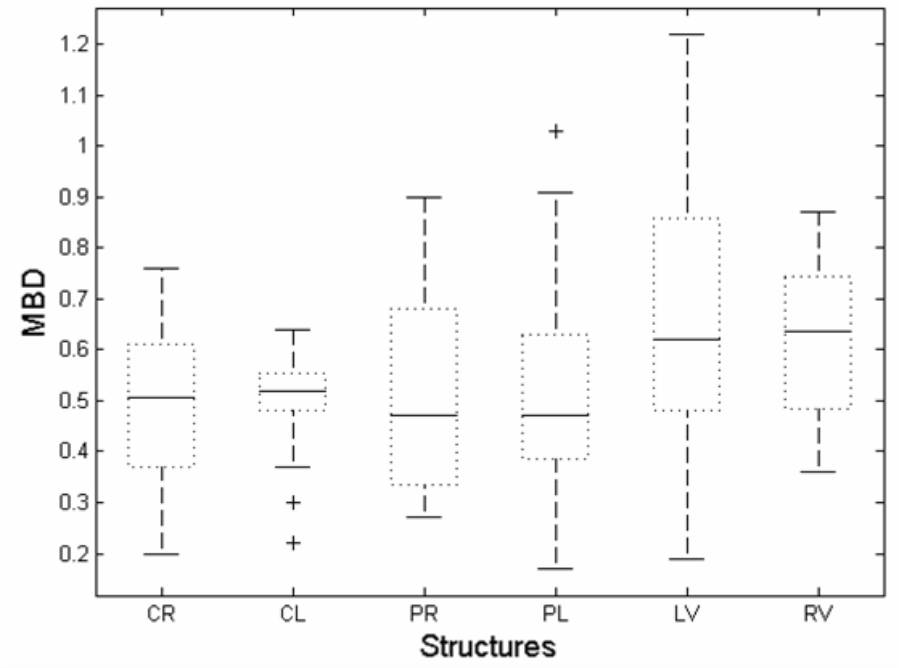

Figure 40. The box plot of the MBD of the six structures (CR, CL, PR, PL, RV and LV).

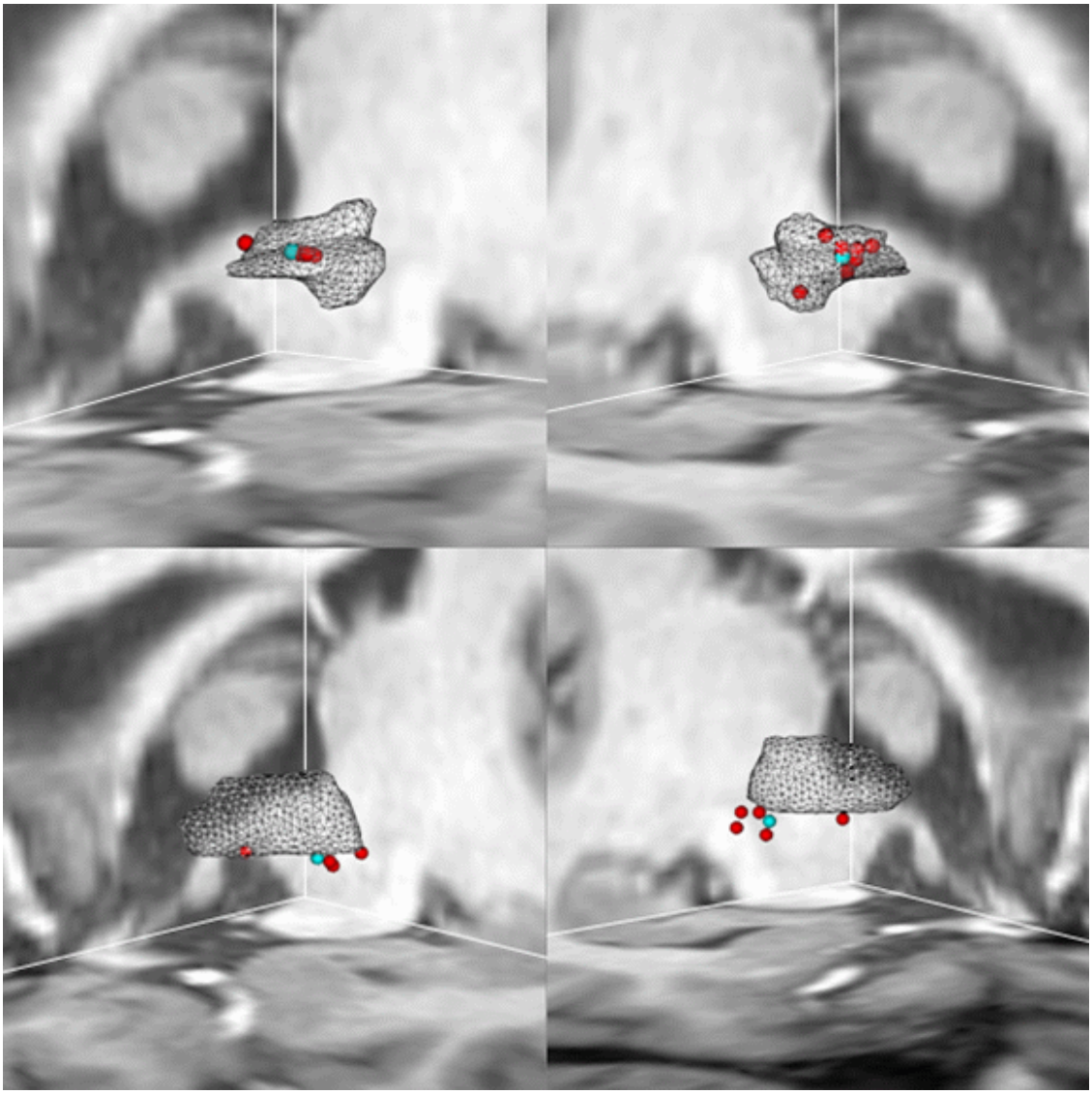

Figure 41. Left STN (top left), right STN (top right), left GPi (bottom left) and right GPi (bottom right) 3D models are shown in zoomed 3D views of the atlas image. The final implant locations transformed from the 20 subjects are shown with red spheres and the centroid of each cluster is shown with blue sphere.

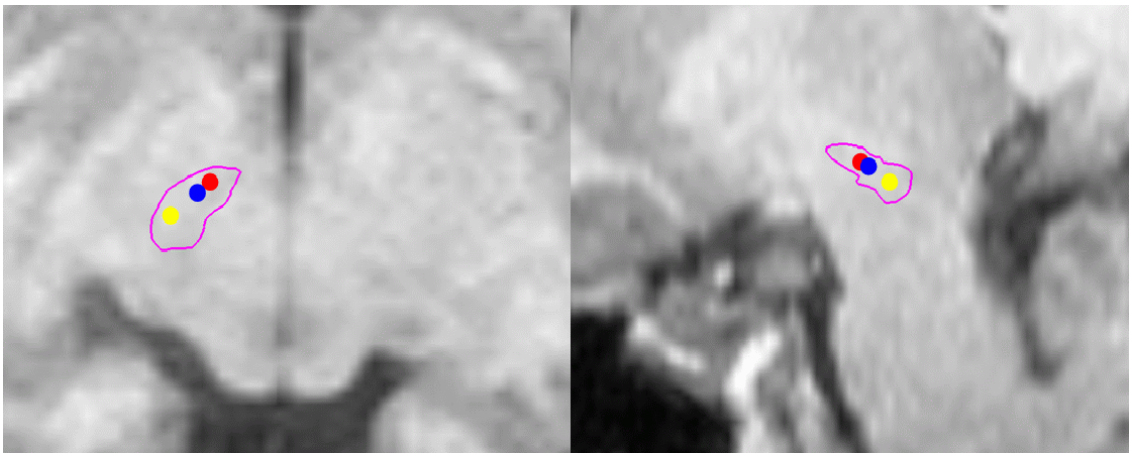

Figure 42. Zoomed axial (left) and sagittal (right) slice of a subject pre-op MR image with the automatically segmented STN contours (in purple). Blue dot shows the actual implant location, red dot shows the automatically predicted implant location by our algorithm and yellow dot shows the manually selected implant location. Note the close proximity of the automatically predicted implant location to the actual implant location.

CHAPTER 5
CONCLUSIONS

This thesis addressed two important problems related to DBS surgery planning and navigation. The first problem was the intraoperative brain shift for which we proposed an accurate method for its analysis and also proposed diploë-based rigid registration. The second problem addressed in this thesis was the automated pre-op localization of the DBS targets for which we proposed an integrated electrophysiological and anatomical 3D MRI atlas, which had eleven deep brain structures segmented in it and electrophysiological data of DBS targets like STN and GPi.

The accuracy of rigid registration of serial MRI head scans can be negatively affected by intensity, topological and geometric image differences if the registration is based on the whole scans. To avoid the influence of image differences on the rigid registration, one can register the scans using the segmented diploë. A study with serial T1 weighted MRI scans of 27 subjects (25 DBS surgery patients, 1 epilepsy surgery patient and 1 tumor removal surgery patient) showed that the diploë-based approach had no measurable registration error and it was consistently more accurate than or equal to the whole-scan approach.

Two detailed studies were conducted for the brain shift analysis during the DBS surgery. The first study showed that, in a group of 25 subjects, the anterior commissure, posterior commissure and both putamina shifted on average 1.8 $\pm$ 0.8 mm and up to 4 mm as a result of deep brain stimulation surgery. On average, the points moved in approximately the direction of gravity with deeper and more central structures experiencing smaller shift than outer structures. The brain shift is non-negligible for implantation of the DBS lead in STN (which is approximately 4 x 6 mm in the axial plane), GPi (which has a maximal radius of approximately 4 mm), or thalamus (which in the Vim/Vop target area measures approximately 2 x 3 x 6 mm), and it therefore should be considered during implantation of DBS electrodes.

The second study of the brain shift analysis performed on eight subjects who underwent DBS surgery recorded shifts of up to 8.3 mm. Larger shifts were related to the presence of pneumocephalus, they were mainly in the gravity direction, and their magnitude dropped

from the anterior region, where the pneumocephalus was located, to the posterior region. Absence of pneumocephalus resulted in smaller shifts. The shift at the implant locations was up to 1.6 mm, which was non-negligible since it was comparable to the size of the target structures. For this reason, brain shift should not be ignored in DBS surgery.

Indirect targeting approaches like atlas based segmentation are used to help infer the DBS target locations like STN, GPi and Vim. An integrated 3D MRI atlas was prepared and proposed for atlas based segmentation, that had eleven deep brain structures manually segmented in it by an expert, and electrophysiological data of four implant locations (left STN, right STN, left GPi and right GPi) using MR images of twenty patients that underwent DBS surgery. This atlas MR image was than non-rigidly registered with the pre-operative subject MR image that gave its initial DBS target location (centroids of STN and GPi clusters) along with the segmented deep brain structures, which were used for guidance during the microelectrode mapping of the stereotactic procedure. The segmentation results were validated for six structures (left and right ventricles, putamena and caudate nuclei) using sensitivity, positive predictive value, Dice coefficient and mean boundary distance. The mean $\pm$ std of the sensitivity was 0.89$\pm$0.013, of PPV was 0.93$\pm$0.013, of Dice coefficient was 0.91 ± 0.03 and of mean boundary distance was 0.55 ± 0.18 mm for twenty subjects over six structures. The electrophysiological atlas data results show that automatic selection of targets using our approach is 85% of the times closer to the final implant location as opposed to the currently used manual selection of target locations. The automatic selection method brings the predicted target point 1 mm on average closer to the actual implant location than the manual target selection. The mean $\pm$ std of the distance form the centroid for STN clusters is 2.1 ± 1.4 mm and GPi clusters is 3.5 ± 2.6 mm that shows the tightness of clusters.

APPENDIX A
DERIVATION OF EQUATION (2.2)

Without loss of generality it is assumed that $x = 0$ is the point between the rigid and nonrigid part of the object shown in Fig. 2. The image before the deformation is

$$I(x) = \begin{cases} 0 & x < -\alpha, \\ 1 + \frac{x}{\alpha} & -\alpha \le x < 0, \\ 1 - \frac{x}{\beta} & 0 \le x < \beta, \\ 0 & x \ge \beta. \end{cases} \tag{A.1}$$

The image after the deformation, $J(x)$, is the same as $I(x)$ except that β is replaced by $\lambda\beta$. The translated $J(x)$ is

$$J(x-t) = \begin{cases} 0 & x < t - \alpha, \\ 1 - \frac{t}{\alpha} + \frac{x}{\alpha} & t - \alpha \le x < t, \\ 1 + \frac{t}{\lambda\beta} - \frac{x}{\lambda\beta} & t \le x < t + \lambda\beta, \\ 0 & x \ge t + \lambda\beta. \end{cases} \tag{A.2}$$

It can be concluded by inspection that when $\lambda < 1$ the minimum of (2.1) is achieved when $0 < t < (1-\lambda)\beta$ and that when $\lambda > 1$ the minimum of (2.1) is achieved when $(1-\lambda)\beta < t < 0$. By combining (A.1), (A.2) and (2.1) one obtains for the two intervals of interest,

$$SSD(t) = \begin{cases} \frac{-(\alpha+\beta)t^3+3\alpha(\alpha+\beta)t^2+3\alpha^2\beta(\lambda-1)t+\alpha^2\beta^2(\lambda-1)^2}{3\alpha^2\beta} & 0 < t < (1-\lambda)\beta, \\ \frac{(\alpha+\lambda\beta)t^3+3\alpha(\alpha+\lambda\beta)t^2+3\alpha^2\beta(\lambda-1)t+\alpha^2\beta^2(\lambda-1)^2}{3\lambda\alpha^2\beta} & (1-\lambda)\beta < t < 0. \end{cases} \tag{A.3}$$

The minimum is obtained from $\frac{d}{dt}SSD = 0$. Since SSD is a (piece-wise) cubic polynomial in t, its derivative is a (piece-wise) quadratic polynomial in t. The quadratic equation has two solutions, one corresponding to a minimum and one to a maximum. It turns out that the minimum is in the respective interval. The translation for which SSD is minimal is given in (2.2).

APPENDIX B
PROOF OF THE THEOREM

Let D_1 denote the rigid region and D_2 denote the deformable region of the object. The image of the object can be written as

$$I(\mathbf{r}) = \begin{cases} R(\mathbf{r}) & \mathbf{r} \in D_1, \\ S(\mathbf{r}) & \mathbf{r} \in D_2, \\ 0 & \mathbf{r} \notin D_1 \cup D_2, \end{cases} \tag{B.1}$$

where $R(\mathbf{r})$ represents the image intensity over the rigid region and $S(\mathbf{r})$ represents the image intensity over the deformable region. We assume that outside the object the image is 0. Without loss of generality one can assume that $R(\mathbf{r}) = 0$ when $\mathbf{r} \notin D_1$ and that $S(\mathbf{r}) = 0$ when $\mathbf{r} \notin D_2$. Then, the image can be written in a more convenient form,

$$I(\mathbf{r}) = R(\mathbf{r}) + S(\mathbf{r}). \tag{B.2}$$

The image of the same object after the deformable part underwent a deformation is

$$J(\mathbf{r}) = R(\mathbf{r}) + S(\mathbf{t}(\mathbf{r})), \tag{B.3}$$

where $\mathbf{t}(\mathbf{r})$ is the inverse of the transformation. Note that this model assumes that the image intensity is identical at corresponding locations in images I and J. A necessary condition for the identity transformation to be a minimizer of (2.4) is

$$\frac{\partial SSD}{\partial \mathbf{b}}\Big|_{\mathbf{A}=\mathbf{I},\mathbf{b}=\mathbf{0}} = \mathbf{0}, \tag{B.4}$$

where $\mathbf{I}$ is an identity matrix. From (2.4), (B.3) and (B.2) it follows that

$$\frac{\partial SSD}{\partial \mathbf{b}}\Big|_{\mathbf{A}=\mathbf{I},\mathbf{b}=\mathbf{0}} = 2\int [S(\mathbf{t}) - S]\left[\frac{\partial R}{\partial \mathbf{r}} + \frac{\partial \mathbf{t}}{\partial \mathbf{r}} \cdot \frac{\partial S}{\partial \mathbf{r}}(\mathbf{t})\right] \tag{B.5}$$

$$= 2\int [S(\mathbf{t}) - S]\frac{\partial R}{\partial \mathbf{r}} + 2\int [S(\mathbf{t}) - S]\frac{\partial \mathbf{t}}{\partial \mathbf{r}} \cdot \frac{\partial S}{\partial \mathbf{r}}(\mathbf{t}). \tag{B.6}$$

The first integral in (B.6) is zero since S and $S(\mathbf{t})$ are zero outside the deformable region and R and consequently $\frac{\partial R}{\partial \mathbf{r}}$ are zero outside the rigid region and therefore the product $[S(\mathbf{t}) - S]\frac{\partial R}{\partial \mathbf{r}}$ is zero everywhere. Thus,

$$\frac{\partial SSD}{\partial \mathbf{b}}\Big|_{\mathbf{A}=\mathbf{I},\mathbf{b}=\mathbf{0}} = 2\int [S(\mathbf{t}) - S]\frac{\partial \mathbf{t}}{\partial \mathbf{r}} \cdot \frac{\partial S}{\partial \mathbf{r}}(\mathbf{t}). \tag{B.7}$$

In the general case (B.7) is not equal to zero, which means that the necessary condition (B.4) is not satisfied, i.e. the identity transformation is not a minimizer of (2.4). □

APPENDIX C

TABLES

Table 8. The values of true positive (TP), false positive (FP), false negative(FN), sensitivity(S), positive value prediction (PVP) and dice coefficient for right caudate nucleus (CR) and left caudate nucleus (CL) of 20 DBS subjects after registration with the atlas image.

Subject No	CR						CL					
	TP	FP	FN	S	PVP	D	TP	FP	FN	S	PVP	D
1	135	9	15	0.90	0.94	0.92	126	3	23	0.85	0.98	0.91
2	100	27	6	0.91	0.87	0.86	101	2	17	0.85	0.98	0.91
3	108	19	6	0.92	0.87	0.90	107	3	13	0.86	0.98	0.93
4	101	4	10	0.92	0.88	0.94	109	8	20	0.86	0.96	0.89
5	122	21	10	0.92	0.87	0.89	115	10	8	0.87	0.95	0.93
6	118	3	7	0.93	0.89	0.96	106	6	15	0.87	0.95	0.91
7	101	5	6	0.93	0.90	0.95	113	9	20	0.87	0.95	0.89
8	114	21	12	0.92	0.89	0.87	100	7	22	0.86	0.95	0.87
9	122	7	19	0.92	0.90	0.90	121	14	20	0.86	0.94	0.88
10	131	18	6	0.92	0.89	0.92	121	4	19	0.86	0.94	0.91
11	95	14	9	0.92	0.89	0.89	87	9	13	0.86	0.94	0.89
12	107	6	10	0.92	0.90	0.93	107	10	17	0.86	0.94	0.89
13	99	4	15	0.92	0.90	0.91	88	9	11	0.86	0.94	0.90
14	111	8	12	0.92	0.90	0.92	116	6	8	0.87	0.94	0.94
15	92	22	9	0.92	0.90	0.86	96	5	21	0.87	0.94	0.88
16	117	11	15	0.91	0.90	0.90	124	7	14	0.87	0.94	0.92
17	114	6	17	0.91	0.90	0.91	107	8	20	0.87	0.94	0.88
18	135	14	17	0.91	0.90	0.90	92	5	26	0.86	0.94	0.86
19	121	14	10	0.91	0.90	0.91	136	2	10	0.87	0.94	0.96
20	104	17	14	0.91	0.90	0.87	102	9	21	0.87	0.94	0.87
Mean	112	13	11	0.92	0.89	0.90	109	7	17	0.86	0.95	0.90
±Std	13	7	4	0.01	0.01	0.03	13	3	5	0.01	0.01	0.03

Table 9. The values of true positive (TP), false positive (FP), false negative(FN), sensitivity(S), positive value prediction (PVP) and dice coefficient for right putamen (PR) and left putamen (PL) of 20 DBS subjects after registration with the atlas image.

Subject No	PR						PL					
	TP	FP	FN	S	PVP	D	TP	FP	FN	S	PVP	D
1	238	2	30	0.89	0.99	0.94	205	12	29	0.88	0.94	0.91
2	212	42	29	0.88	0.91	0.86	239	10	39	0.87	0.95	0.91
3	283	11	15	0.91	0.93	0.96	229	17	58	0.84	0.95	0.86
4	273	10	15	0.92	0.94	0.96	274	12	25	0.86	0.95	0.94
5	223	7	11	0.93	0.94	0.96	258	52	7	0.88	0.92	0.90
6	281	14	14	0.93	0.95	0.95	220	35	24	0.89	0.91	0.88
7	240	26	12	0.93	0.94	0.93	233	26	14	0.89	0.91	0.92
8	243	21	12	0.94	0.94	0.94	239	29	42	0.89	0.91	0.87
9	215	27	32	0.93	0.93	0.88	267	17	20	0.89	0.91	0.94
10	264	22	30	0.93	0.93	0.91	273	10	26	0.90	0.92	0.94
11	189	13	24	0.92	0.93	0.91	206	7	30	0.89	0.92	0.92
12	261	20	32	0.92	0.93	0.91	235	29	31	0.89	0.92	0.89
13	172	14	25	0.92	0.93	0.90	208	52	38	0.89	0.91	0.82
14	246	14	14	0.92	0.93	0.95	214	52	25	0.89	0.90	0.85
15	147	45	27	0.92	0.93	0.80	198	8	53	0.88	0.90	0.87
16	204	44	42	0.91	0.92	0.83	209	7	12	0.89	0.91	0.96
17	210	12	33	0.91	0.92	0.90	177	7	16	0.89	0.91	0.94
18	237	15	25	0.91	0.92	0.92	196	20	6	0.89	0.91	0.94
19	188	24	24	0.91	0.92	0.89	228	4	10	0.89	0.91	0.97
20	218	51	25	0.91	0.91	0.85	213	11	20	0.89	0.91	0.93
Mean	227	22	24	0.92	0.93	0.91	226	21	26	0.88	0.92	0.91
±Std	37	14	9	0.01	0.02	0.04	27	16	14	0.01	0.02	0.04

Table 10. The values of true positive (TP), false positive (FP), false negative(FN), sensitivity(S), positive value prediction (PVP) and dice coefficient for right lateral ventricle (RV) and left lateral ventricle (LV) of 20 DBS subjects after registration with the atlas image.

Subject No	RV						LV					
	TP	FP	FN	S	PVP	D	TP	FP	FN	S	PVP	D
1	400	29	49	0.89	0.93	0.91	407	25	57	0.88	0.94	0.91
2	243	27	14	0.90	0.92	0.92	184	28	10	0.89	0.93	0.91
3	733	10	178	0.83	0.97	0.89	754	56	80	0.90	0.93	0.92
4	487	18	84	0.83	0.97	0.91	760	59	93	0.90	0.93	0.91
5	685	5	145	0.83	0.97	0.90	768	108	38	0.91	0.91	0.91
6	490	38	69	0.84	0.97	0.90	647	74	39	0.92	0.91	0.92
7	392	20	65	0.84	0.97	0.90	611	55	58	0.92	0.91	0.92
8	556	21	52	0.85	0.97	0.94	480	42	42	0.92	0.91	0.92
9	367	10	52	0.85	0.97	0.92	352	44	26	0.92	0.91	0.91
10	280	11	37	0.85	0.97	0.92	444	29	21	0.92	0.91	0.95
11	304	22	20	0.85	0.96	0.94	468	31	10	0.92	0.91	0.96
12	484	48	59	0.86	0.96	0.90	841	81	34	0.93	0.91	0.94
13	637	16	78	0.86	0.96	0.93	866	43	73	0.93	0.92	0.94
14	459	12	175	0.85	0.96	0.83	581	45	69	0.93	0.92	0.91
15	692	11	191	0.84	0.96	0.87	731	78	37	0.93	0.92	0.93
16	622	3	132	0.84	0.97	0.90	689	40	35	0.93	0.92	0.95
17	290	7	17	0.84	0.97	0.96	310	27	13	0.93	0.92	0.94
18	382	16	36	0.84	0.97	0.94	308	15	49	0.93	0.92	0.91
19	420	6	36	0.84	0.97	0.95	469	40	33	0.93	0.92	0.93
20	465	10	84	0.84	0.97	0.91	467	51	32	0.93	0.92	0.92
Mean	469	17	79	0.85	0.96	0.91	557	49	42	0.92	0.92	0.92
±Std	146	11	56	0.02	0.01	0.03	196	23	23	0.02	0.01	0.02

Table 11. The min, max, mean and Std of the mean boundary distance (MBD) for right caudate nucleus (CR) and left caudate nucleus (CL) of 20 DBS subjects.

Subject	**C**R				**C**L			
No	**M**in	**M**ax	**M**ean	**S**td	**M**in	**M**ax	**M**ean	**S**td
1	0.00	2.00	0.42	0.55	0.00	2.83	0.51	0.71
2	0.00	3.00	0.76	0.84	0.00	2.00	0.37	0.53
3	0.00	2.24	0.50	0.69	0.00	1.00	0.38	0.49
4	0.00	1.00	0.24	0.43	0.00	1.41	0.56	0.54
5	0.00	2.00	0.65	0.68	0.00	2.00	0.48	0.59
6	0.00	1.41	0.20	0.42	0.00	1.41	0.48	0.54
7	0.00	1.41	0.24	0.46	0.00	2.00	0.60	0.61
8	0.00	2.24	0.59	0.62	0.00	2.00	0.55	0.57
9	0.00	1.41	0.58	0.54	0.00	1.41	0.52	0.55
10	0.00	1.41	0.40	0.50	0.00	1.00	0.48	0.51
11	0.00	2.00	0.52	0.59	0.00	2.00	0.54	0.59
12	0.00	1.41	0.30	0.47	0.00	2.00	0.57	0.59
13	0.00	1.00	0.34	0.48	0.00	2.24	0.53	0.73
14	0.00	1.41	0.41	0.53	0.00	1.00	0.30	0.46
15	0.00	2.00	0.69	0.62	0.00	2.24	0.55	0.64
16	0.00	1.41	0.54	0.53	0.00	3.16	0.52	0.83
17	0.00	1.41	0.50	0.53	0.00	2.24	0.49	0.62
18	0.00	1.41	0.63	0.56	0.00	3.00	0.59	0.75
19	0.00	1.41	0.51	0.52	0.00	1.41	0.22	0.43
20	0.00	2.00	0.70	0.64	0.00	2.00	0.64	0.72
Mean	**0**.00	**1**.68	**0**.49	**0**.56	**0**.00	**1**.92	**0**.49	**0**.60
±Std	**0**.00	**0**.49	**0**.16	**0**.10	**0**.00	**0**.63	**0**.10	**0**.10

Table 12. The min, max, mean and Std of the mean boundary distance (MBD) for right putamen (PR) and left putamen (PL) of 20 DBS subjects.

Subject	**P**R				**P**L			
No	**M**in	**M**ax	**M**ean	**S**td	**M**in	**M**ax	**M**ean	**S**td
1	0.00	2.83	0.33	0.63	0.00	2.24	0.47	0.66
2	0.00	2.00	0.81	0.61	0.00	2.00	0.59	0.55
3	0.00	2.24	0.34	0.56	0.00	2.00	0.64	0.69
4	0.00	1.00	0.27	0.45	0.00	2.00	0.38	0.56
5	0.00	2.00	0.27	0.50	0.00	3.61	0.63	0.83
6	0.00	2.00	0.31	0.52	0.00	2.00	0.60	0.70
7	0.00	1.00	0.43	0.50	0.00	2.24	0.39	0.59
8	0.00	2.00	0.44	0.60	0.00	2.83	0.62	0.66
9	0.00	2.83	0.70	0.73	0.00	1.41	0.40	0.50
10	0.00	3.61	0.66	0.79	0.00	2.00	0.34	0.51
11	0.00	2.24	0.51	0.58	0.00	2.24	0.47	0.63
12	0.00	2.00	0.61	0.63	0.00	2.00	0.67	0.61
13	0.00	2.24	0.44	0.61	0.00	2.83	0.91	0.81
14	0.00	1.00	0.33	0.47	0.00	5.00	1.03	1.37
15	0.00	3.16	0.90	0.82	0.00	3.16	0.63	0.81
16	0.00	2.83	0.89	0.92	0.00	1.00	0.22	0.42
17	0.00	2.00	0.50	0.56	0.00	1.00	0.30	0.46
18	0.00	2.00	0.44	0.54	0.00	2.24	0.44	0.55
19	0.00	1.41	0.63	0.53	0.00	1.00	0.17	0.38
20	0.00	3.61	0.86	0.95	0.00	1.41	0.42	0.52
Mean	**0**.00	**2**.20	**0**.53	**0**.62	**0**.00	**2**.21	**0**.52	**0**.64
±Std	**0**.00	**0**.77	**0**.21	**0**.14	**0**.00	**0**.96	**0**.21	**0**.21

Table 13. The min, max, mean and Std of the mean boundary distance (MBD) for right lateral ventricle (RV) and left lateral ventricle (LV) of 20 DBS subjects.

Subject	**R**V				**L**V			
No	**M**in	**M**ax	**M**ean	**S**td	**M**in	**M**ax	**M**ean	**S**td
1	0.00	3.00	0.56	0.65	0.00	2.00	0.48	0.54
2	0.00	2.24	0.38	0.58	0.00	3.00	0.40	0.60
3	0.00	7.21	0.98	1.64	0.00	4.00	0.81	0.86
4	0.00	4.00	0.70	0.85	0.00	5.00	0.87	0.98
5	0.00	7.00	1.19	1.52	0.00	2.24	0.78	0.65
6	0.00	3.00	0.65	0.65	0.00	2.00	0.68	0.59
7	0.00	4.00	0.59	0.80	0.00	4.00	0.72	0.79
8	0.00	2.24	0.54	0.61	0.00	2.83	0.65	0.68
9	0.00	2.00	0.48	0.61	0.00	3.61	0.74	0.88
10	0.00	2.24	0.40	0.55	0.00	1.41	0.36	0.49
11	0.00	3.16	0.48	0.72	0.00	3.00	0.36	0.61
12	0.00	3.16	0.83	0.83	0.00	3.00	0.71	0.65
13	0.00	5.00	0.77	1.06	0.00	4.00	0.75	0.82
14	0.00	5.00	0.89	1.09	0.00	2.83	0.56	0.63
15	0.00	6.00	1.22	1.38	0.00	3.00	0.75	0.69
16	0.00	5.00	0.93	1.26	0.00	2.00	0.45	0.57
17	0.00	1.41	0.19	0.41	0.00	4.00	0.49	0.72
18	0.00	2.00	0.39	0.57	0.00	5.00	0.59	0.82
19	0.00	4.47	0.53	0.86	0.00	2.83	0.57	0.66
20	0.00	3.00	0.77	0.76	0.00	2.24	0.62	0.65
Mean	**0**.00	**3**.76	**0**.67	**0**.87	**0**.00	**3**.10	**0**.62	**0**.69
±Std	**0**.00	**1**.68	**0**.27	**0**.35	**0**.00	**1**.00	**0**.15	**0**.13

REFERENCES

[1] D. L. Byrd, W. J. J. Marks, and P. A. Starr, "Deep brain stimulation for advanced parkinson's disease," *AORN Journal*, vol. 72(3), pp. 387–390, Sept. 2000.

[2] C. Honey, R. E. Gross, and A. M. Lozano, "New developments in the surgery for parkinson's disease," *The Canadian Journal of Neurological Sciences*, vol. 26(2), pp. 45–52, Aug. 1999.

[3] P. A. Starr, J. L. Vitek, and R. A. Bakay, "Ablative surgery and deep brain stimulation for parkinson's disease," *Neurosurgery*, vol. 43(5), pp. 989–1013, Nov. 1998.

[4] R. E. Gross and A. M. Lozano, "Advances in neurostimulation for movement disorders," *Neurological Research*, vol. 22(3), pp. 247–258, 2000.

[5] P. Limousin, P. Krack, P. Pollak, A. Benazzouz, C. Ardouin, D. Hoffmann, and A.-L. Benabid, "Electrical stimulation of the subthalamic nucleus in advanced parkinson's disease," *New England Journal of Medicine*, vol. 339(16), pp. 1105–1111, Oct. 1998.

[6] *Atlas of Pathophysiology.* Springhouse, PA, USA: Anatomical Chart Company, 2002.

[7] "Movement disorders fact sheet," *Medtronic.* http://www.medtronic.com, (Last accessed October 2008).

[8] "General facts on parkinson's disease," *Parkinsons Disease Foundation.* http://www.pdf.org, (Last accessed October 2008).

[9] A. Hristova, K. Lyons, A. I. Trster, R. Pahwa, S. B. Wilkinson, and W. C. Koller, "Effect and time course of deep brain stimulation of the globus pallidus and subthalamus on motor features of parkinson's disease," *Clinical Neuropharmacology*, vol. 23(4), pp. 208–211, July 2000.

[10] M. C. Rodriguez-Oroz, M. Rodriguez, J. Guridi, K. Mewes, V. Chockkman, J. Vitek, M. R. DeLong, and J. A. Obeso, "The subthalamic nucleus in parkinson's disease: somatotopic organization and physiological characteristics," *Brain*, vol. 124(9), pp. 1777–1790, Sept. 2001.

[11] A. Machado, A. R. Rezai, B. H. Koppel, R. E. Gross, A. D. Sharan, and A. Behabid, "Deep brain stimulation for parkinson's disease: Surgical technique and perioperative management," *Movement Disorders*, vol. 21(14).

[12] C. Yu, M. L. J. Apuzzo, C. Zee, and Z. Petrovich, "A phantom study of the geometric accuracy of computed tomography and magnetic resonance imaging stereotactic localization with the leksell stereotactic system," *Neurosurgery Online*, vol. 48(5).

[13] J. Fitzpatrick and J. B. West, "The distribution of target registration error in rigid-body point-based registration," *IEEE Transactions on Medical Imaging*, vol. 20(9).

[14] R. J. Maciunas, R. L. Galloway, and J. W. Latimer, "The application accuracy of stereotactic frames," *Neurosurgery Online*, vol. 35(4).

[15] C. Pollo, R. Meuli, P. Maeder, F. Vingerhoets, J. Ghika, and J.-G. Villemure, "Subthalamic nucleus deep brain stimulation for parkinsons disease: Magnetic resonance imaging targeting using visible anatomical landmarks," in *Proceedings of the Meeting of the American Society for Stereotactic and Functional Neurosurgery*, (New York, USA), pp. 76–81, May 2003.

[16] T. Aziz, D. Nandi, S. Parkin, X. Liu, N. Giladi, P. Bain, R. Gregory, C. Joint, R. Scott, and J. Stein, "Targeting the subthalamic nucleus," *Stereotactic and Functional Neurosurgery*, vol. 77(1-4), pp. 87–90, Sept. 2001.

[17] B. H. Kopell, A. R. Rezai, J. W. Chang, and J. L. Vitek, "Anatomy and physiology of the basal ganglia: Implications for deep brain stimulation for parkinson's disease," *Movement Disorders*, vol. 21(14), pp. 238–246, June 2006.

[18] D. Winkler, M. Tittgemeyer, J. Schwarz, C. Preul, K. Strecker, and J. Meixensberger, "The first evaluation of brain shift during functional neurosurgery by deformation field analysis," *Journal of Neurology, Neurosurgery and Psychiatry*, vol. 76, pp. 1161–1163, 2005.

[19] M. F. Khan, K. Mewes, R. E. Gross, and O. Skrinjar, "Assessment of brain shift related to deep brain stimulation surgery," *Stereotactic and Functional Neurosurgery*, vol. 86, pp. 44–53, 2008.

[20] C. H. Halpern, S. F. Danish, G. H. Baltuch, and J. L. Jaggi, "Brain shift during deep brain stimulation surgery for parkinson's disease," *Stereotactic and Functional Neurosurgery*, vol. 86, pp. 37–43, 2008.

[21] O. Škrinjar, A. Nabavib, and J. Duncan, "Model-driven brain shift compensation," *Medical Image Analysis*, vol. 6(4), pp. 361–373, Dec 2002.

[22] K. Wester and J. Kråkenes, "Vertical displacement of the brain and the target area during open stereotaxic neurosurgery," *Acta Neurochirurgica*, vol. 143, pp. 603–606, 2001.

[23] D. L. G. Hill, C. R. Maurer, M. Y. Wang, R. J. Maciunas, J. A. Barwise, and J. M. Fitzpatrick, "Estimation of intraoperative brain surface movement," in *First Joint Conference, Computer Vision, Virtual Reality and Robotics in Medicine and Medical Robotics and Computed-Assisted Surgery (CVRMed-MRCAS)*, (Grenoble, France), pp. 449–458, 1997.

[24] R. Bucholz, D. Yeh, J. Trobaugh, L. McDurmont, C. Sturm, C. Baumann, and M. Jaimie, "The correction of stereotactic inaccuracy caused by brain shift using an intraoperative ultrasound device," in *First Joint Conference, Computer Vision, Virtual Reality and Robotics in Medicine and Medical Robotics and Computed-Assisted Surgery (CVRMed-MRCAS)*, (Grenoble, France), pp. 459–466, 1997.

[25] C. R. Maurer, D. L. Hill, A. J. Martin, H. Liu, M. McCue, D. Rueckert, D. Lloret, W. A. Hall, R. E. Maxwell, D. J. Hawkes, and C. L. Truwit, "Investigation of intraoperative brain deformation using a 1.5 tesla interventional mr system: Preliminary results," *IEEE Transactions on Medical Imaging*, vol. 17(5), pp. 817–825, 1998.

[26] A. Nabavi, P. M. Black, D. T. Gering, C. F. Westin, V. Mehta, R. S. Pergolizzi, M. Ferrant, S. K. Warfield, N. Hata, R. B. Schwartz, W. M. W. III, R. Kikinis, and F. A. Jolesz, "Serial intraoperative mr imaging of brain shift," *Neurosurgery*, vol. 48(4), pp. 787–798, Apr 2001.

[27] C. Nimsky, O. Ganslandt, S. Cerny, P. Hastreiter, G. Greiner, and R. Fahlbusch, "Quantification of, visualization of, and compensation for brain shift using intraoperative magnetic resonance imaging," *Neurosurgery*, vol. 47(5), pp. 1070–1080, 2000.

[28] D. W. Roberts, A. H. F. E. Kennedy, M. I. Miga, and K. D. Paulsen, "Intraoperative brain shift and deformation: A quantitative analysis of cortical displacement in 28 cases," *Neurosurgery*, vol. 43(4), pp. 749–760, 1998.

[29] P. J. Edwards, D. L. G. Hill, J. A. Little, and D. J. Hawkes, "A three-component deformation model for image-guided surgery," *Medical Image Analysis*, vol. 2(4), pp. 355–367, Dec 1998.

[30] M. I. Miga, A. Staubert, K. D. Paulsen, F. E. Kennedy, V. M. Tronnier, D. W. Roberts, A. Hartov, L. A. Platenik, and K. E. Lunn, "Model-updated image-guided neurosurgery: Preliminary analysis using intraoperative mr," in *Medical Image Computing and Computer Aided Intervention (MICCAI)*, (Pittsburgh, PA, USA), pp. 115–124, 2000.

[31] D. L. G. Hill, C. R. M. Jr., A. J. Martin, S. Sabanathan, W. A. Hall, D. J. Hawkes, D. Rueckert, and C. L. Truwit, "Assessment of intraoperative brain deformation using interventional mr imaging," in *Medical Image Computing and Computer Aided Intervention (MICCAI)*, (Cambridge, UK), pp. 910–919, 1999.

[32] R. M. Comeau, A. Fenster, and T. M. Peters, "Intraoperative ultrasound for guidance and tissue shift correction in image-guided neurosurgery," *Medical Physics*, vol. 27(4), pp. 787–800, 2000.

[33] M. F. Khan, K. Mewes, R. E. Gross, and O. Skrinjar, "Analysis of brain shift related to deep brain stimulation surgery using non-rigid registration," *IEEE Transactions on Biomedical Engineering*, Under Revision.

[34] S. Lucerna, F. M. Salpietro, C. Alafaci, and F. Tomasello, *In Vivo Atlas of Deep Brain Structures with 3D Reconstructions*. Germany: Springer, 2002.

[35] P. D'Haese, E. Cetinkaya, P. Konrad, C. Kao, and B. Dawant, "Computer-aided placement of deep brain stimulators: from planning to intraoperative guidance," *IEEE Transactions on Medical Imaging*, vol. 24(11), pp. 1469–1478, Nov. 2005.

[36] K. Finnis, Y. Starreveld, A. Parrent, A. Sadikot, and T. Peters, "Three-dimensional database of subcortical electrophysiology for image-guided stereotactic functional neurosurgery," *IEEE Transactions on Medical Imaging*, vol. 22(1), pp. 93 – 104, Jan. 2003.

[37] T. Talairach and P. Tournoux, *Co-Planar Steretaxic Atlas of the Human brain*. New York, USA: Thieme, 1988.

[38] G. Schaltenbrand and W. Wahren, *Atlas for Stereotaxy of the Human Brain*. New York, USA: Thieme, 1977.

[39] M. F. Khan, K. Mewes, R. E. Gross, and O. Skrinjar, "An integrated electrophysiological and anatomical mri atlas for image guided deep brain stimulation surgery," *Medical Image Analysis*, Under Submission.

[40] K. A. Ganser, H. Dickhaus, R. Metzner, and C. R. Wirtz, "A deformable digital brain atlas system according to talairach and tournoux," *Medical Image Analysis*, vol. 8(1), pp. 3–22, Mar. 2004.

[41] M. Ortega, M. C. Juan, M. Alcaiz, J. A. Gil, and C. Monserrat, "Deformable brain atlas validation of the location of subthalamic nucleus using t1-weighted mr images of patients operated on for parkinsons," *Computerized Medical Imaging and Graphics*, vol. 32(5), pp. 367–378, July 2008.

[42] M. Chen, T. Kanade, D. Pomerleau, and H. Rowley, "Anomaly detection through registration," *Pattern Recognition*, vol. 32(1), pp. 113–128, Jan. 1999.

[43] B. M. Dawant, S. L. Hartmann, J.-P. Thirion, F. Maes, D. Vandermeulen, and P. Demaerel, "Automatic 3-d segmentation of internal structures of the head in mr images using a combination of similarity and free-form transformations: Part i, methodology and validation on normal subjects," *IEEE Transactions on Medical Imaging*, vol. 18(10), pp. 909–916, Oct. 1999.

[44] S. L. Hartmann, M. H. Parks, P. R. Martin, and B. M. Dawant, "Automatic 3-d segmentation of internal structures of the head in mr images using a combination of similarity and free-form transformations: Part ii, validation on severely atrophied brains," *IEEE Transactions on Medical Imaging*, vol. 18(10), pp. 917–926, Oct. 1999.

[45] K. M. Pohla, J. Fisher, W. E. L. Grimson, R. Kikinis, and W. M. Wells, "A bayesian model for joint segmentation and registration," *NeuroImage*, vol. 31(1), pp. 228–239, May 2006.

[46] D. L. Collins, A. P. Zijdenbos, W. F. C. Baare, and A. C. Evans, "Animal+insect: Improved cortical structure segmentation," in *Proceedings of the 16th International Conference on Information Processing in Medical Imaging*, pp. 210–223, Springer-Verlag London, UK, May 1999.

[47] P. St-Jean, A. F. Sadikot, L. Collins, D. Clonda, R. Kasrai, A. C. Evans, and T. M. Peters, "Automated atlas integration and interactive three-dimensional visualization tools for planning and guidance in functional neurosurgery," *IEEE Transactions on Medical Imaging*, vol. 17(5), pp. 672–680, Oct. 1998.

[48] P. F. D'Haese, S. Pallavaram, K. Niermann, J. Spooner, C. Kao, P. E. Konrad, and B. M. Dawant, "Automatic selection of dbs target points using multiple electrophysiological atlases," in *Proceedings of the Medical Image Computing and Computer Assisted Intervention (MICCAI)*, pp. 427–434, Springer Berlin, Germany, Oct. 2005.

[49] F. J. Castro, C. Pollo, R. Meuli, P. Maeder, O. Cuisenaire, M. B. Cuadra, J. G. Villemure, and J. P. Thiran, "A cross validation study of deep brain stimulation targeting: From experts to atlas-based, segmentation-based and automatic registration algorithms," *IEEE Transactions on Medical Imaging*, vol. 25(11), pp. 1440–1450, Nov. 2006.

[50] Y. Xia, K. Bettinger, L. Shen, and A. L. Reiss, "Automatic segmentation of the caudate nucleus from human brain mr images," *IEEE Transactions on Medical Imaging*, vol. 26(4), pp. 509–517, Apr. 2007.

[51] D. Shen, E. H. Herskovits, and C. Davatzikos, "An adaptive-focus statistical shape model for segmentation and shape modeling of 3-d brain structures," *IEEE Transactions on Medical Imaging*, vol. 20(4), pp. 257–270, Apr. 2001.

[52] V. Barra and J.-Y. J.Y Boire, "Automatic segmentation of subcortical brain structures in mr images using information fusion," *IEEE Transactions on Medical Imaging*, vol. 20(7), pp. 549–558, July 2001.

[53] L. Amini, H. Soltanian-Zadeh, C. Lucas, and M. Gity, "Automatic segmentation of thalamus from brain mri integrating fuzzy clustering and dynamic contours," *IEEE Transactions on Biomedial Engineering*, vol. 51(5), pp. 800–811, May 2004.

[54] N. Duta and M. Sonka, "Segmentation and interpretation of mr brain images: An improved active shape model," *IEEE Transactions on Medical Imaging*, vol. 17(6), pp. 1049–1062, Dec. 1998.

[55] J. Yang, L. H. Staib, and J. S. Duncan, "Neighbor-constrained segmentation with level set based 3-d deformable models," *IEEE Transactions on Medical Imaging*, vol. 23(8), pp. 940–948, Aug. 2004.

[56] A. Kelemen, G. Szekely, and G. Gerig, "Elastic model-based segmentation of 3-d neuroradiological data sets," *IEEE Transactions on Medical Imaging*, vol. 18(10), pp. 828–839, Oct. 1999.

[57] O. Colliot, O. Camara, and I. Bloch, "Integration of fuzzy spatial relations in deformable modelsapplication to brain mri segmentation," *Pattern Recognition*, vol. 39(8), pp. 1401–1414, 2006.

[58] A. J. Worth, N. Makris, M. R. Patti, J. M. Goodman, E. A. Hoge, J. Verne S. Caviness, and D. N. Kennedy, "Precise segmentation of the lateral ventricles and caudate nucleus in mr brain images using anatomically driven histograms," *IEEE Transactions on Medical Imaging*, vol. 17(2), pp. 303–310, Apr. 1998.

[59] H. R. Jäger, E. J. Williams, D. G. Savage, S. A. J. Rule, J. V. Hajnal, K. Sikora, J. M. Goldman, and G. M. Bydder, "Assessment of brain changes with registered mr before and after bone marrow transplantation for chronic myeloid leukemia," *American Journal of Neuroradiology*, vol. 17, pp. 1275–1282, August 1996.

[60] D. T. Gering, A. Nabavi, R. Kikinis, N. Hata, L. J. O'Donnell, E. E. L. Grimson, F. A. Jolesz, P. M. Black, and W. M. Wells, III, "An integrated visualization system for surgical planning and guidance using image fusion and an open mr," *Journal of Magnetic Resonance Imaging*, vol. 13, pp. 967–975, June 2001.

[61] A. Nabavi, P. Black, D. T. Gering, C. Westin, V. Mehta, R. S. Pergolizzi, Jr., M. Ferrant, S. K. Warfield, N. Hata, R. B. Schwartz, W. M. Wells, III, R. Kikinis, and F. A. Jolesz, "Serial intraoperative magnetic resonance imaging of brain shift," *Neurosurgery*, vol. 48, pp. 787–798, April 2001.

[62] T. Hartkens, D. L. G. Hill, A. D. Castellano-Smith, D. J. Hawkes, C. R. Maurer, Jr., A. J. Martin, W. A. Hall, H. Liu, and C. L. Truwit, "Measurement and analysis of brain deformation during neurosurgery," *IEEE Transactions on Medical Imaging*, vol. 22, pp. 82–92, January 2003.

[63] P. Hastreiter, C. Rezk-Salama, G. Soza, M. Bauer, G. Greiner, R. Fahlbusch, O. Ganslandt, and C. Nimsky, "Strategies for brain shift evaluation," *Medical Image Analysis*, vol. 8, pp. 447–464, December 2004.

[64] O. Clatz, H. Delingette, I. Talos, A. J. Golby, R. Kikinis, F. A. Jolesz, N. Ayache, and S. K. Warfield, "Robust nonrigid registration to capture brain shift from intraoperative mri," *IEEE Transactions on Medical Imaging*, vol. 24, pp. 1417–1427, November 2005.

[65] S. M. Haney, P. M. Thompson, T. F. Cloughesy, J. R. Alger, and A. W. Toga, "Tracking tumor growth rates in patients with malignant gliomas: A test of two algorithms," *American Journal of Neuroradiology*, vol. 22, pp. 73–82, January 2001.

[66] N. C. Fox, R. Jenkins, S. M. Leary, V. L. Stevenson, N. A. Losseff, W. R. Crum, R. J. Harvey, M. N. Rossor, D. H. Miller, and A. J. Thompson, "Progressive cerebral atrophy in ms: A serial study using registered, volumetric mri," *Neurology*, vol. 54, pp. 807–812, February 2000.

[67] N. C. Fox, R. I. Scahill, W. R. Crum, and M. N. Rossor, "Correlation between rates of brain atrophy and cognitive decline in ad," *Neurology*, vol. 52, pp. 1687–1689, May 1999.

[68] B. K. Puri, A. J. Richardson, A. Oatridge, J. V. Hajnal, and N. Saeed, "Cerebral ventricular asymmetry in schizophrenia: A high resolution 3d magnetic resonance imaging study," *International Journal of Psycophysiology*, vol. 34, pp. 207–211, December 1999.

[69] S. Kovačič, J. C. Gee, W. S. L. Ching, M. Reivich, and R. Bajcsy, "Three-dimensional registration of pet and ct images," in *11th Annual International Conference of the IEEE Engineering in Medicine and Biology Society*, pp. 548–549, November 1989.

[70] C. R. Maurer, Jr., J. M. Fitzpatrick, M. Y. Wang, R. L. Galloway, Jr., E. J. Maciunas, and G. S. Allen, "Registration of head volume images using implantable fiducial markers," *IEEE Transactions on Medical Imaging*, vol. 16, pp. 447–462, August 1997.

[71] T. Peters, B. Davey, P. Munger, R. Comeau, A. Evans, and A. Olivier, "Three-dimensional multimodla image-guidance for neurosurgery," *IEEE Transactions on Medical Imaging*, vol. 15, pp. 121–128, April 1996.

[72] N. M. Alpert, J. F. Bradshaw, D. Kennedy, and J. A. Correia, "The principal axes transformation - a method for image registration," *The Journal of Nuclear Medicine*, vol. 31, pp. 1717–1722, October 1990.

[73] D. L. G. Hill, D. J. Hawkes, M. J. Gleeson, T. C. S. Cox, A. J. Strong, W. Wong, C. F. Ruff, N. D. Kitchen, D. G. T. Thomas, A. Sofat, J. E. Crossman, C. Studholme, A. J. Gandhe, S. E. M. Green, and G. P. Robinson, "Accurate frameless registration of mr and ct images of the head: Applications in planning surgery and radiation therapy," *Radiology*, vol. 191, pp. 447–454, May 1994.

[74] J. C. de Munck, F. C. Verster, E. A. Dubois, J. B. A. Habraken, B. Boltjes, J. J. Claus, and M. van Herk, "Registration of mr and spect without using external fiducial markers," *Physics in Medicine and Biology*, vol. 43, pp. 1255–1269, May 1998.

[75] A. Rangarajan, H. Chui, and J. S. Duncan, "Rigid point feature registration using mutual information," *Medical Image Analysis*, vol. 3, pp. 425–440, December 1999.

[76] M. Holden, D. L. G. Hill, E. R. E. Denton, J. M. Jarosz, T. C. S. Cox, T. Rohlfing, J. Goodey, and D. J. Hawkes, "Voxel similarity measures for 3-d serial mr brain image registration," *IEEE Transactions on Medical Imaging*, vol. 19, pp. 94–102, February 2000.

[77] M. F. Khan and O. Skrinjar, "Diploe-based rigid registration of serial mri head scans," *Medical Image Analysis*, Submitted after Revision.

[78] C. Studholme, D. L. G. Hill, and D. J. Hawkes, "An overlap invariant entropy measure of 3d medical image alignment," *Pattern Recognition*, vol. 32, pp. 71–86, January 1999.

[79] G. Wahba, "Spline interpolation and smoothing on the sphere," *SIAM Journal Sci. Stat. Comput.*, vol. 2, pp. 1–15, 1981.

[80] A. Katanforoush and M. Shahshahani, "Distributing points on the sphere, I," *Experimental Mathematics*, vol. 12, no. 2, pp. 199–209, 2003.

[81] K. H. Zou, S. K. Warfield, A. Bharatha, C. M. C. Tempany, M. R. Kaus, S. J. Haker, W. M. Wells, III, F. A. Jolesz, and R. Kikinis, "Statistical validation of image segmentation quality based on a spatial overlap index," *Academic Radiology*, vol. 11, pp. 178–189, February 2004.

[82] D. Rueckert, L. I. Sonda, C. Hayes, D. L. G. Hill, M. O. Leach, and D. J. Hawkes, "Nonrigid registration using free-form deformations: Application to breast mr images," *IEEE Transactions on Medical Imaging*, vol. 18, pp. 712–721, August 1999.

[83] F. Bookstein, "Principal warps: Thin-plate splines and the decomposition of deformations," *IEEE Transactions on Pattern Analysis and Machine Intelligence*, vol. 29, pp. 567–585, June 1989.

[84] W. H. Press, B. P. Flannery, S. A. Teukolsky, and W. T. Vetterling, *Numerical Recipes in C: the art of scientific computing*. New York, NY, USA: Cambrige Univeristy Press, 1992.

[85] R. E. Gross, P. Krack, M. C. Rodriguez-Oroz, A. R. Rezai, and A.-L. Benabid, "Electrophysiological mapping for the implantation of deep brain stimulators for parkinsons disease and tremor," *Movement Disorders*, vol. 21(S14), pp. S259–S283, 2006.

[86] W. E. Lorensen and H. E. Cline, "Marching cubes: A high resolution 3d surface construction algorithm," in *Computer Graphics*, vol. 21(4), July 1987.

[87] G. Taubin, "A signal processing approach to fair surface design," in *SIGGRAPH 95: Proceedings of the 22nd annual conference on Computer graphics and interactive techniques*, pp. 351–358, 1995.